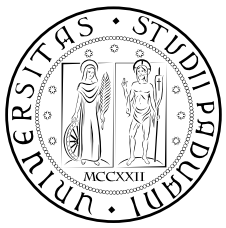

UNIVERSITÀ DEGLI STUDI DI PADOVA

DIPARTIMENTO DI TECNICA E GESTIONE DEI SISTEMI INDUSTRIALI
CORSO DI LAUREA MAGISTRALE IN INGEGNERIA MECCATRONICA

MASTER THESIS

High-Performance Multi-Axis Control with Applications in Compliant Parallel Manipulators

Supervisor: Roberto Oboe

Co-Supervisors: Richard Kavanagh [UCC], Guangbo Hao [UCC]

Author: Elena Petri
1183905-IMC

ACADEMIC YEAR: 2019-20

ucc

Coláiste na hOllscoile Corcaigh, Éire
University College Cork, Ireland

All the activities related to this thesis work were performed in the Mechatronic Laboratory of the Electrical and Electronic Engineering building at the University College Cork (UCC), Ireland, during an Erasmus project.

ABSTRACT

In this thesis, a two-axis high-performance compliant positioning system (whereby movements are performed through the deflection of its flexible components) is analyzed and controlled. A high-performance positioning system is a mechatronic motion system capable of high-quality motion (as for the system described here), in the micrometer or the nanometer ranges. While the mechanical structure was designed to perform movements in the nanometer range, the noise introduced by the available servo amplifiers limits the attainable system performance.

Starting from previous works related to single-axis movements, this thesis focuses on the improvement of the control algorithm performance, implemented in Matlab-Simulink, and on its extension to two-axis movements. Each axis can be accurately modelled using linear equations only within in a small motion range of up to ± 0.2 mm. Beyond this threshold, the axis movement has a significantly non-linear behaviour. To achieve high-performance motion over a wide range of up to ± 1 mm in each axis, a non-linear model has to be used in the control algorithm.

The control algorithm for each axis is based on a PID feedback controller and a force feed-forward controller. In addition, when both axes are to move simultaneously two cross-coupling interactions arise between them. It was found that these effects are quite small, but not negligible. Static compensations for these two undesired phenomena were implemented.

Finally, with the target of repeatedly carrying out some physically useful shapes in the XY-plane, such as circular or square trajectories, periodic reference signals have been used. When these reference signal are used, the system performance improves, especially at the higher frequency movements, using high-performance controllers, such as repetitive control (RPC) or iterative learning control (ILC).

SOMMARIO

In questa tesi vengono presentate le prestazioni ed il sistema di controllo di un sistema di posizionamento biassiale ad elevate prestazioni basato sulla tecnologia compliant, che perciò permette di realizzare il movimento sfruttando la deformazione dei suoi componenti flessibili. Un sistema di posizionamento ad alte prestazioni è un sistema meccatronico che esegue movimenti con un'elevata qualità di funzionamento. Il sistema descritto in questa tesi può operare nel range dei micrometri o dei nanometri. Purtroppo, anche se la struttura meccanica è stata progettata per eseguire movimenti con qualità nanometrica, il rumore introdotto dai servo amplifiers limita le prestazioni del sistema.
Basandosi sulle attività di tesi svolte in precedenza e relative ai movimenti lungo un singolo asse, questo lavoro si focalizza sul miglioramento dell'algoritmo di controllo, implementato in Matlab-Simulink, e sulla sua estensione a movimenti simultanei di due assi complanari. L'uso di un modello lineare permette di descrivere accuratamente il comportamento di un singolo asse solamente nel caso di piccoli movimenti, con un'ampiezza massima dell'escursione fino a ± 0.2 mm. Superato questo limite, l'approssimazione lineare non permette più di ottenere l'accuratezza richiesta. Per garantire elevate prestazioni su un range di movimento più ampio, fino ad ± 1 mm per ciascun asse, nel sistema di controllo è necessario utilizzare le equazioni che descrivono le non linearità del sistema.
L'algoritmo di controllo per un singolo asse è costituito da un PID in retroazione e da un feed-forward di forza. Inoltre, durante il moto simultaneo dei due assi considerati, sono state rilevate ed analizzate due tipi di interazioni di cross-coupling tra di essi. L'effetto di entrambe queste interazioni sulla qualità del movimento è risultato piuttosto ridotto, ma comunque non trascurabile. Conseguentemente, gli effetti statici di questi fenomeni indesiderati sono stati compensati.
Il sistema è stato inoltre alimentato con segnali di riferimento periodici, con l'obiettivo di tracciare ripetutamente forme geometriche significative nel piano XY, come per esempio circonferenze o quadrati. Utilizzando controllori ad alte prestazioni, come il repetitive control (RPC) o l'iterative learning control (ILC) è stato inoltre possibile migliorare drasticamente le prestazioni del sistema specialmente nel caso di movimenti a più elevata frequenza.

ACKNOWLEDGEMENTS

I would like to thank both my supervisors in UCC, Dr. Richard Kavanagh and Dr. Guangbo Hao for the suggestions and support that they provided me for all the activities related to this thesis work. I would like to thanks my italian supervisor Professor Roberto Oboe for his suggestions and advices. Big thanks go to all the technicians and the UCC's staff, in particular to Micheal O'Shea, Tim Power, Hilary Mansfield, James Griffiths and Ralph O'Flaherty. They were always kind and available to solve any technical problem that arose in the system.
I wish to thank my parents and my brother Davide for their support during my studies and for continuously believing in me, in my dedication and in my capabilities.
I would like to thank my Cork's friends. They allowed me to feel at home during my stay in Ireland. I wish to remember also my italian friends. I spent with them a lot of unforgettable moments and they helped me to tackle challenging studies. Finally, I would like to thank Marco for his continuous effective support, especially during the most difficult moments.

CONTENTS

LIST OF FIGURES

LIST OF TABLES

1 INTRODUCTION

1.1 HIGH-PERFORMANCE POSITIONING SYSTEMS

High-performance positioning systems, such as micro-positioning systems and nano-positioning systems, are mechatronic motion systems capable of micrometric or nanometric motion quality. Many applications of micro-technologies or nano-technologies require an extremely high level of movement quality, which is not achievable by humans; thus high-performance positioning mechanisms are required more and more frequently.
High-performance motion quality is determined by three main parameters below. These are easily and clearly defined in terms of measurement, but parameters defined in terms of actuation can also be defined similarly.

- Precision: defined as the "closeness of agreement between indications or measured quantity values obtained by replicate measurements on the same or similar objects under specified conditions" [1].
- Accuracy: defined as the "closeness of agreement between a measured quantity value and a true quantity value of a measurand" [1].
- Resolution: defined as the "smallest change in a quantity being measured that causes a perceptible change in the corresponding indication" [1].

Besides high motion quality, high-performance positioning systems are required to exhibit also a high bandwidth and a large range of motion. To ensure these characteristics both the choice of the components and the manipulator design have to be considered very carefully. Compliant mechanisms are an excellent choice for the mechanical structure of high-performance positioning systems, due to their specific features, as it will be described in the next section. The choice of the actuator is also critical. Usually direct-drive linear electromagnetic actuators, piezo-electric actuators, or inchworm style actuators are adopted [2]. The voice coil actuators, which belong to the category of direct-drive linear electromagnetic actuators, are the best option for large range high-performance positioning systems due to their linear behaviour and because they are frictionless, hysteresis free and cog-free. In addition they allow direct control of actuation force [2]. Moreover, the choice of the sensors is also relevant in a high-performance

positioning system. Linear optical encoders are considered one of the best options [2].
Possible high-performance positioning systems applications are: super-resolution microscopes, spectroscopy, scanning probe microscopes and surface profilometry, optical tweezers and optical traps, medical/health devices, nanofabrication, MEMS and NEMS development, assembly and testing [3], [4], [2], [5].

1.2 COMPLIANT MECHANISMS

A mechanism is a mechanical device used to transfer or transform input force, displacement and energy into output force, displacement and energy. [6], [5].
Traditional rigid-body mechanisms are assemblies of rigid components connected at movable joints, such as sliding joints or rolling joints. The mechanism motion are performed through the operation of the joints [6], [5].
A compliant mechanism, unlike the rigid-body mechanisms, exploits the deflection of its flexible components to perform at least part of its movement [7], [6].
Compliant mechanisms, compared to rigid-body mechanisms, have several advantages. The first one is the reduced number of components, which simplify their manufacturing and assembly, thus saving production time and cost. Moreover, compliant mechanisms have less movable joints or they can be jointless. This characteristic reduces wear and the need of lubrication, and so makes the compliant mechanism more suitable for application in harsh environments, that can affect the joints, or where access is not easy. In addition, mechanism precision is increased as compared to the traditional rigid-body solution because backlash is reduced or eliminated due to the reduced number of joints. Furthermore, compliant mechanisms usually weight less than their rigid-body counterparts. Another advantage is that they are easy to be miniaturized. In addition, compliant mechanism are a good choice for applications requiring clean or sterile environments, as occurs in the medical field or in extreme vacuum environments. Unfortunately, compliant mechanisms have also some drawbacks. Comparing to the traditional rigid-body solution, their design and analysis are more difficult. Indeed, due to the large deflections of their flexible components, the equations that describe a compliant mechanism are usually non-linear. In addition, the motion range of a compliant mechanism can be limited due to physical constraints on the deflection of its components [6], [7], [8].

1.3 THE ANALYZED SYSTEM

The high-performance positioning system analyzed in this thesis work is a two-axis compliant parallel manipulator. It was designed to perform high-quality movement in a large motion range (± 1 mm on both axes). A photo of the system is shown in Figure 1.1 and a detailed description of all its components is reported in Chapter 3.

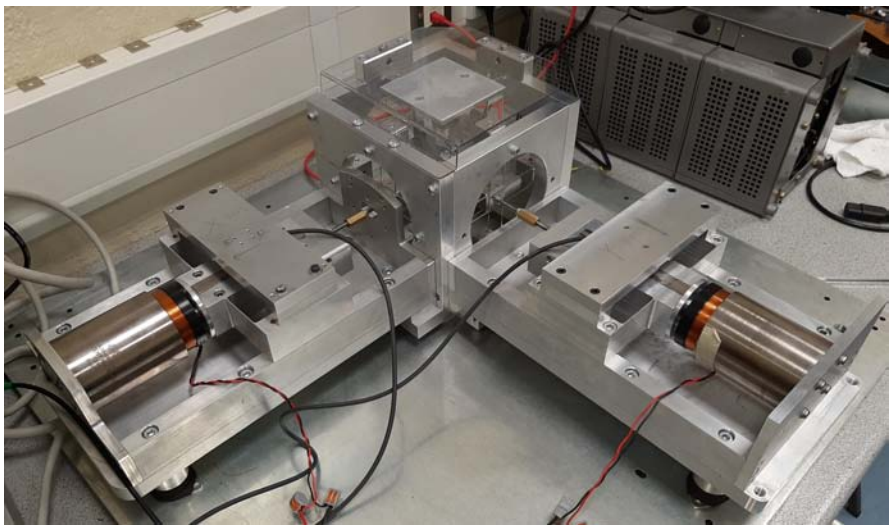

Figure 1.1: Two-axis high-performance positioning system analyzed

The most innovative part of the mechanical system is the XYZ compliant mechanism designed in [5]. It is symmetric and allows motion translation along three orthogonal directions. Moreover, it provides reduced cross-coupling between the axes, minimum lost motion and relatively small parasitic motion. The XYZ compliant mechanism has several possible applications, summarized in Table 1.1 [5].

The project of the high-performance positioning system analyzed in this work has been developed by a number of students:

- Haiyang Li designed the XYZ compliant mechanism.
  PhD thesis [UCC]: "Approaches to the synthesis, modelling and optimisation of spatial translational compliant parallel mechanisms", 2016 [5].

- Fabiana Federica Ferro completed the system setup and implemented the close-loop control algorithm.
  Master thesis [UNIPD]:" Nonlinear Control of a Flexure-Based Single Degree of Freedom Nanopositioning System", 2016 [9]

- Riccardo Sandon completed the control algorithm introducing the force feed-forward assuming that the system is operating in its linear range (up to ± 0.2 mm) and performed a deep analysis of the system performance.

Application field	Application description
Micro assembly	Assembly of micro components
Nano-/micro-positioning	High performance micro-/nano-positioning along X-,Y and Z-axes
Optics	Handling of small components and assemblies
Optical tweezers and optical traps	Manipulating nanometer and micrometer sized electric particles
Optical fibre alignment	Accurate motion and placement of individual fibres for alignment
Metrology	Accurate measurement of motion and placement
AFM (Atomic Force Microscope)	Accurate placement of specimen for examination
Spectroscopy	Measurement of radiation intensity as a function of wavelength
Super resolution microscopy	Accurate placement of specimen for examination
Photovoltaics	Component alignment
MEMS	Accurate handling of nano- and micro-electronic mechanical systems
Nano-fabrication, nano-pattering and nano-machining	Accurate positioning with precision motion is needed to manufacture small, detailed components
Magnetic tweezers, traps and manipulation	Scientific instruments for the manipulation of biomolecules

Table 1.1: Possible applications of the XYZ compliant mechanism [5]

Master thesis [UNIPD]: "Modelling, Control and Performance Evaluation of a Single-Axis Compliant Nano-Positioning System", 2017 [10]

- Aldo Marchi extended the control algorithm to the non-linear range, modifying both the feedback and the feed-forward controllers. The motion range was extended to ± 1 mm.
  Master thesis [UNIPD]: "Wide Range Control and Performance Evaluation of a Single-Axis Compliant Nano-Positioning System", 2019 [8].

All of the theses reported above are related only to the one-axis system (that axis is called X-axis in the following). The system operation capability was then extended to two axes and the main purpose of this project was to extend the control algorithm, implemented in Matlab-Simulink, to both axes of the system in order to allow a controlled movement on a plane surface. For this reason the starting point of this thesis work was the control scheme reported in [8] for the one-axis system operating in the non-linear range. Improving the system performance is also a major objective of the work. Since the two axes are moving simultaneously, a cross-coupling interaction between them can arise. Thus, this must be analyzed (and compensated as necessary). An additional target is to achieve a high-bandwidth control. Hence, the resonant frequencies of the system must be identified in order to avoid movements that can break the manipulator.

1.4 OUTLINE OF THE CONTENT

This thesis is organized as follows:

- **Chapter 2**: in this chapter the theory behind the control algorithm employed in this thesis work is described.
- **Chapter 3**: in this chapter all components of the analyzed system are described and the related equations are provided. Moreover, both the linear and the non-linear models of the manipulator are described.
- **Chapter 4**: in this chapter a brief description of the control system designed by Marchi [8] for a high-performance, single-axis positioning system is reported. That work formed the starting point of this project work. Moreover, meaningful measurements performed on the one-axis system are also provided.
- **Chapter 5**: The high-precision positioning system was extended from one axis to two axes. In this chapter the performance associated to the added axis are shown. Moreover, new reference signals are designed in order to drive the system in such a way that

some significant shapes in the XY-plane are performed. The results achieved when moving both axes simultaneously are also shown in this chapter.

- **Chapter 6**: when both axes are moving simultaneously, two different kinds of cross-coupling interaction between them were detected: kinematic and kinetostatic cross-coupling. In this chapter, they are analyzed and possible compensation solutions are provided.

- **Chapter 7**: when periodic reference signal are used, the system performance can be improved using high-performance controllers, such as the repetitive control (RPC) and the iterative learning control (ILC). These controllers have been added to the control scheme of the system and the achieved results are shown and discussed in this chapter.

2 CONTROL THEORY

2.1 INTRODUCTION

Different techniques were used to control the system analyzed in this thesis work. This chapter briefly describes the basic theory behind them.
A control system usually is based on the simultaneous action of feedback and feed-forward control. In this way the advantages of both controllers are exploited.
The feedback controller action is based on the error between a reference and a measured signal. This technique tends to eliminate (or reduce) this error, and it reduces the influence of unmodeled error due to external disturbance or difference between the real system and its model. Unfortunately, due to measurement, the action of a feedback controller is slow and it exhibits transients. To reduce the transient time and therefore improve the control action, the feed-forward control is added.
The feed-forward control is a non error-based control action. This means that the action of this controller depends only on the knowledge of the system and not on the real-time measured signals. This knowledge can come from theoretical models and equations or from previous measurements of the system behaviour. Unfortunately, being based only on the knowledge of the system, and not on the real signal measurements, the feed-forward control is not robust to external noise and to possible differences between the model and the real system.
The combination of the two control models combines the advantages of the fast response of the feed-forward term and the high accuracy of the feedback term, which compensates the unmodeled effects of the physical system and the external disturbances [11].
Consequently, the control for both axes of the manipulator is based on a simultaneous action of feedback and feed-forward controllers. The feedback control is based on a PID controller, described in section 2.2. In the feedback control, the output signal $x(t)$ is compared with the reference $r(t)$ to produce the error signal $e(t) = r(t) - x(t)$, which is the controller input signal. The system output signal can be measured or estimated. In the positioning system studied, the feedback controller uses the position and velocity signals. The first one is directly measured by a linear encoder, while the second is estimated through an observer, which will be described in section 2.3.
The feed-forward control is based on the theoretical stiffness equa-

tion and it is described in section 2.4. Moreover, some experimental results show a cross-coupling interaction between the two axes and this behaviour is compensated using a feed-forward action.
With the target of drawing circumferences on the XY plane, sinusoidal reference signals were used on both axes. When periodic or repetitive reference signals are used, the control can be improved using Repetitive Control (RPC) or Iterative Learning Control (ILC) techniques, that will be explained in section 2.5 and 2.6, respectively. Both these methods enable the design of a new control signal starting from previous information and therefore they improve the control performance "learning" from experience [12].

2.2 PID CONTROL

The PID (Proportional Integral Derivative) controller is a feedback controller widely used in industrial applications. The PID controller's popularity can be due to both its functional simplicity and its robustness in a wide range of operating conditions [13]. The input of this controller is the error $e(t)$ between the reference and the measurement. As explained by the name, this controller processes the input error using a proportional, an integral and a derivative term. The time domain equation of the PID controller is:

$$PID(t) = K_p e(t) + K_i \int e(t)dt + K_d \frac{d}{dt} e(t) \tag{2.1}$$

In the Laplace domain this equation becomes:

$$PID(s) = K_p E(s) + K_i \frac{1}{s} E(s) + K_d s E(s) = K_p (1 + sT_d + \frac{1}{sT_i}) E(s) \tag{2.2}$$

where: $T_i = \frac{K_p}{K_i}$ is the integral time constant and $T_d = \frac{K_d}{K_p}$ is the derivative time constant.
The PID's gains need to be tuned in order to have the desired system response. Increasing the proportional gain K_p will increase the speed of the control system response; however, it will reduce the phase margin and therefore the system will tend to oscillate and then it will diverge as the gain increased further. The integral gain K_i sums the error over time and thus leads to eliminate the steady - state error. The bigger is this gain, the faster this action occurs, but the unwanted integrator wind-up effect increases. The derivative term is sensitive to the rate of change of the error signal. Increasing the derivative gain K_d will cause the control system to react more strongly to changes in the error term and so this increases the speed of the overall control system. Unfortunately, the derivative term amplifies the high frequency signals, thus the system is more sensitive at higher frequency noise [13].

There are different methods to tune the PID controller gains. The one used in this thesis work is the Ziegler-Nichols method. This heuristic method is performed initially by setting the integral and the derivative gains to zero ($K_i = K_d = 0$). In this configuration the proportional gain K_p is increased (starting from 0) until it reaches the ultimate gain K_u, at which the output of the control loop has a stable and consistent oscillation. Higher proportional gains will produce divergent oscillations. With the proportional gain set to K_u, the oscillation period T_u is measured. The PID gains are then calculated using table 2.1 and the values of K_u and T_u found [14].

Control type	K_p	T_i	T_d
PI	$0.45K_u$	$T_u/1.2$	-
Classic PID	$0.6K_u$	$T_u/2$	$T_u/8$
PID no overshoot	$0.2K_u$	$T_u/2$	$T_u/3$

Table 2.1: Ziegler-Nichols's Gains Table [14]

For the compliant mechanism studied in this thesis work, the overshoot could be a problem. Therefore, the "PID no overshoot" gains are chosen.

2.3 OBSERVER

The feedback control requires knowledge of the system output signals, which can be measured or estimated. The feedback signals used in the high-performance positioning system studied in this thesis work are the position and velocity signals. The system analyzed is equipped with a linear encoder which returns position measurements, but no velocity sensor is available and so the system velocity needs to be estimated. Velocity can be easily estimated through the derivative of the position signal. Unfortunately, this method provides poor results since it amplifies the wide band noise superimposed to the position signal. To overcome this problem, the feedback velocity signal is estimate through an observer.
All the theory behind the observer described in this section can be found in [15] and [8].

2.3.1 *Continuous Time Analysis*

The observer block diagram in the Laplace domain is shown in Figure 2.1. As can be seen, the observer estimates both the position and velocity signals via the following equations.

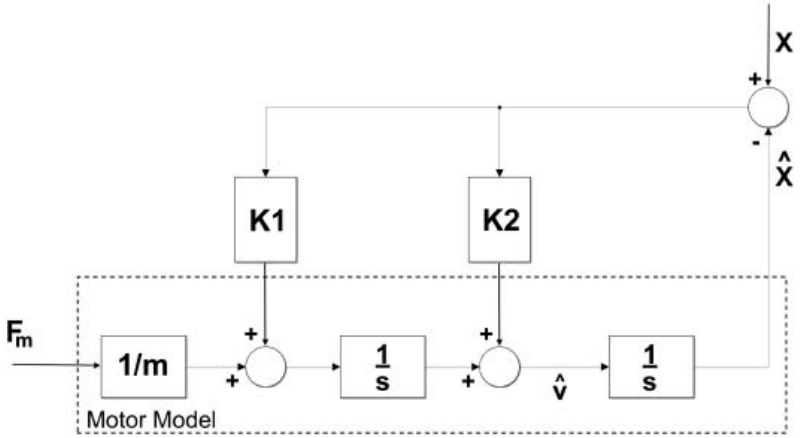

Figure 2.1: Observer Block Diagram in the Laplace Domain [8]

Neglecting the force feed-forward input, from the block diagram in Figure 2.1, we obtain:

$$\hat{x} = \frac{1}{s}[\frac{1}{s}K_1(x-\hat{x}) + K_2(x-\hat{x})] \tag{2.3}$$

Thus:

$$\hat{x} + \frac{1}{s^2}K_1\hat{x} + \frac{1}{s}K_2\hat{x} = \frac{1}{s^2}K_1x + \frac{1}{s}K_2x \tag{2.4}$$

Therefore:

$$\hat{x} = \frac{K_1 + K_2 s}{s^2 + K_2 s + K_1}x \tag{2.5}$$

Equation (2.5) is a second order system with: $K_1 = \omega_0^2$ and $K_2 = 2\rho\omega_0$, where: ω_0 is the natural frequency and ρ is the damping factor [8]. This transfer-function is the closed-loop observer transfer-function and therefore it defines the observer poles and consequently its dynamics.
Considering now the force feed-forward term, which acts to reduce the position transient error [8], the equation becomes:

$$\hat{x} = \frac{1}{s}[\frac{1}{s}(K_1(x-\hat{x}) + \frac{F_m}{m}) + K_2(x-\hat{x})] \tag{2.6}$$

Thus:

$$\hat{x} + \frac{1}{s^2}K_1\hat{x} + \frac{1}{s}K_2\hat{x} = \frac{1}{s^2}K_1x + \frac{1}{s}K_2x + \frac{1}{s}\frac{F_m}{m} \tag{2.7}$$

Therefore:

$$\hat{x} = \frac{K_1 + K_2 s}{s^2 + K_2 s + K_1} x + \frac{F_m/m}{s^2 + K_2 s + K_1} \tag{2.8}$$

As a consequence, the estimation error is:

$$x - \hat{x} = x - \frac{K_1 + K_2 s}{s^2 + K_2 s + K_1} x - \frac{F_m/m}{s^2 + K_2 s + K_1} \tag{2.9}$$

Or:

$$x - \hat{x} = \frac{s^2 + K_2 s + K_1}{s^2 + K_2 s + K_1} x - \frac{K_1 + K_2 s}{s^2 + K_2 s + K_1} x - \frac{F_m/m}{s^2 + K_2 s + K_1} \tag{2.10}$$

and therefore:

$$x - \hat{x} = \frac{s^2}{s^2 + K_2 s + K_1} x - \frac{\hat{a}}{s^2 + K_2 s + K_1} \tag{2.11}$$

where: $\hat{a} = \frac{F_m}{m}$ is the estimated acceleration.
Recognizing that $s^2 x$ is the Laplace term for the acceleration a:

$$x - \hat{x} = \frac{a}{s^2 + K_2 s + K_1} - \frac{\hat{a}}{s^2 + K_2 s + K_1} = \frac{a - \hat{a}}{s^2 + K_2 s + K_1} \tag{2.12}$$

2.3.2 *Discrete Time Analysis*

The control algorithm used in this thesis work is implemented in the discrete time domain using Matlab-Simulink. As described with the continuous time model, the velocity observer uses a second order model to estimate both position and velocity [15].
Figure 2.2 shows the observer block diagram in the Z-trasform domain.

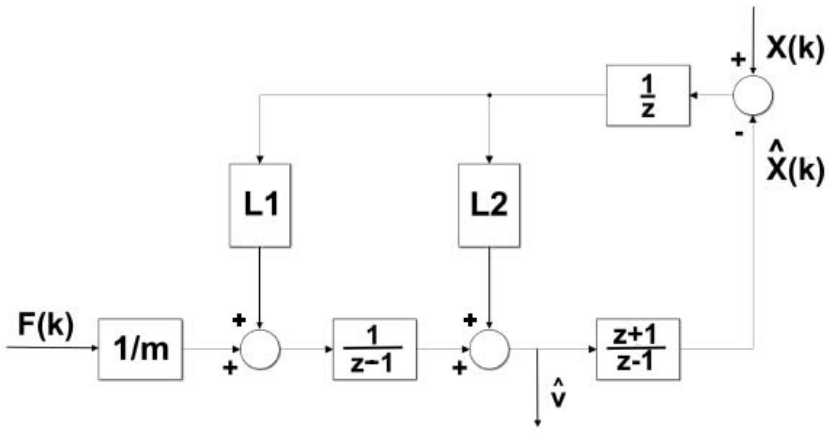

Figure 2.2: Observer Block Diagram in the Z-Trasform Domain [8]

In the discrete time domain, the block $\frac{z+1}{z-1}$ has a feedthrough path which results in an algebraic loop. To overcome this problem an extra delay element is introduced in the observer's error path [15] [8].
As was done before with the continuous time observer, the equation for the estimated position $\hat{x}$ can be evaluated by neglecting the feed-forward term:

$$\hat{x} = \frac{z+1}{z-1}\left(\frac{1}{z(z-1)}L_1(x-\hat{x}) + \frac{1}{z}L_2(x-\hat{x})\right) \tag{2.13}$$

Thus:

$$\left[1 + \frac{z+1}{z-1}\left(\frac{1}{z(z-1)}L_1 + \frac{1}{z}L_2\right)\right]\hat{x} = \frac{z+1}{z-1}\left(\frac{1}{z(z-1)}L_1 + \frac{1}{z}L_2\right)x \tag{2.14}$$

Furthermore:

$$\hat{x} = \frac{(z+1)(L_1 + L_2(z-1))}{z(z-1)^2 + (z+1)(L_1 + L_2(z-1))}x \tag{2.15}$$

Or:

$$\hat{x} = \frac{L_2z^2 + L_1z + L_1 - L_2}{z^3 + z^2(L_2-2) + z(L_1+1) + L_1 - L_2}x \tag{2.16}$$

Thus, due to the presence of a delay in the error path, the discrete time observer is no longer a second order system (as occurs in the continuous time domain), but a third-order system. As a consequence, tuning the observer gains in the discrete time domain is more difficult than in the continuous time domain. In [15] three sets of possible gains L_1 and L_2 were found:

Set	L_1	L_2
Low	0.01125	0.10
Medium	0.02473	0.1716
High	0.035	0.30

Table 2.2: Observer Gains Table [15]

In [15] the observer gain selection was obtained as a trade off between noise filtering and disturbance rejection. Indeed, the noise filtering requires lower gains, while the disturbance rejection is improved by increasing the gain value.

2.4 FEED-FORWARD CONTROL: NON LINEAR STIFFNESS AND CROSS-COUPLING

The two-axis high-performance positioning system has been controlled by applying different feed-forward controllers. The first one is a force

feed-forward control, based on the theoretical equations of the system (described in chapter 3). These equations evaluate the force needed to perform a certain movement on each axis, starting from the position, velocity and acceleration references.
Unfortunately, when both axes of the manipulator are moved simultaneously, two kinds of cross-coupling interaction arise between the two axes. The first one is the kinematic cross-coupling, which means that a movement of one axis produces an unwanted movement on the other axis. This effect was measured statically and its compensation was performed by modifying the input of the force feed-forward control, as it will be explained in chapter 6.
The second type of cross-coupling interaction is the kinetostatic cross-coupling. In fact, the force needed to feed one axis in order to obtain a specific displacement depends not only on that displacement, but also on the position of the orthogonal axis. This effect is theoretically described in [5] and the related equations will be reported in chapter 6. Moreover, the kinetostatic cross-coupling interaction was measured and the data collected allowed for the compensation of that effect.
Both the theoretical equations and the measurements show that the force needed to perform a movement on one axis is function of the position (x, y) of both axes. Therefore the force needed to perform a displacement on the X-axis can be expressed as:

$$F_x = f(x, y) \tag{2.17}$$

Since the effect of y on F_x is small compared to the effect of x, equation (2.17) can be approximated using the Taylor's series about $y = 0$ truncated to the first order term:

$$F_x = f(x, y) = f(x, 0) + f'(x, 0)y \tag{2.18}$$

The terms $f(x, 0)$ and $f'(x, 0)$ can be evaluated using the theoretical cross-coupling equation or experimental data. The same compensation approach can be used on all the system axes. In this way, the force feed-forward control has been modified by introducing the kinetostatic cross-coupling compensation.
Better approximations can be performed using higher order terms of the Taylor series about $y = 0$. However, on one hand, if the coefficients are evaluated from measurements, it would require more experimental data and an high repeatability of the system behaviour. On the other hand, if the coefficients of the Taylor series are evaluated from the theoretical model of the cross-coupling, significant modelling errors can arise thus making the contribution of higher order terms useless.
For the high-precision positioning system studied in this thesis work, the first order term of the Taylor series is sufficient to compensate the

kinetostatic cross-coupling interaction between the two axes of the system, as will be explained in chapter 6.

2.5 RPC: REPETITIVE CONTROL

The Repetitive Control (RPC) is an advanced control technique used when the reference is a periodic or repetitive signal, or to reject periodic or repetitive disturbances. In this thesis work the RPC has been used to improve the system's capability to follow periodic reference signals. The theory behind the RPC described in this section can be found in [16] and [17].
There are two hypothesis behind the RPC. The first one is the knowledge of the period of the periodic or repetitive signal (whether if it is the reference or the disturbance), which is assumed constant. The second hypothesis is the knowledge of the system model.
In the discrete time, a periodic signal with period NT, where N is the number of samples in a period and T is the sample time, can be represented as a delay chain with a positive feedback loop, as shown in Figure 2.3.

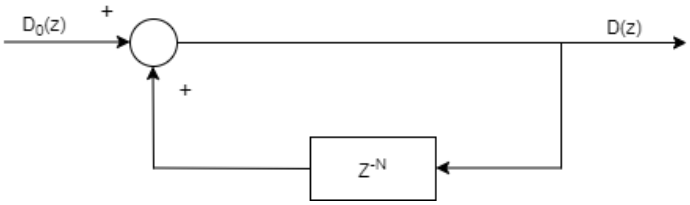

Figure 2.3: Discrete Time Periodic Signal [17]

Considering Figure 2.3, the periodic discrete time signal in the z-trasform domain can be expressed by:

$$D(z) = \frac{1}{1 - z^{-N}} D_0(z) \tag{2.19}$$

where: $D_0(z) = d_0 + d_1 z^{-1} + ... + d_{N-1} z^{N-1}$ represents the z-trasform of one period of the discrete time periodic signal and d_0, d_1,..., d_{N-1} are the N signal samples.
Therefore, the RPC structure has to be:

$$G_r(z) = T(z) \frac{1}{1 - z^{-N}} \tag{2.20}$$

The RPC is not the only controller of the system. Indeed it is added in parallel to another controller the task of which is to guarantee the stability of the controlled system and the pole allocation to achieve the desired dynamic performance. In such a way, the only requirement of the RPC is the minimization of the position error signal in the case of a periodic reference or the rejection of periodic disturbances.

Let us consider a generic causal continuous time system described by the open loop transfer function $G(s)$. The close loop transfer-function is:

$$W(s) = \frac{Y(s)}{R(s)} = \frac{G(s)}{1 + G(s)} \tag{2.21}$$

where $Y(s)$ and $R(s)$ are the output signal and the input reference signal in the Laplace domain, respectively. A block diagram of the RPC in the Laplace domain is shown in Figure 2.4. The additional input $U_r(s) = G_r(s)E(s)$ is added to the system with the aim of reducing the tracking error $E(s)$ in the case of a periodic or repetitive reference signal, or the effect of a periodic or repetitive disturbance $D(s)$.

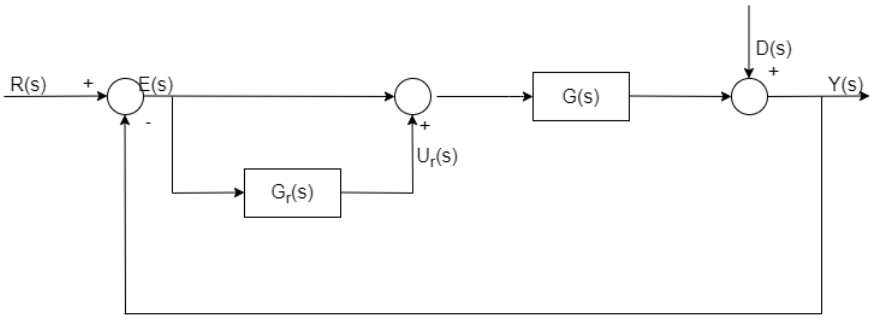

Figure 2.4: RPC block diagram in the Laplace domain [17]

Neglecting the disturbance $D(s)$ (as can be considered using the superposition principle), the output is expressed by:

$$Y(s) = G(s)U_r(s) + G(s)E(s) \tag{2.22}$$

If $R = 0$, the error $E(s)$ is: $E(s) = -Y(s)$ and therefore equation (2.22) becomes:

$$Y(s) = G(s)U_r(s) - G(s)Y(s) \rightarrow Y(s) = \frac{G(s)}{1 + G(s)}U_r(s) = W(s)U_r(s) \tag{2.23}$$

Using the same approach in the Z-trasform domain it can be shown that we obtain the discrete RPC block diagram reported in Figure 2.5, where $W(z)$ is the the close-loop transfer function in the Z-trasform domain:

$$W(z) = (1 - z^{-1})Z[\frac{W(s)}{s}] = \frac{z^{-d}B(z^{-1})}{A(z^{-1})} \tag{2.24}$$

where d is relative degree of the transfer-function.

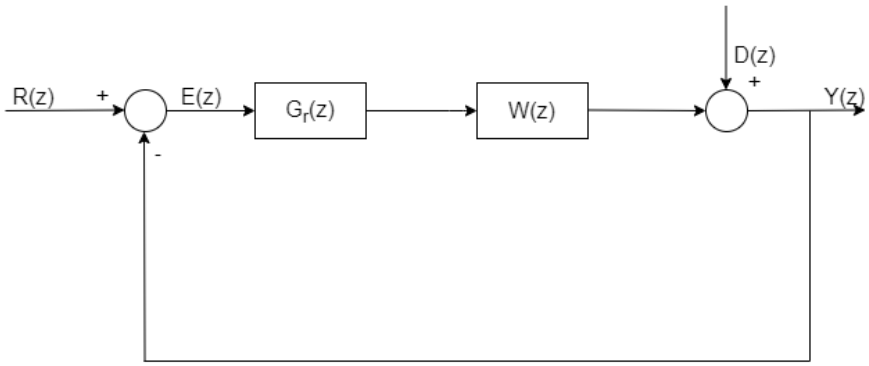

Figure 2.5: RPC block diagram in the Z-transform domain [17]

In [16] the following structure for the RPC controller was proposed:

$$G_r(z) = \frac{z^{-N}}{1 - z^{-N}} \frac{1}{W(z)} = \frac{z^{-N+d}}{1 - z^{-N}} \frac{A(z^{-1})}{B(z^{-1})} \tag{2.25}$$

The controller in equation (2.25) is realizable if $N > d$ and it is stable if the zeros of $B(z^{-1})$ are located inside the unit radius circumference. Assuming for the moment that this is true, we have:

$$G_r(z)W(z) = \frac{z^{-N+d}}{1 - z^{-N}} \frac{A(z^{-1})}{B(z^{-1})} \frac{z^{-d}B(z^{-1})}{A(z^{-1})} = \frac{z^{-N}}{1 - z^{-N}} \tag{2.26}$$

and the input-output transfer-function is:

$$\frac{G_r(z)W(z)}{1 + G_r(z)W(z)} = \frac{z^{-N}}{1 - z^{-N} + z^{-N}} = z^{-N} \tag{2.27}$$

Thus, the RPC introduces a one period delay.
Unfortunately, this structure of the repetitive controller $G_r(z)$ could be implemented only if all the zeros of the discrete close-loop transfer-function $W(z)$ are inside the unit radius circumference. This condition is not always verified. Moreover, if the relative degree of the continuous time transfer-function is equal or bigger than 3, then it can be shown that the corresponding discrete time transfer function has at least one zero outside the unit radius circumference. In addition, if the relative degree of the continuous time transfer-function is equal to 2, the corresponding discrete time transfer-function has a zero located on the unit radius circumference (limit condition for stability) [17].
In this case, the discrete time transfer-function $W(z)$ cannot be reversed because it has one or more unstable zeros and consequently the RPC controller structure reported in equation (2.25) cannot be used. To get around this problem, in [16] a new RPC controller structure, applicable also when the discrete time transfer function is not

reversible, was proposed. To that aim, let us first split the numerator of the close-loop discrete transfer-function $W(z)$ as a product of $B^+(z^{-1})$ and $B^-(z^{-1})$. The first term exhibits the m unstable zeros of $W(z)$ ($deg(B^+(z^{-1})) = m$), while $B^-(z^{-1})$ is stable. Thus, we have:

$$W(z) = \frac{z^{-d}B(z^{-1})}{A(z^{-1})} = \frac{z^{-d}B^+(z^{-1})B^-(z^{-1})}{A(z^{-1})} \tag{2.28}$$

The $G_r(z)$ controller proposed in [16] is:

$$G_r(z) = \frac{1}{1-z^{-N}} K_r \frac{z^{-N+d+m}A(z^{-1})z^{-m}B^+(z)}{bB^-(z^{-1})} \tag{2.29}$$

where:
- $\frac{1}{1-z^{-N}}$ is a common factor for all the repetitive controllers (as described before),
- K_r is the controller gain,
- z^{-N+d+m} is necessary for physical feasibility,
- $A(z^{-1})$ is the denominator polynomial of $W(z)$
- $b \geqslant max[B^+(e^{j\omega T})]^2$ with $0 \leqslant \omega T \leqslant \pi$,
- $N \geqslant d + m$ for the controller physical feasibility,
- $B^+(z)$ is equal to $B^+(z^{-1})$, where z^{-1} is substituted with z: $B^+(z)$ is not physically feasible, but $z^{-m}B^+(z)$ is physically feasible.

In [16] a theorem regarding the stability for this repetitive control system is provided. Let us determine the roots of $1 + G_r(z)W(z)$, that is the denominator of the close loop transfer-function:

$$\begin{aligned} 1 + G_r(z)W(z) &= 1 + \frac{1}{1-z^{-N}} K_r \frac{z^{-N+d+m}A(z^{-1})z^{-m}B^+(z)}{bB^-(z^{-1})} \frac{z^{-d}B(z^{-1})}{A(z^{-1})} = \\ &= 1 + K_r z^{-N} \frac{B^+(z)B^+(z^{-1})}{b(1-z^{-N})} = \\ &= 1 + z^{-N}[K_r \frac{B^+(z)B^+(z^{-1})}{b} - 1] = \\ &= 0 \end{aligned} \tag{2.30}$$

Equation (2.30) can be represented by the system of Figure 2.6, that does not have instable poles. Therefore, using the Small Gain Theorem [18], the system is stable if the following constraint is satisfied:

$$\left| z^{-N}[K_r \frac{B^+(z)B^+(z^{-1})}{b} - 1] \right| < 1 \tag{2.31}$$

Since $|z^{-N}| \leqslant 1$, the system stability is guaranteed if:

$$\left| K_r \frac{B^+(z)B^+(z^{-1})}{b} - 1 \right| < 1 \tag{2.32}$$

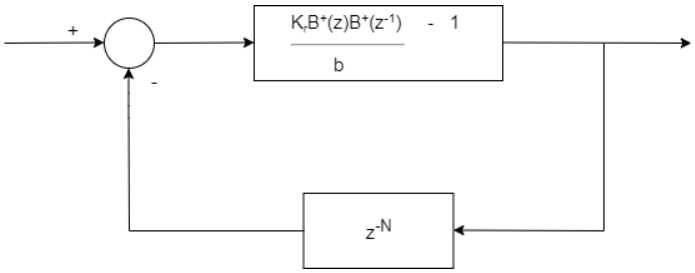

Figure 2.6: Equivalent feedback system for stability analysis [16]

Since for $z = e^{j\omega T}$, we have $B^+(z)B^+(z^{-1}) = |B^+(e^{-j\omega T})|^2$. Defining:

$$\frac{|B^+(e^{-j\omega T})|^2}{b} = a \tag{2.33}$$

and remembering that for definition $b \geqslant max|B^+(e^{-j\omega T})|^2$, then we have $a \leqslant 1$. Consequently the problem becomes:

$$|K_r a - 1| < 1 \tag{2.34}$$

which yields:

$$0 < K_r < 2 \tag{2.35}$$

In conclusion, the RPC controller has to be added in parallel to the feedback controller, which is usually already implemented on the system to guarantee the system stability and the desired dynamics. A schematic structure is shown in Figure 2.7, where the controller block G_r implements equation (2.29) and it is stable if: $0 < K_r < 2$.

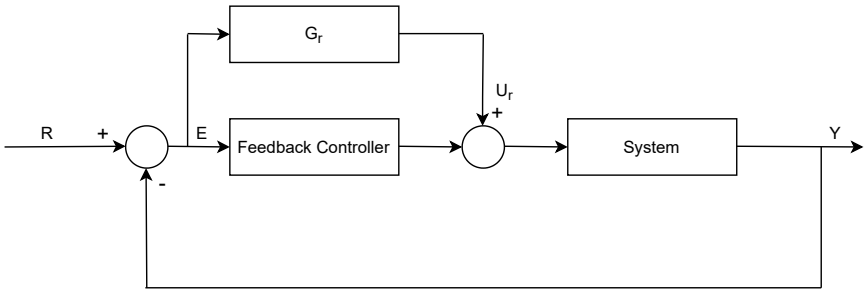

Figure 2.7: RPC Structure Scheme

2.6 ILC: ITERATIVE LEARNING CONTROL

The Iterative Learning Control (ILC) is an advanced control technique used when the reference is a periodic or repetitive signal, or to reject periodic or repetitive disturbances. In this thesis work the ILC has been used to improve the system's capability to follow periodic refer-

ence signals. The theory behind the ILC described in this section can be found in [17], [12] and [19].
This high-performance control technique is based on the idea that it is possible to improve the behaviour of a system that perform the same operation multiple times by learning from previous executions. This is because for a system that executes the same task repeatedly and under the same operating condition, the non-learning controller produces the same tracking error each time. This error signal is rich in information and can be used to improve the control performance [19].
A single repetitive movement is called a batch.
The ILC is typically implemented in the discrete time because it requires the storage of the error samples related to the last input cycle. [19].
The control objective is to ensure that the system output signal $y(k)$ tracks the input reference signal $r(k)$. Thus, the tracking error signal related to the i-th batch, is defined as:

$$e(k,i) = r(k) - y(k,i) \tag{2.36}$$

The concept is to reduce that error by exploiting the recorded values of the tracking error signal $e(k,i-1)$ and the input signal $u(k,i-1)$ corresponding to the previous batch. In the simplest ILC formulation, called proportional-type ILC (P-type ILC), the input of the current batch ($u(k,i)$) is obtained by adding the input signal of the previous batch ($u(k,i-1)$) and a contribution proportional to the tracking error of the previous batch ($e(k,i-1)$) [12]:

$$u(k,i) = u(k,i-1) + K_{ILC}e(k,i-1) \tag{2.37}$$

This type of ILC is the one used in this thesis work. Other more complex types of ILC can be found in [12] and [19].
Theoretically, the updating expression (2.37) should converge to a zero tracking error signal.

As explained in [19], in most physical implementations the ILC is used in combination with an already existing feedback controller. In [19] two ways to combine the two controllers are proposed. In the first arrangement, the ILC is connected in series with the feedback controller, while in the second one it is connected in parallel. According to this latter architecture, schematized in Figure 2.8, the ILC output signal u_{ILC} directly alters the control signal to the plant and therefore when the ILC controller improves the system performance and reduces the tracking error, the feedback controller will apply less effort. In this thesis work, the parallel approach was used.

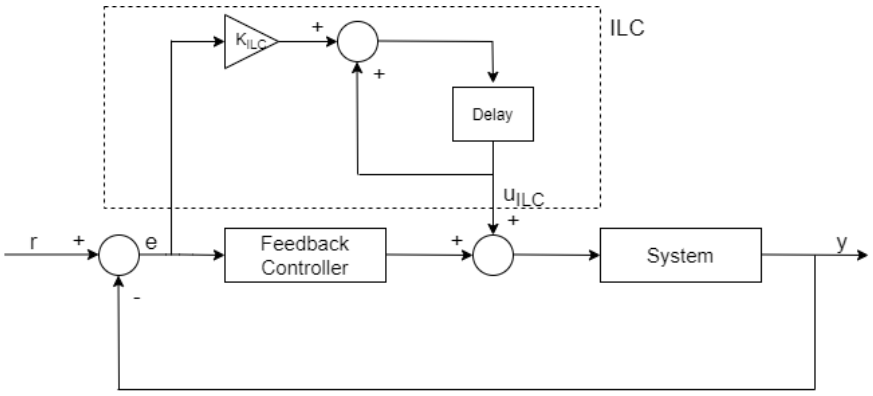

Figure 2.8: ILC Structure Scheme

3 SYSTEM DESCRIPTION AND MODEL

3.1 INTRODUCTION

The system analyzed in this thesis work is a high-performance compliant positioning manipulator. The system is designed with a compliant mechanical structure in order to achieve high performance movements, with resolution, accuracy and precision of the order of several nanometers. Unfortunately, due to the electrical noise of the amplifier adopted, the system is limited to movements with micrometer accuracy.
In this chapter, the main components of the manipulator are described and a system model is given. The manipulator is composed of:

- Mechanical Structure
- Voice Coil Actuator
- Linear Encoder
- Servo Amplifier
- Power Supply
- Controller Board, including a dSPACE controller with 64-bit floating-point processor
- Computer with Matlab 2013b and Simulink

These components will be described in detail in the next sections.
The system is composed by two orthogonal axes designed identically. Some of the components listed above are shared between the two axes. These are: power supply, controller board and computer. The non-shared components are: actuator, encoder and servo amplifier. The mechanical structure is composed by three parts, as will be described in section 3.2: Compliant Basic Parallelogram Mechanism (CBPM), XYZ Compliant Parallel Manipulator (CPM) and a base frame. The former and the base are duplicated separately on both axes, while the CPM is shared between the two axes.

Figure 3.1 shows the block diagram of one axis in which the method of connection of the system components is explained. While Figure 3.2 is a photo of the system, showing the mechanical structure (with actuators and encoders), the dSPACE board and the two servo amplifiers.

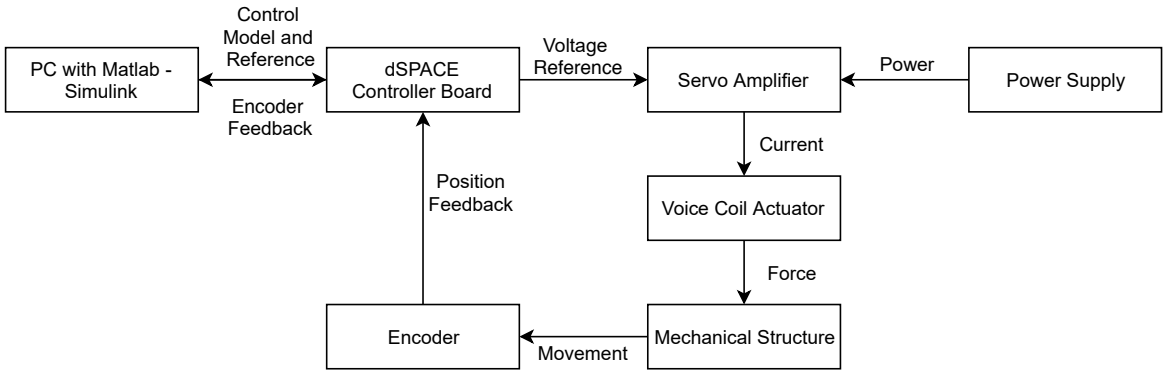

Figure 3.1: One Axis Block Diagram

Figure 3.2: Photo of the System

3.2 MECHANICAL STRUCTURE

The mechanical structure of the system is composed by three main parts: a Compliant Basic Parallelogram Mechanism (CBPM, described in subsection 3.2.1), a fully symmetrical XYZ Compliant Parallel Manipulator (CPM, described in subsection 3.2.2) and a base frame (described in subsection 3.2.3).
All the components are made of Aluminium 6061 (Young's Modulus E = 69000MPa).
Figure 3.3 shows a photo of the system with labeled components.

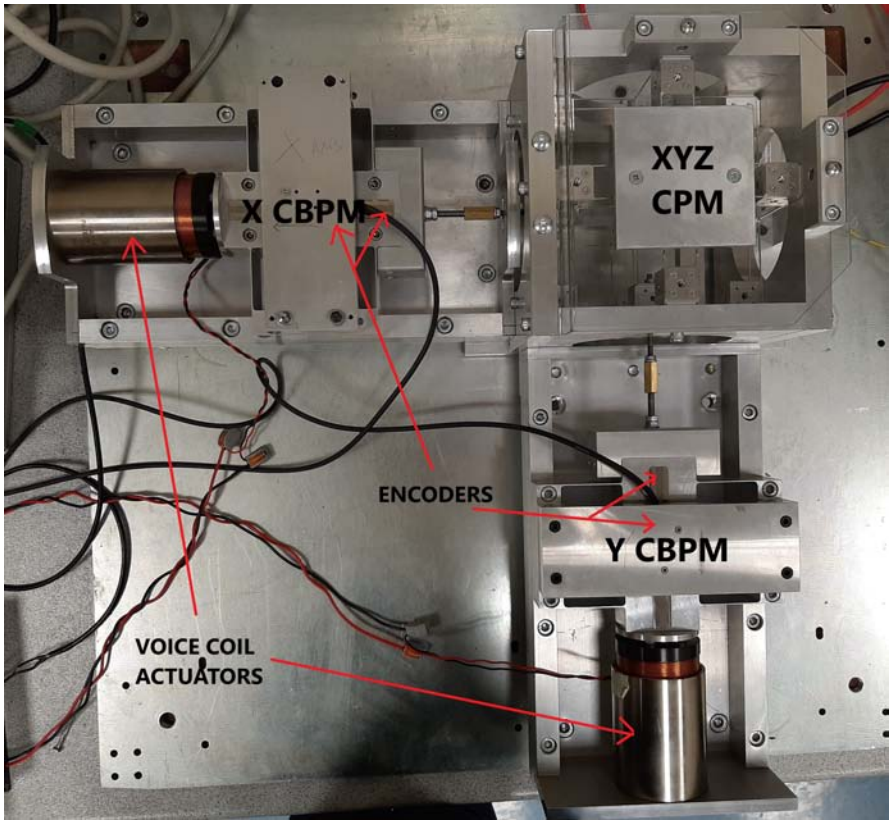

Figure 3.3: Photo of the System

3.2.1 *Compliant Basic Parallelogram Mechanism (CBPM)*

The Compliant Basic Parallelogram Mechanism (CBPM) is an example of a compound parallel mechanism, which consists of two identical Basic Parallelogram Mechanisms (BPMs), arranged in a mirror-symmetrical configuration [20]. The CBPM is a compliant version of the traditional prismatic-joint mechanism, which has good characteristics, such as: alleviated stress concentration, simple symmetrical structure, non-underconstrained design, large parasitic motion stiffness, mitigated buckling and avoidance of thermal sensitivity. Unfortunately, the CBPM stiffness exhibits non-linear characteristics [20],

[8].
A CBPM Representation, of the two BPMs that comprise it and a Photo are shown in Figure 3.4.

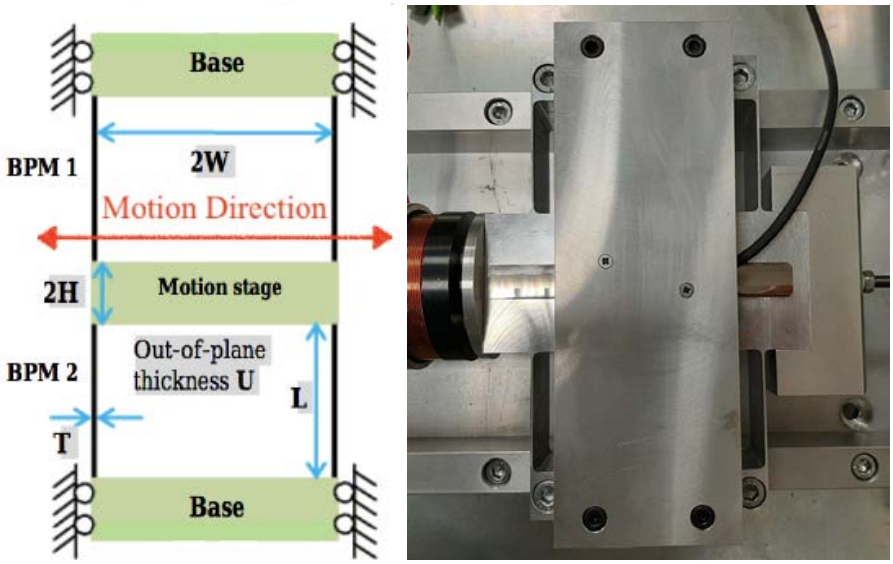

Figure 3.4: CBPM Representation [8] and Photo

This compliant component is needed in the system to constrain the motion of the Voice Coil Actuator to the axial direction, to prevent its damage. Moreover, the CBPM increases the overall stiffness of the system to an appropriate value for the actuator size [8]. Furthermore, a bigger stiffness ensure also a better dynamic performance [10].
Referring to Figure 3.4, the CBPM sizes are:

- W_{CBPM} = half of the spanning size = 50 mm
- H_{CBPM} = thickness of the moving stage = 60 mm
- T_{CBPM} = beam in-plane thickness = 1 mm
- L_{CBPM} = beam actual length = 50 mm
- U_{CBPM} = beam out-of-plane thickness = 40 mm

3.2.2 *XYZ Compliant Parallel Manipulator (CPM)*

The shared member between the two axes of the mechanical structure is the fully symmetrical XYZ Compliant Parallel Manipulator, described in [21]. It has desired motion characteristics such as: reduced cross-axis coupling, minimized lost motion, and relatively small parasitic motion. These CPM motion characteristics are derived from both its symmetric configuration and the rigid linkage between non-adjacent rigid stages [21]. The XYZ CPM is shown in Figure 3.5. In the representation on the left side F_y is the actuating force originating

from the CBPM component. The image in Figure 3.5 (a) is a disassembled representation and Figure 3.5 (b) shows the beams involved in the motion along only one axis. As can be seen in Figure 3.5, 24 beams contribute to the stiffness of the actuated axis [10].

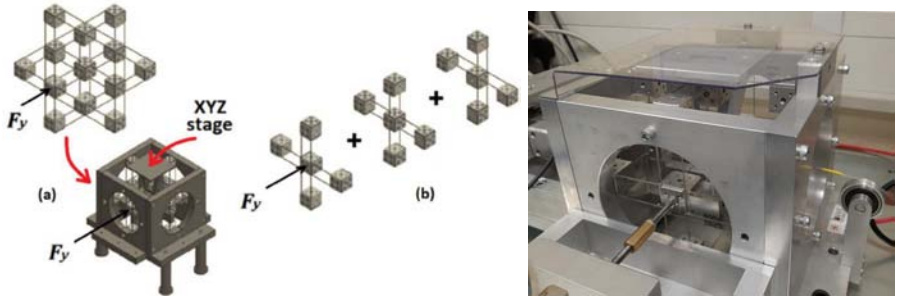

Figure 3.5: XYZ CPM Representation [22] and Photo

The design of the XYZ Compliant Parallel Manipulator provides three DOF (Degree of Freedom) with maximal decoupled motion along the three axes. Consequently, each axis to be moved requires an actuator and a CBPM component. Figure 3.6 shows the XYZ CPM with the three axes highlighted (a) and a motion along the X-axis (b) [21].

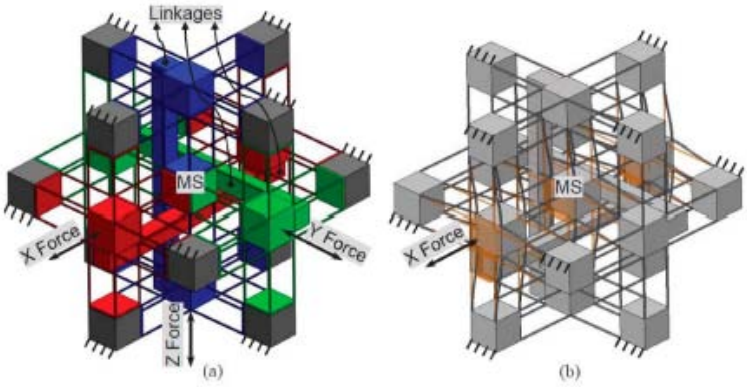

Figure 3.6: XYZ CPM with the three axes highlighted (a) and the motion along the X-axis (b) [21]

Due to symmetry and decoupled motion along the two axes, each axis can be controlled separately with the same control strategy. Unfortunately, there is a small coupling interaction between two axes, that need to be considered when controlling the system. This will be discussed, analyzed and compensated for in chapter 6.
The XYZ CPM beams sizes are:

- U_{XYZ} = beam width = 1 mm
- T_{XYZ} = beam thickness = 1 mm
- L_{XYZ} = beam length = 50 mm

3.2.3 *Base Frame*

The function of the base frame is to support and connect the compliant structure (CBPMs and XYZ CPM), the voice coil actuators and the encoders. To reduce vibrations on the mechanism, suitable anti-vibrational feet are used; the chosen ones are the DSD 40(60Sh) produced by AMC [10].

3.3 VOICE COIL ACTUATOR

The actuator chosen for both system axes is a voice coil actuator (VCA), model LA30-48-000A manufactured by BEI Technologies INC; a picture of it is shown in Figure 3.7, together with a schematic representation of the actuator [23]. Voice coils are direct drive linear motors and are hysteresis-free, frictionless and cog-free. Due to these characteristics they are the best choice for a large-range high-precision positioning system. Unfortunately these actuators cannot tolerate transverse force; for this reason the CBPM is required for both axes.

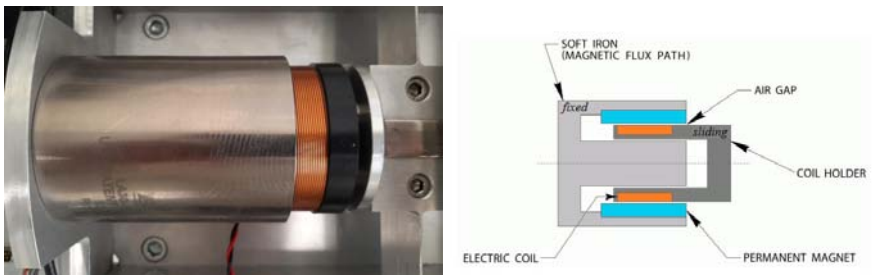

Figure 3.7: Voice Coil Actuator: Photo and Scheme [23]

Voice Coil Actuators are made up by two main parts: a coil and a permanent magnet. In the system studied, the coil is the moving part connected to the compliant mechanism and the permanent magnet is fixed on the aluminium frame. Voice Coil Actuators work on a principle based on the Lorenz force. According to this principle, if a current-carrying conductor is placed in a magnetic field, a force will act on it. These actuators utilize a magnetic field and a coil winding (conductor) to produce a force that is proportional to the current applied to the coil [24]. The linear equation (3.1) for the actuation force is:

$$F = (kBLN)i = K_f i \tag{3.1}$$

where:
- k = Force Costant [Nm^{-1}],
- B = Magnetic Flux Density [T],
- L = Length of Wire [m],
- N = Number of Conductors,
- i = Current [A],

and
- K_f = Force Sensitivity = 35.14 [NA^{-1}] for the VCA used.

On the physical system studied, the VCA coil is directly connected to the compliant mechanism. Consequently, the force produced by the actuator is directly apply to the compliant structure.
The actuator specifications are shown in table 3.1.

Winding Constants *	Units	Tol	Symbol	Wdg A
DC Resistance	Ohms	± 12.5%	R	2.6
Voltage @ F_P	Volts	Nominal	V_P	33.0
Current @ F_P	Amps	Nominal	I_P	12.7
Force Sensitivity	LB/Amp	± 10%	K_F	7.9
	N/Amp	± 10%		35.14
Back EMF Constant	V/(ft/sec)	± 10%	K_B	10.71
	V/(m/sec)	± 10%		35.14
Inductance ****	milli-henry	± 30%	L	2.9

Linear Actuator Parameters *	Units	Symbol	Value
Peak Force **	LB	F_P	100
	N		445
Continuos Stall Force ***	LB	F_{CS}	30.1
	N		133.8
Actuator Constant	LB/$\sqrt{Watt}$	K_A	4.9
	N/ $\sqrt{Watt}$		21.8
Electrical Time Constant	milli-sec	τ_E	1.12
Mechanical Time Constant	milli-sec	τ_M	1.57
Theoretical Acceleration	ft/sec^2	α_T	1962.2
	m/sec^2		598.1
Max Theoretical Frequency @ Full Stroke & Sinusoidal/Triangular Motion	Hz	f_{max}	34.5/38.4
Power I^2R @ F_P	Watts	P_P	419
Stroke:	± in		0.5
	± mm		12.7
Clearance on Each side of Coil	in		0.02
	mm		0.51
Thermal Resistance of Coil in still air	°C/Watt	Θ_{TH}	2.3
Maximum Allowable Coil Winding Temp	°C	Temp	155
Weight of Coil Assembly	LB	WT_C	1.64
	G		744
Weight of Field Assembly	LB	WT_T	4.95
	KG		2.25

* AT MID-STROKE POSITION AND @ 25°C AMBIENT TEMPERATURE
** 10 SECONDS @ 25°C AMBIENT & 155°C COIL TEMPERATURE
*** @25°C AMBIENT & 155°C COIL TEMPERATURE
**** MEASURED AT 1000 Hz.

Table 3.1: Specification of the Voice Coil Actuator [25]

3.4 LINEAR ENCODER

High-precision positioning systems require high resolution encoders. The most accurate relevant encoders are optical linear encoders and consequently they dominate the high resolution market.
The optical linear encoders used in both system axes are the: SI-HN-4000-01-0-FN-403-003-3, readhead number SRO15A, by Renishaw. One of these encoders is shown in Figure 3.8. The encoder resolution is 5

nm and it responds to changes of at most 0.135 ms^{-1}. The encoder resolution does not limit the quality of the measurement because it is dominated by the output noise of the amplifier, as written in section 3.5. The datasheet of the encoder can be found in [26].

Figure 3.8: Optical Linear Encoder: Real Photo and Datasheet Image[26]

This optical encoder is composed of two components: a readhead and a scale. The scale is fixed on the CBPM joint and consequently it moves together with the axis. Thanks to the characteristics of the compliant component, the lost motion of the axis is negligible and for this reason the position read by the encoder mounted on the CBPM represents the position of the XYZ compliant joint. The readhead, which reads the position from the scale, is fixed on a support directly above the CBPM compliant mechanism (The distance between the readhead and the scale must be in the range 0.8 ± 0.08 mm [26]). The encoder output is connected to the encoder input on the dSPACE controller board and its feedback signal allows the creation of a closed loop control system by using Matlab/Simulink running on the computer.
Moreover, Renishaw provides the SIGNUM software that can be used to read the encoder output signal strength, to configure the components and to verify their correct installation [27].

3.5 SERVO AMPLIFIER

The voltage provided by the DAC output of the dSPACE controller board needs to be converted into a current that feeds the voice coil actuator. This action is performed by a brushless PWM servo amplifier for both axes. The B25A20 by Advanced Motion Control, shown in Figure 3.9, is used. Its specifications are shown in table 3.2, while the datasheet of this component can be found in [28].

Table 3.2 shows that the device allows four operating modes. In order to have an output current proportional to the input voltage, the current mode was used for both the servo amplifiers. The corresponding I/O relationship is (3.2):

$$i = K_d v \tag{3.2}$$

Figure 3.9: Brushless PWM Servo Amplifiers

where:
- i is the output current [A],
- K_d is the amplifier gain [A/V],
and
- v is the input voltage [V].

The value of the gain K_d between the voltage input and the current output was determined experimentally for both servo amplifiers as: 1.804 A/V and 1.615 A/V for the X-axis and the Y-axis amplifier, respectively.
The system resolution is limited by the output electrical noise of the amplifiers, whose amplitude has been experimentally determined and it resulted around 0.2µm and 0.5µm for the X-axis and the Y-axis, respectively.

Power Specifications		
Description	Units	Value
DC Supply Voltage Range	VDC	40 - 190
DC Bus Over Voltage Limit	VDC	195
Maximum Peak Output Current[1]	A	25
Maximum Continuous Output Current	A	12.5
Maximum Continuous Output Power	W	2256
Maximum Power Dissipation at Continuous Current	W	119
Minimum Load Inductance (Line-To-Line)[2]	µH	250
Low Voltage Supply Outputs	-	±10 VDC (3 mA), +6 VDC (30 mA)
Switching Frequency	kHz	22
Control Specifications		
Description	Units	Value
Command Sources	-	±10 V Analog
Feedback Supported	-	Halls, Tachometer (±60 VDC)
Commutation Methods	-	Trapezoidal
Modes of Operation	-	Current, Hall Velocity, Duty Cycle, Velocity
Motors Supported	-	Single Phase (Brushed, Voice Coil, Inductive Load), Three Phase (Brushless)
Hardware Protection	-	Invalid Commutation Feedback, Over Current, Over Temperature, Over Voltage, Short Circuit (Phase-Phase & Phase-Ground)
Primary I/O Logic Level	-	5V TTL

Table 3.2: Specification of the Servo Amplifiers [28]

3.6 POWER SUPPLY

The power supply used in the system is the SM 52-30 by Delta Elektronika. The voltage range is: $0 - 52$ V and the current range is: $0 - 30$ A. A photo of the power supply employed is shown in Figure 3.10.

Figure 3.10: Power Supply

3.7 DSPACE CONTROLLER BOARD

The DS1104 R&D Controller Board allows the upgrading of the PC to a development system for rapid control prototyping. It is a single-board system with real-time hardware and comprehensive I/O. This controller is connected to the PC through a PCI (Pheripheral Component Interconnect) interface. Using the dSPACE ControlDesk 5.4 software, that interface allows uploading of the control programs developed in Matlab/Simulink on the board and real-time visualization on the PC of acquired data.
All the characteristics of the dSPACE controller board can be found in [29]. It has several input and output devices, such as:

- 8 ADC (Analog to Digital Converter) input
- 8 DAC (Digital to Analog Converter) output
- a Digital I/O connector
- a I/O Slave DSP
- 2 Digital incremental encoder interface
- 2 Single UART serial interface connectors

This thesis work used two DAC outputs and two encoder inputs, as shown in Figure 3.11.

The DAC outputs are used to convert the digital voltage reference values returned by the control model developed in Simulink, to the analog voltage signals that feed the amplifiers. The DACs have a resolution of 16 bits and an output range of ± 10V. Moreover, since the DAC exhibits a gain of 10, a factor equal to 0.1 is added before the DAC block in the Simulink model, as shown in Figure 3.13.
The system position is acquired by the optical linear encoders and forwarded to the computer. It has 24 bit resolution and selectable

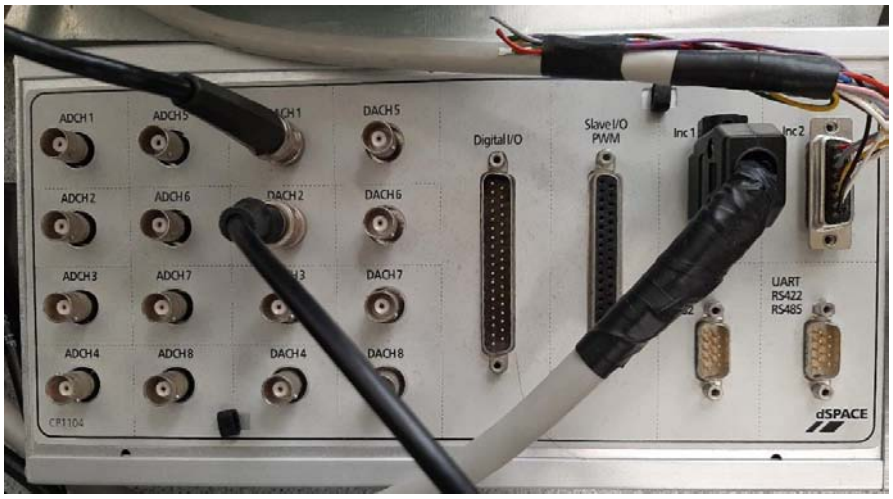

Figure 3.11: dSPACE DS1104 controller board with amplifiers and encoders connections

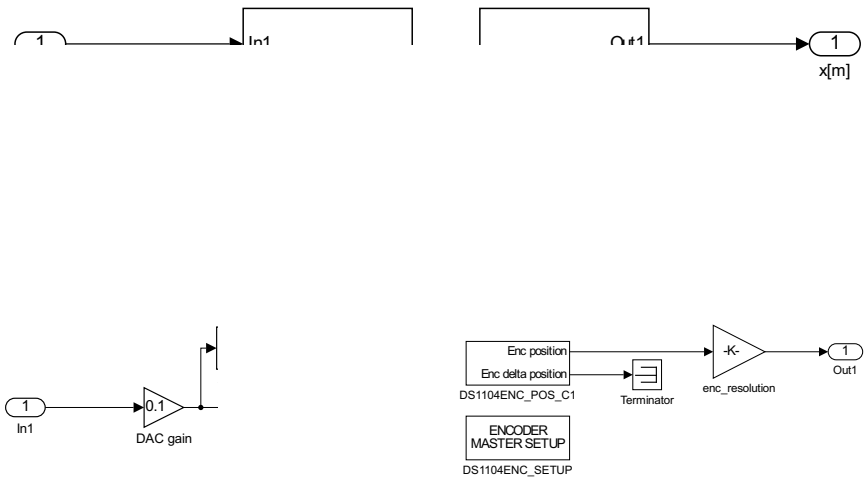

Figure 3.13: dSPACE DS1104 DAC and Encoder blocks implementation in Simulink

Figure 3.13 shows that only one block is needed to drive to the chosen DACH channel. Instead, the encoder input requires two blocks. In particular, the Encoder Master Setup Block allows the choice of the global encoder settings, such as the type of input (single-ended

TTL or differential RS422), while the Enc position/Enc delta position block provides read access to the position and delta position of the encoder interface channel (here the channel number must be choose). The scope added between the DAC gain and the DAC block allows the signal on the controller board to be viewed. Without that scope, no signal was available on the DAC output of the dSPACE board, so that the system was not driven. Moreover, the gain after the Enc position is required to convert the encoder output, expressed in encoder lines, in meters.
Once the Simulink control model is designed, it has to be built and downloaded on the DS1104 controller board, in order to work with the dSPACE ControlDesk 5.4 software.

3.7.1 *dSPACE ControlDesk 5.4 Software*

The dSPACE ControlDesk 5.4 software [30] represents the PC graphical interface between the controller board and the user. It allows a real-time communication between the PC and the dSPACE Controller Board. Moreover, this software permits the real-time visualization and storage of the measured signals and the variation of the model parameters. The measured signals can be exported in Matlab to be analyzed in depth, or plotted on a graph.

3.8 SYSTEM MODEL

The real system exhibits a non-linear behavior due to the compliant mechanism stiffness. According to [22], non-linearity can be neglected when the axis movement is up to ± 0.2 mm. In this range of movements, each axis can be modelled as a Mass-Spring-Damper system and it is possible to represent it with a linear transfer function between the voltage input (from the DAC on the dSPACE Controller Board) and the position signal output returned by the encoder. This model will be described in subsection 3.8.1. When the displacements are larger than ± 0.2 mm, the stiffness non-linearity cannot be neglected, this will be analyzed in subsection 3.8.2.

3.8.1 *Linear Model*

According to [8], in the linear range each axis can be modelled as a Mass-Spring-Damper system, shown in Figure 3.14.

Applying the Newton's law to the system in Figure 3.14, the following equation can be obtained:

$$F(t) + F_e(t) + F_v(t) = m_{tot}\ddot{x}(t) \tag{3.3}$$

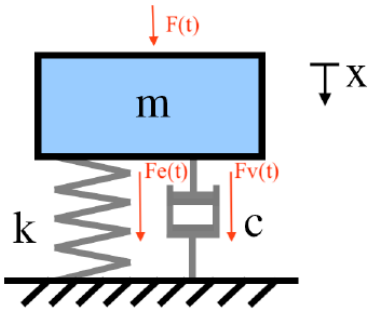

Figure 3.14: Mass-Spring-Damper System [8]

where:
- $F(t)$ is the force produced by the actuator [N],
- $F_e(t)$ is the elastic force [N],
- $F_v(t)$ is the viscous force [N],
- m_{tot} is the total mass of one axis [kg],
and
- $\ddot{x}$ is the acceleration of the system [m/s^2].
The force produced by the actuator can be expressed by combining the equations (3.1) and (3.2):

$$F(t) = K_f i(t) = K_f K_d v(t) \tag{3.4}$$

Moreover, the elastic force and the viscous force are:

$$F_e(t) = -k_t x(t) \qquad F_v(t) = -c\dot{x}(t) \tag{3.5}$$

where: k_t is the axis stiffness and c is the viscous damping coefficient. Therefore, each axis can be represented by the following equation:

$$F(t) = K_f K_d v(t) = m_{tot}\ddot{x}(t) + c\dot{x}(t) + k_t x(t) \tag{3.6}$$

Expressing this equation in the Laplace domain:

$$F(s) = K_f K_d V(s) = m_{tot}s^2 X(s) + csX(s) + k_t X(s) \tag{3.7}$$

Thus the axis linear transfer function is expressed by:

$$\frac{X(s)}{V(s)} = \frac{K_f K_d}{m_{tot}s^2 + cs + k_t} \tag{3.8}$$

The transfer-function numerators are different for the two axes due to the different servo amplifier gains K_d. They are equal to 1.804 A/V and 1.615 A/V for the X-axis and the Y-axis amplifiers, respectively. The axis stiffness in the linear range was theoretically and experimentally evaluated in [10] for the X-axis. The resulting experimental value is equal to 129.46 N/mm. The Y-axis linear stiffness was

supposed to be equal to that of the X-axis one due to the same axis structure. Moreover, the linear model is valid only in a small range and for this reason the small difference between the stiffness of the two axes is less relevant than the non-linear behaviour of the system. In the same paper [10], the the viscous damping coefficient was also evaluated on the basis of the damping factor estimated through the logarithmic decrement method. The estimated damping factor was: ξ = 0.023 and, consequently, the following viscous damping coefficient resulted: $c = 2\xi\sqrt{k_t m_{tot}} = 22.35\sqrt{kgN/m}$. Moreover, the axis total mass is 1.824 kg.
Using the above values in equation (3.8) the voltage/position transfer-functions of the two axes are:

$$\frac{X_x(s)}{V_x(s)} = \frac{K_f K_{dx}}{m_{tot}s^2 + cs + k_t} = \frac{35.14 \cdot 1.804}{1.824s^2 + 22.35s + 129460} \tag{3.9}$$

$$\frac{X_y(s)}{V_y(s)} = \frac{K_f K_{dy}}{m_{tot}s^2 + cs + k_t} = \frac{35.14 \cdot 1.615}{1.824s^2 + 22.35s + 129460} \tag{3.10}$$

for the X-axis and the Y-axis, respectively.

The bode diagram of the X-axis transfer-function is shown in Figure 3.15. The bode plot of the Y-axis transfer-function is very similar, since there is only a small difference in the DC gain of the two systems.

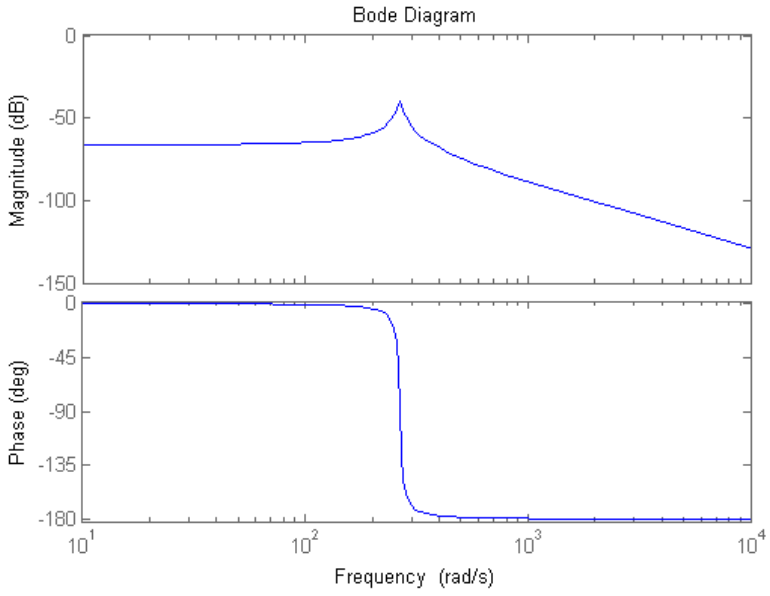

Figure 3.15: Bode diagram of the X-axis transfer-function

The first resonance frequency can be evaluated using equation (3.11) and can be verified using the bode plot. The resonance frequency is

the same for both axes because the denominator coefficients are identical.

$$w_n = \sqrt{\frac{K_t}{m_{tot}}} = \sqrt{\frac{129460}{1.824}} = 266.413 \text{rad/s} = 42.40 \text{Hz} \qquad (3.11)$$

3.8.2 *Non Linear Model*

Since the CBPM stiffness non-linearity cannot be neglected for displacements larger than ± 0.2 mm, a non-linear model of the system must be identified.
In [31] the non-linear model for the CBPM is explained and the non-linear equation for the CBPM stiffness was obtained. In this section, these equations are reported and the non-linear model of the system (considering also the XYZ component) is shown.
In [31] a kinematostatic modelling is employed to capture the load-displacement relationship of the CBPM. Both load and displacement are defined at the centre of the motion stage, as shown in Figure 3.16. The CBPM equations reported refer to this Figure.

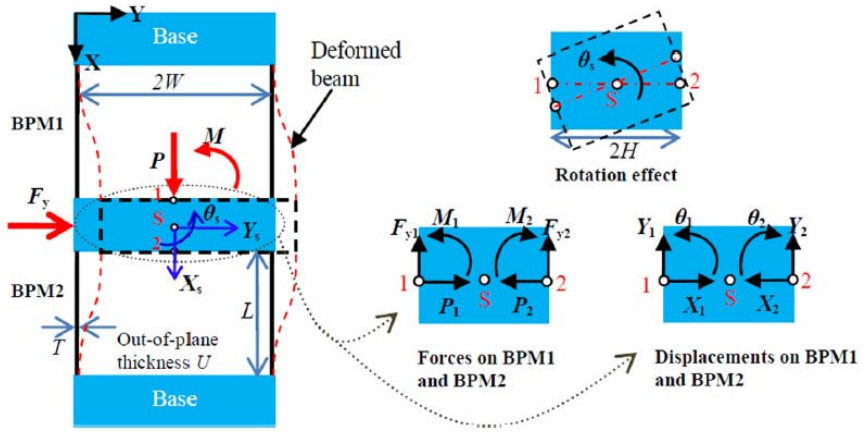

Figure 3.16: CBPM with actual geometry, loading and displacement indication [31]

In this paper, a normalization strategy was employed: all the translational displacements and length parameters are normalized to the beam actual length L, while the forces and the moments are normalized by EI/L^2 and EI/L, respectively, where E is the Young's modulus and I is the second moment of area of a rectangular cross-section ($I = \frac{1}{12}WT^3$). All the normalized parameters are denoted by the corresponding lower-case letters. In [31] it has been shown that the normalized primary translational motion (y_s) of the CBPM can be expressed by:

$$y_s = \frac{f_y}{48 + 1.2(\frac{2.4y_s^2}{1/d + y_s^2/700})} \qquad (3.12)$$

where:
- f_y is the normalized primary force
and
- $d = \frac{12}{(T/L)^2}$, where T is the beam in-plane thickness and L is the beam length.
Therefore, the normalized primary actuation force f_y is:

$$f_y = 48y_s + \frac{2.88y_s^3}{\frac{1}{d} + \frac{y_s^2}{700}} \tag{3.13}$$

Considering the normalization factors, we have:

$$\frac{F_y}{(\frac{EI}{L^2})} = 48\frac{Y_s}{L} + \frac{2.88(\frac{Y_s}{L})^3}{\frac{1}{d} + \frac{(\frac{Y_s}{L})^2}{700}} \tag{3.14}$$

and thus the primary actuation force is:

$$F_y = 48\frac{EI}{L^3}Y_s + \frac{2.88EI}{\frac{L^5}{d} + \frac{L^3Y_s^2}{700}}Y_s^3 \tag{3.15}$$

Using the numerical value of the CBPM component reported in section 3.2, the primary actuation force behaviour versus the displacement is shown in Figure 3.17.

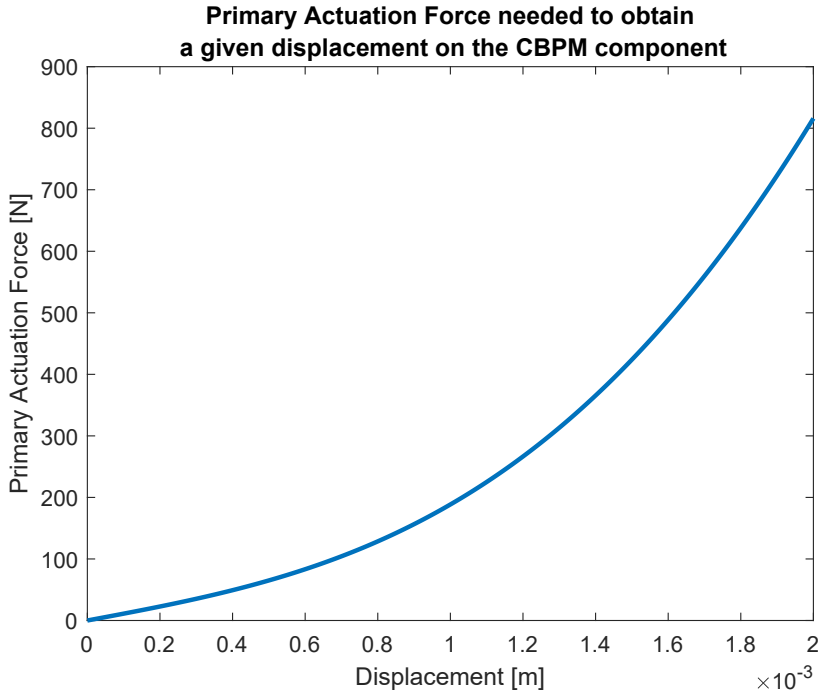

Figure 3.17: CBPM primary actuation force as a function of the displacement

As can be seen from Figure 3.17, the relationship between the primary actuation force and the displacement is strongly non-linear and therefore non-linearity effects cannot be neglected.

Using equation (3.13), the normalized primary motion stiffness can be evaluated [31]:

$$k_y = \frac{df_y}{dy_s} = 48 + \frac{8.64y_s^2}{(\frac{1}{d} + \frac{y_s^2}{700})} - \frac{5.76y_s^4}{700(\frac{1}{d} + \frac{y_s^2}{700})^2} \tag{3.16}$$

Considering the normalization factors, the primary motion stiffness becomes:

$$K_y = \frac{dF_y}{dY_s} = \frac{48EI}{L^3} + \frac{8.64EIY_s^2}{\frac{L^5}{d} + \frac{L^3Y_s^2}{700}} - \frac{5.76EIL^3Y_s^4}{700(\frac{L^5}{d} + \frac{L^3Y_s^2}{700})^2} \tag{3.17}$$

Using the numerical value of the CBPM component reported in section 3.2, the primary motion stiffness behaviour versus the displacement is shown in Figure 3.18.

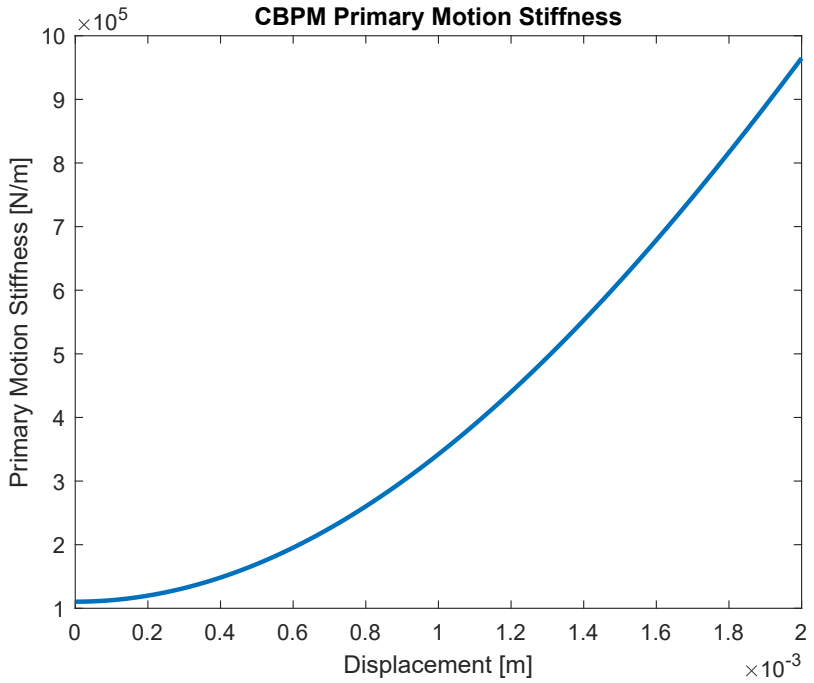

Figure 3.18: CBPM primary motion stiffness as a function of the displacement

To obtain the system model, the theoretical stiffness equation of the XYZ CPM also needs to be evaluated. According to [10], the single beam that composes the XYZ CPM component can be represented as in Figure 3.19.

Under the assumption of small deflection, it is possible to evaluate the beam stiffness using the simplified Euler-Bernoulli equation [10]:

$$\frac{M(x)}{EI} = \frac{d^2y}{dx^2} \tag{3.18}$$

Figure 3.19: Deformed Beam [10]

where:
- $M(x) = F(L-x) - \frac{FL}{2} = \frac{FL}{2} - Fx$,
- E is the Young's module,
and
- I is the second moment of area of a rectangular section ($I = \frac{1}{12}WT^3$).
Substituting the $M(x)$ expression in equation (3.18):

$$\frac{d^2y}{dx^2} = \frac{\frac{FL}{2} - Fx}{EI} \tag{3.19}$$

Therefore:

$$\frac{dy}{dx} = \int (\frac{\frac{FL}{2} - Fx}{EI})dx = \frac{1}{EI}(\frac{FLX}{2} - \frac{FX^2}{2}) \tag{3.20}$$

Consequently:

$$y = \int_0^L \frac{1}{EI}(\frac{FLX}{2} - \frac{FX^2}{2})dx = \frac{FL^3}{12EI} \tag{3.21}$$

Thus, the stiffness of a single beam of the XYZ CPM component is:

$$k_{singlebeamXYZ} = \frac{F}{y} = 12\frac{EI_{XYZ}}{L^3_{XYZ}} = \frac{EU_{XYZ}T^3_{XYZ}}{L^3_{XYZ}} \tag{3.22}$$

Using the numerical value for the XYZ CPM parameters reported in subsection 3.2.2, the single beam stiffness is found to be: $k_{singlebeamXYZ} = 552N/m$. Furthermore, knowing that 24 beams are included in the XYZ CPM axis stiffness, the total linear stiffness of the XYZ CPM compliant component is:

$$k_{XYZ} = 24 \cdot k_{singlebeamXYZ} = 24 \cdot 552 = 13248N/m \tag{3.23}$$

The primary actuation force of one axis of the system is obtained adding the XYZ CPM stiffness to the linear stiffness of the equation (3.15):

$$F_y = (48\frac{EI_{CBPM}}{L^3_{CBPM}} + 24\frac{12EI_{XYZ}}{L^3_{XYZ}})Y_s + \frac{2.88EI_{CBPM}}{\frac{L^5_{CBPM}}{d} + \frac{L^3_{CBPM}Y^2_s}{700}}Y^3_s \quad (3.24)$$

Moreover, adding the XYZ stiffness to equation (3.17), the total axis stiffness can be found:

$$K_y = \frac{48EI_{CBPM}}{L^3_{CBPM}} + 24\frac{12EI_{XYZ}}{L^3_{XYZ}} + \frac{8.64EI_{CBPM}Y^2_s}{\frac{L^5_{CBPM}}{d} + \frac{L^3_{CBPM}Y^2_s}{700}} - \frac{5.76EI_{CBPM}L^3_{CBPM}Y^4_s}{700(\frac{L^5_{CBPM}}{d} + \frac{L^3_{CBPM}Y^2_s}{700})^2} \quad (3.25)$$

The behaviour of the total axis force as a function of the axis displacement is shown in Figure 3.20, together with the primary actuation force of the CBPM and the force of the XYZ CPM separately.

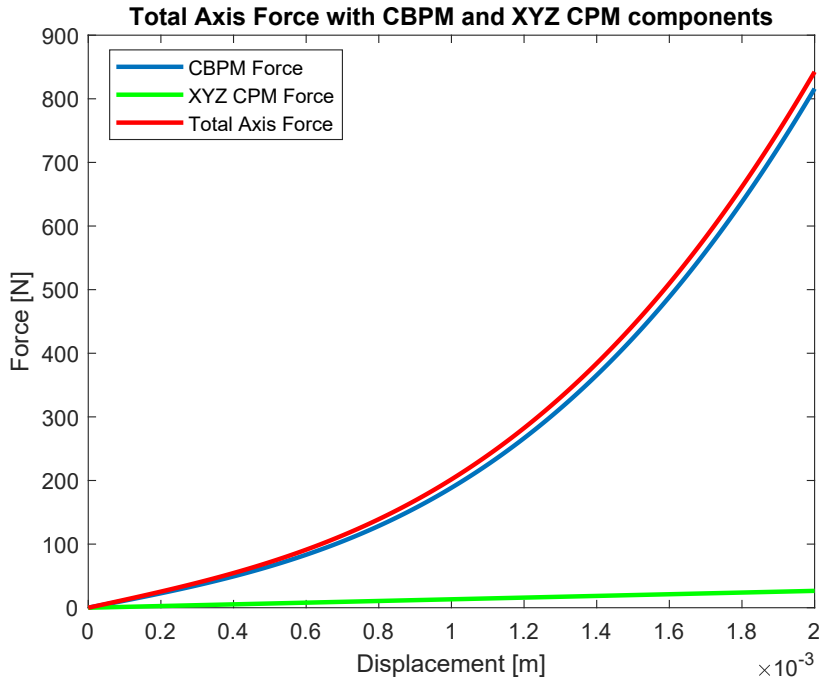

Figure 3.20: Total Axis Force and CBPM and XYZ CPM Components Force

3.9 NON-LINEAR MODEL SIMULINK

In a previous thesis work on this project [8], the behaviour of the system was simulated only in the linear range by modelling the system with the linear transfer-function reported in (3.9). The non-linear behaviour was analyzed only experimentally.
During this thesis work, the non-linear equations were used to imple-

ment also a non-linear model of the system in Simulink.
As wrote above, the non-linear behaviour is mainly due to the non-linear stiffness of the CBPM component of the manipulator. Therefore, the linear force expression reported in equation (3.6) can be modified replacing the linear stiffness k_t, with the non-linear stiffness function $k(x)$:

$$F(t) = m_{tot}\ddot{x}(t) + c\dot{x}(t) + k(x)x(t) \tag{3.26}$$

Expressing this equation in the Laplace domain, we have:

$$F(s) = m_{tot}s^2X(s) + csX(s) + k(x)X(s) \tag{3.27}$$

or:

$$F(s) - k(x)X(s) = m_{tot}s^2X(s) + csX(s) \tag{3.28}$$

Let us define: $F(s) - k(x)X(s) = U(s)$, it can be seen that there is a linear relation between $U(s)$ and the Laplace transform of the system velocity $sX(s)$:

$$\frac{sX(s)}{U(s)} = \frac{1}{m_{tot}s + c} \tag{3.29}$$

This equation can be represented using the block diagram reported in Figure 3.21.

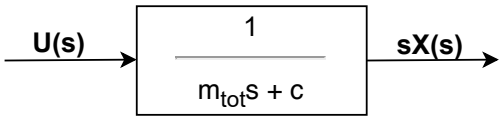

Figure 3.21: Linear Transfer-Function that links U(s) and sX(s)

Integrating the velocity $sX(s)$, that is multiplying by $\frac{1}{s}$ in the Laplace domain, we obtain the position signal $X(s)$.
Remembering the non-linear relation (3.24) between actuating force and position, it is possible to obtain $U(s)$ by calculating the term $k(x)X(s)$ and subtracting it from the actuating force $F(s)$.
Hence, the schematic representation of the non-linear system that represent the relationship between the actuating force and the system position is shown in Figure 3.22.

This model was implemented in Simulink and placed instead of the real system to simulate the system behaviour in the non-linear range. The Simulink non-linear model is shown in Figure 3.23 and the $k(x)$ Matlab Function is reported in appendix A.1.

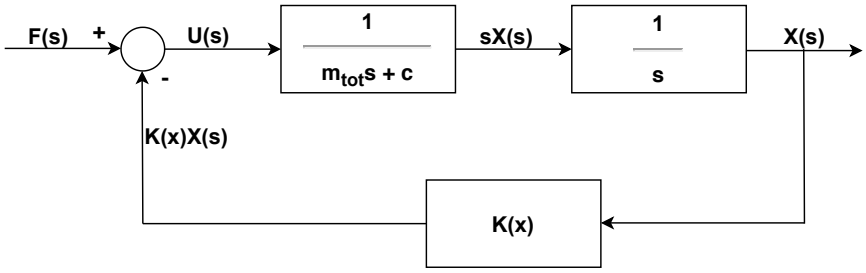

Figure 3.22: Non-Linear Model Schematic Representation

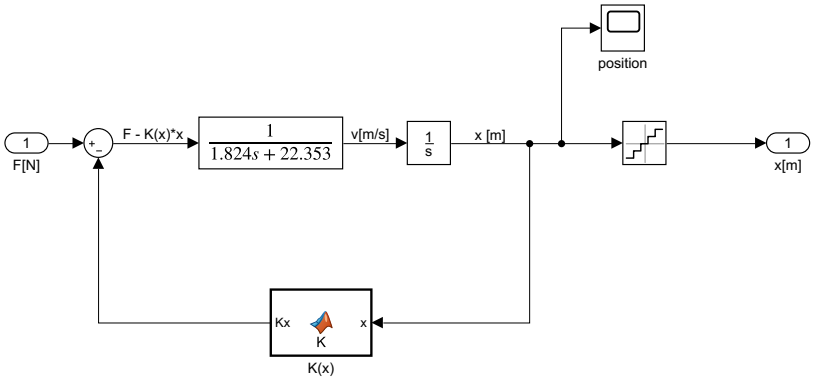

Figure 3.23: Non-Linear Model Simulink of the Relationship between the Actuating Force and the System Position

4

BACKGROUND: ONE AXIS SYSTEM (X-AXIS)

4.1 INTRODUCTION

The project of the compliant high performance positioning system is quite complex and a number of students worked on its design and control, as written in the introduction (Chapter 1).
All the prior activities were concerned only the movement of one of the two system axes (the X-axis). In this chapter, the one axis control algorithm (described in [8]) is summarized. It was implemented by the last student that worked on the manipulator, improving the work of previous students. This was the starting point for the control algorithm implemented in this thesis work.
The control structure implemented in Simulink is shown in Figure 4.1, in which different subsystems are reported. The first one is the Input subsystem, shown in Figure 4.2. This block imports the position, velocity and acceleration reference signals from the Matlab workspace and, applying appropriate gains, it scales the reference signals to obtain the desired amplitude of physical movement. In [8] the motion trajectory was chosen in order to use a reference signal that the manipulator can follow. This will be described in Section 4.2.

The Scope subsystem of the Simulink Control Scheme of Figure 4.1 is reported in Figure 4.3. This subsystem allows the visualization of both the reference and the measured signals on the same plot.

In the Real System subsystem, the physical connections to the dSPACE controller board are implemented. This Simulink subsystem was described in the dSPACE controller board section (Section 3.7). The real system block can be replaced with a system model in order to simulate the system behaviour. The system model can be the linear transfer-function reported in Section 3.8.1 or the non-linear Simulink model reported in Section 3.9.
All the remaining subsystems require a more detailed description and therefore they will be explained in the next sections. The PID controller and the Newton subsystem constitute the feedback control. They are described in Section 4.3. The feed-forward controller is described in Sections 4.4. Finally, a velocity observer was implemented to obtain a velocity less noisy feedback signal than the velocity signal obtained as a derivative of the position feedback returned by the encoder. This subsystem will be described in Section 4.5.

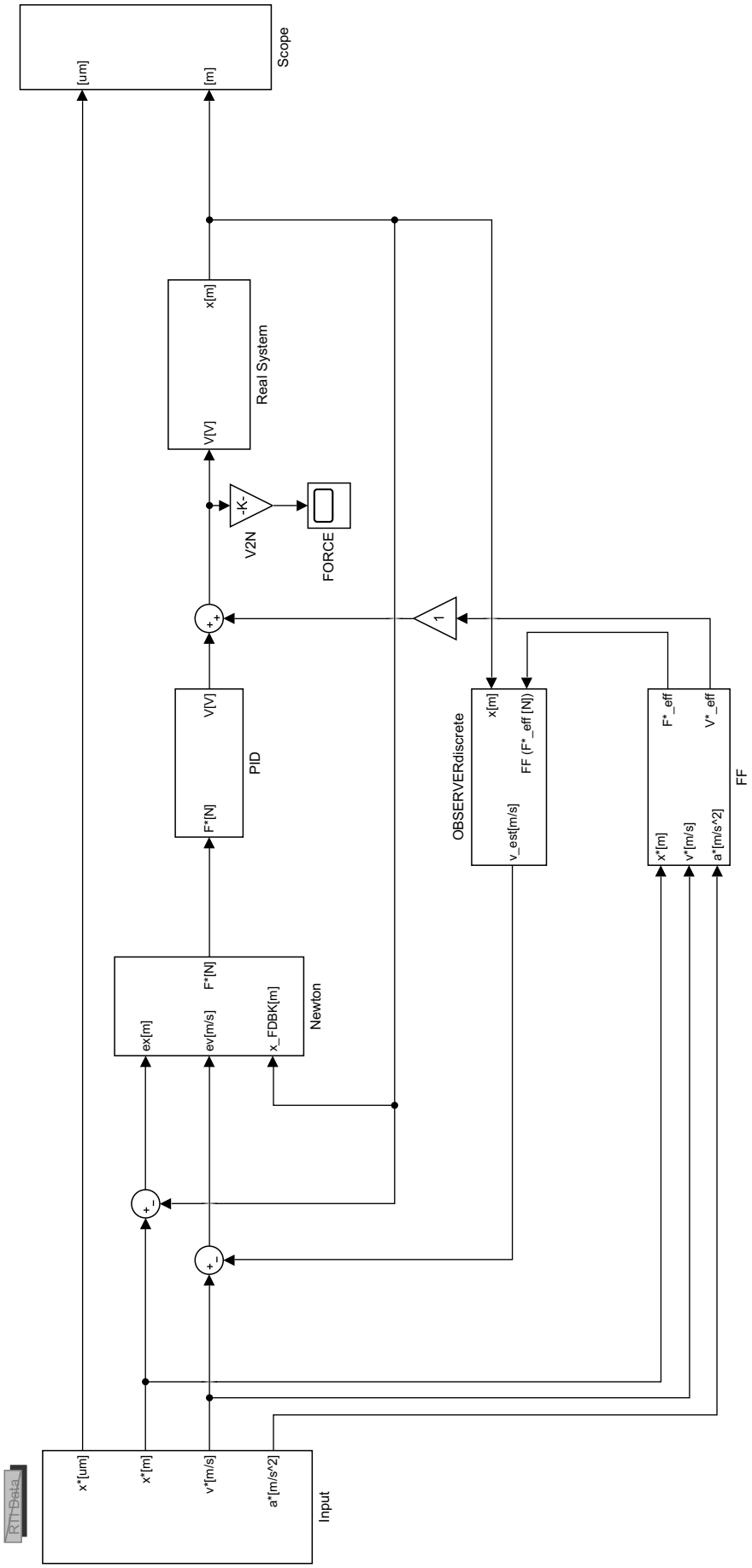

Figure 4.1: One Axis Control Scheme in Simulink [8]

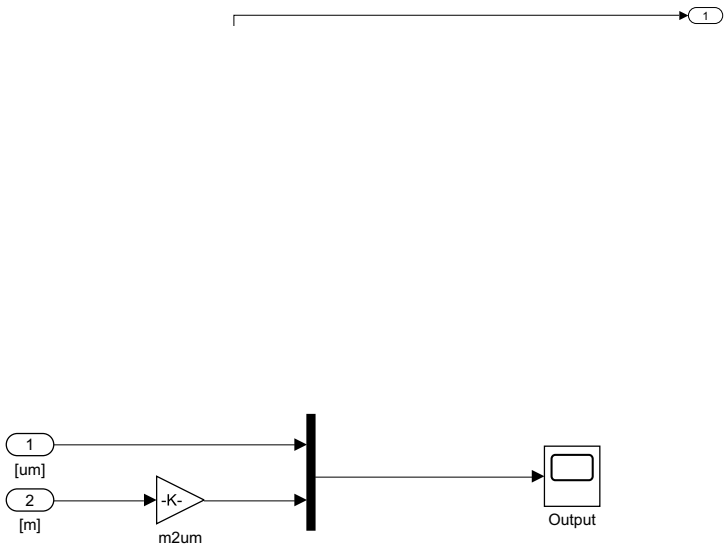

Figure 4.3: Scope Subsystem of One Axis Control Scheme in Simulink [8]

4.2 REFERENCE

In a motion control system achieving precise motion with a minimum vibration and overshoot is extremely important. To fulfill this aim different trajectory planning has been researched, with the target of finding a position reference that provides a mechanically feasible and smooth path while optimizing time and minimizing overshoots of the movement [8]. The ideal step positioning is not feasible because it requires infinite velocity (and of course higher order derivatives are infinite as well), that is impossible to perform in a real system.
For this reason, in [8], the chosen position reference signal for the one-axis system is the one shown in Figure 4.4. Before this signal transition the reference is fixed at 0 while it is held constant at 1 when the transition is over.

The Matlab code that generates this reference signal is reported in Appendix A.2.

The reference signal transition is composed by a half period of a sinewave, shifted and normalized to obtain values in the interval $(0, 1)$. It is defined by the following equation [8]:

$$c\frac{1-\cos(2\pi ft)}{2} \tag{4.1}$$

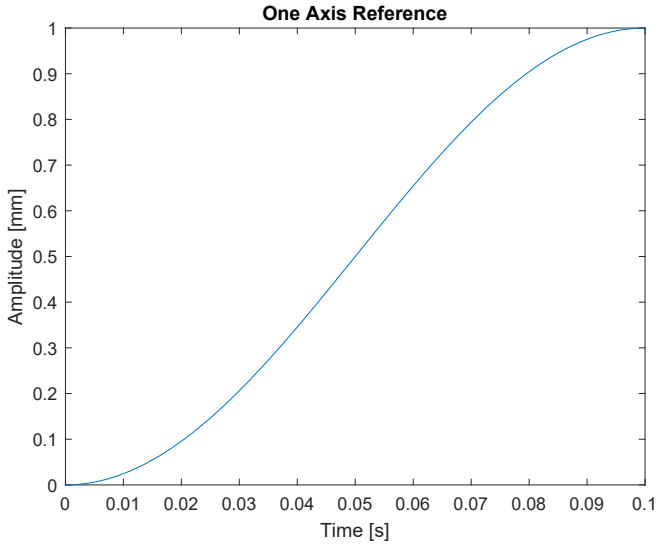

Figure 4.4: Position Reference used in [8]

defining:

$$c = \frac{2s_{des}}{1 - \cos(2\pi f t_{des})}$$
$$\text{and} \tag{4.2}$$
$$f = \frac{1}{2t_{des}}$$

where s_{des} is the desired amplitude and t_{des} is the desired rise time. This reference signal is a good choice because it has a null derivative at both beginning and end and thus it provides a velocity continuous signal.
In [8] the system behaviour with different rise times t_{des} was analyzed and it was concluded that the best choice is $t_{des} = 0.1$, as it is a good trade off between limited overshoot of the system output and fast system response time.
The velocity and the acceleration reference signals are calculated through one or two discrete derivatives of the position reference signal, respectively. This was implemented in Simulink, as shown in Figure 4.5.

The two step Simulink blocks are used to ensure zero velocity and zero acceleration values at the last sample [8]. This program to evaluate the derivatives references signals can be used for any chosen position reference signal.

4.3 FEEDBACK CONTROLLER

The feedback controller is composed of two Simulink subsystems: the Newton subsystem (described in subsection 4.3.1) and the PID subsystem (described in subsection 4.3.2).

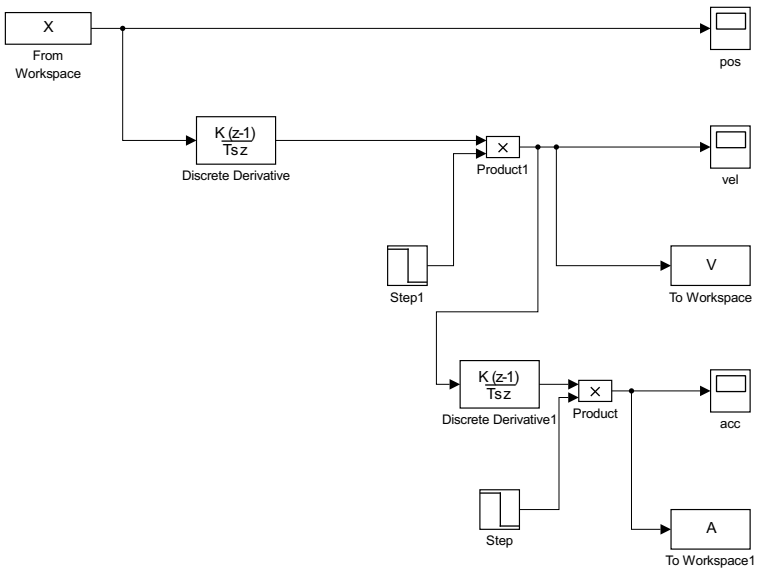

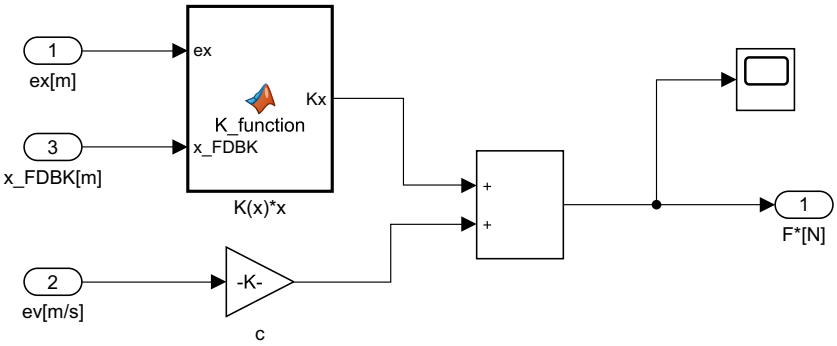

Figure 4.6: Newton Subsystem of One Axis Control Scheme in Simulink [8]

The K_function block is a Matlab function used to evaluate the non-linear stiffness of the manipulator. This function has two inputs: the position measurement returned by the encoder and the position error signal. The first input is needed to calculate the non-linear stiffness using equation (3.25), while the second one is needed to evaluate the force. The theoretical non-linear stiffness equation was experimentally corrected using an error term to compensate for the difference between the theoretical expression (3.25) and the real system. This error term was experimentally tuned. Unfortunately, during this the-

sis work it was discovered that, to achieve the best performance, this error parameter needs to be tuned again every time the system was fixed (also if a screw was turned).
The K_function Matlab code is reported in Appendix A.3.
Considering that the velocity has a linear behaviour in the force expression, a simple gain (equal to the viscous damping coefficient c) was used to consider the velocity error effect. However, this term could be useless because of the presence of the derivative term in the PID action. This consideration is supported by the PID tuning results reported in the next section, where the derivative gain is small.

4.3.2 *PID controller*

The PID control subsystem is shown in Figure 4.7. During this thesis work the PID control gains was retuned because the servo amplifier was replaced and therefore its gain is different. The gain tuning was performed using the Ziegler-Nichols method, explained in Section 2.2. The resulting ultimate gain K_u is equal to 0.53376 and the oscillation period T_u was measured to be equal to 0.022 s. Therefore, using the "PID no overshoot" gains formulas shown in Table 2.1, the resultant PID gains are:

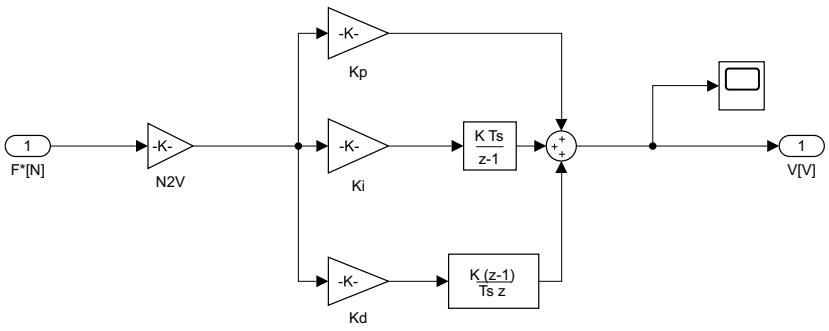

Figure 4.7: PID Subsystem of One Axis Control Scheme in Simulink [8]

4.4 FEED-FORWARD CONTROLLER

The feed-forward control implemented in the high-precision positioning system is based on the theoretical value of the force required to perform a specific movement. The related Simulink subsystem is shown in Figure 4.8.

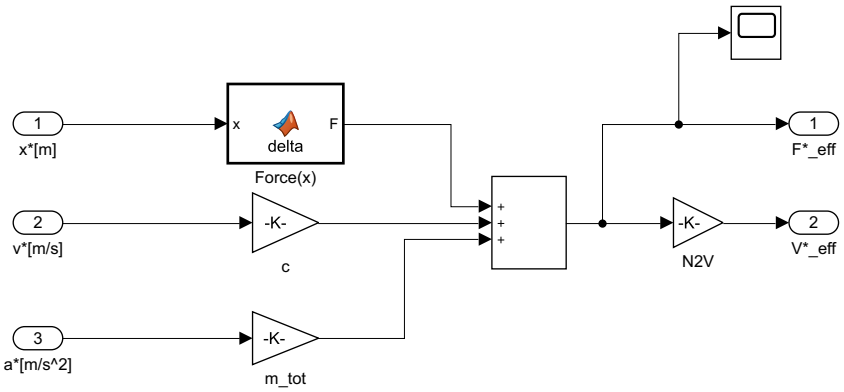

Figure 4.8: Feed-Forward Subsystem of One Axis Control Scheme in Simulink [8]

As it can be noticed from Figure 4.8, the required force is evaluated based on the position, velocity and acceleration reference signals. Both velocity and acceleration have a linear relationship with the actuating force. Therefore their contributions are simply scaled using an suitable gain (equal to the viscous damping coefficient c and the total mass m_{tot} for the velocity and acceleration, respectively), and added up. Conversely, the stiffness is not linear and therefore the relation between the position reference signal and the force is calculated by a Matlab function implementing the force equation (3.24). The related Matlab code is reported in Appendix A.4.
As occurred in the non-linear stiffness function (in the Newton subsystem 4.3.1), some error terms, tuned experimentally, were added to this Matlab function to compensate for the difference between the theoretical expression and the real behaviour of the system. Also in this case, this error coefficients need to be tuned experimentally every time the system was set up.

4.5 VELOCITY OBSERVER

The velocity observer subsystem estimates the velocity used in the feedback control. The Simulink block is shown in Figure 4.9 and it was implemented using the information reported in the observer theory explained in Section 2.3.

In [8], the observer gain values were chosen by considering the three possible options reported in Table 2.2. It was verified that the medium configuration provided the best compromise between noise filtering and disturbance rejection. Therefore, the gains used in the Simulink Observer subsystem are:

- $L_1 = 0.2473$
- $L_2 = 0.1716$

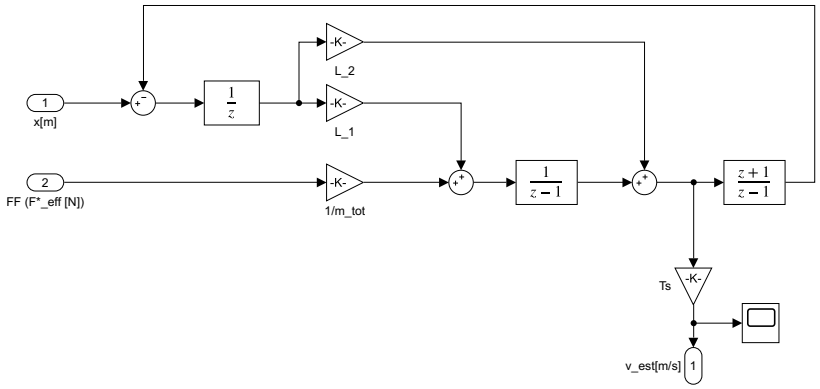

Figure 4.9: Observer Subsystem of One Axis Control Scheme in Simulink [8]

During this thesis work, the three possible gain pairs were tested and the previous selection was confirmed to be the best choice.

4.6 X-AXIS RESULTS

Some meaningfull measurements were performed using the control algorithm presented in this chapter. The simulation and experimental results achieved for $\pm 0.1 mm$ (linear range) and $\pm 1 mm$ (non-linear range) position reference on the X-axis are shown in this section.

4.6.1 *Simulations*

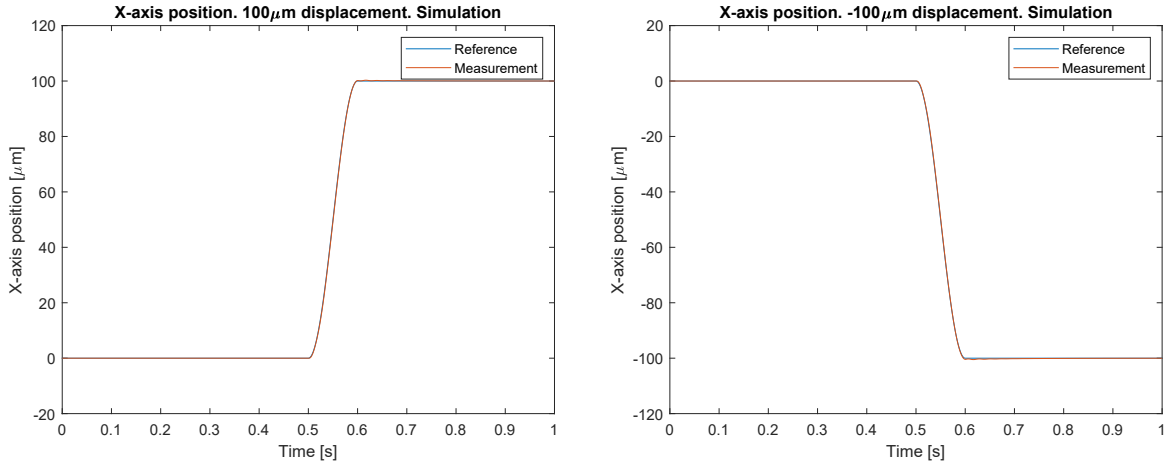

Figure 4.10: X-axis position, ± 100 µm displacement. Reference signals and simulation results

The maximum absolute and RMS (Root Mean Square) values of the error between the measurement results and the reference signal are reported in Table 4.1 for the different amplitudes chosen.

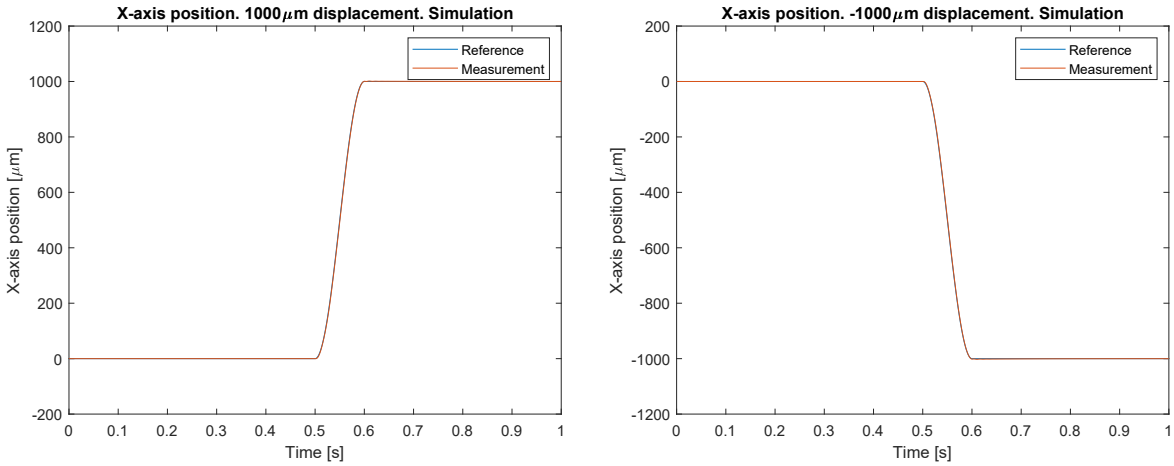

Figure 4.11: X-axis position, ±1000 µm displacement. Reference signals and simulation results

Axis	X	X	X	X
Displacement Amplitude [µm]	100	1000	-100	-1000
Maximum Absolute Error Value [µm]	0.671	7.059	0.561	5.995
RMS Error Value [µm]	0.05	0.48	0.05	0.43

Table 4.1: Maximum absolute error and RMS error Values for the different displacements chosen. X-axis. Simulation results

The data show that the maximum error is in the micro-meters range, while the RMS error values are always smaller than 1µm in the simulation analysis.

4.6.2 *Experiments*

The maximum absolute and RMS (Root Mean Square) values of the error between the measurement results and the reference signal are reported in Table 4.2 for the different amplitudes chosen.

Axis	X	X	X	X
Displacement Amplitude [µm]	100	1000	-100	-1000
Maximum Absolute Error Value [µm]	0.762	12.27	1.434	9.860
RMS Error Value [µm]	0.16	5.91	0.32	1.82

Table 4.2: Maximum absolute error and RMS error values for the different displacements chosen. X-axis. Experimental Results

The data show that the maximum error is in the micro-meter range and, as expected, they are slightly larger than that obtained in the simulation. Furthermore, the RMS error values, as expected, are bigger than those obtain in simulation. This is probably due to the external noise that is always present in the real system.

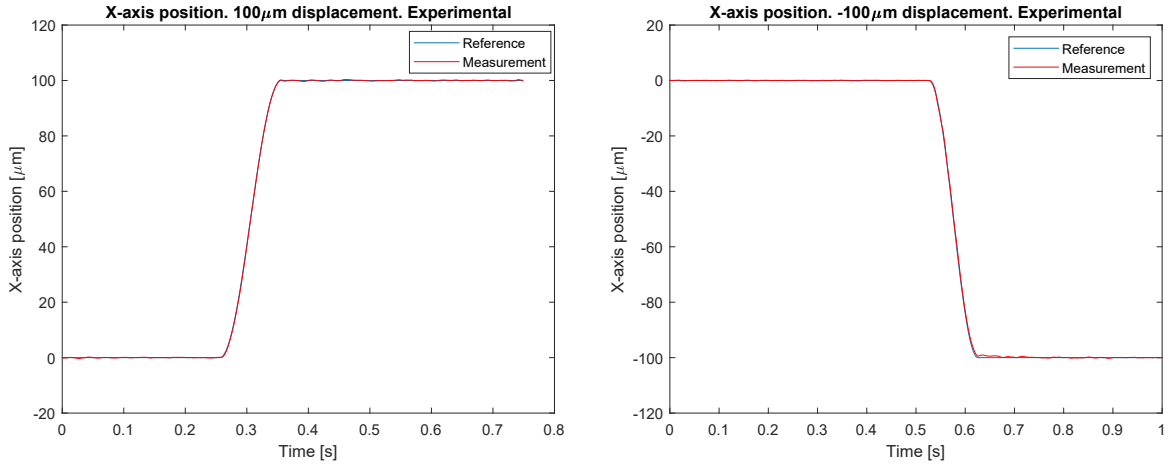

Figure 4.12: X-axis position, ±100 µm displacement. Reference signal and experimental results

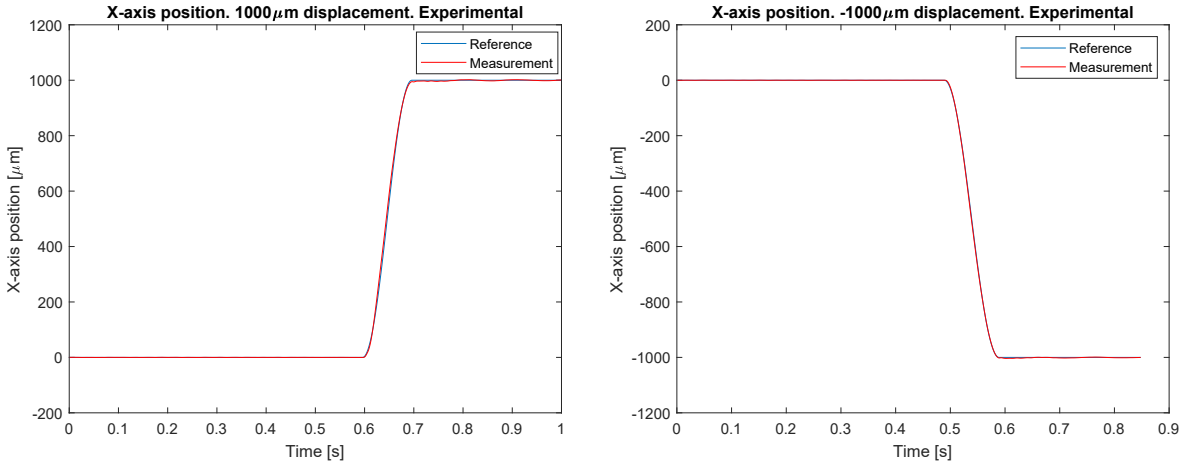

Figure 4.13: X-axis position, ±1000 µm displacement. Reference signal and experimental results

5 TWO AXES SYSTEM

5.1 INTRODUCTION

During this thesis work, the high-precision compliant positioning system was extended from one to two axes. The XYZ CPM was designed in [5] to allow motion performance along the three motion directions to be isotropic. Due to this structure, which decouples the three-axes movements, the control algorithm of each axis can be implemented separately, with each using the same structure. Therefore, to perform movements in two of the three possible degrees of freedom of the XYZ CPM, the physical components of the first axis (amplifier, actuator, CBPM mechanical mechanism, encoder,etc.) were replicated on the second axis.
Specifically, the control algorithm implemented in [8] for the X-axis was replicated for the Y-axis. The only difference between the two algorithms regards the proportional gain of the amplifier, which was measured and discussed in Chapter 3.
The tuning of the Y-axis control system, which has been implemented identically to that of the X-axis one described in the Chapter 4, is illustrated in Section 5.2, where the experimental results obtained using the reference signal designed for the X-axis are also shown. Conversely, simulation results are not reported because, as the amplifier gain is the only difference between the X-axis and the Y-axis, the simulation results are extremely similar to those obtained for the X-axis, which are reported in Chapter 4.
In order to draw some significant shapes on the XY-plane, meaningful reference signals should be selected. The first target shape was a circle on the XY-plane, which was obtaining by feeding both axes with sinusoidal reference signals that have equal amplitude and 90° phase-shift. The choice of this shape was suggested by both its relevance in industrial application and the mathematical simplicity of the reference signals, which have continuous derivatives of all orders. This reference signal and the simulation and experimental results are reported in Section 5.3.
The subsequent target shape was a square in the XY-plane. Drawing this shape is more difficult than the circumference because of the edges. The choice of this reference signal was made because this shape increases the industrial applications of the manipulator. A possible reference signal for both axes to draw a square on the XY-plane is a square wave. However, this option has been discarded because the signal discontinuities cannot be followed accurately by the sys-

tem. Another reference signal that can be used to produce a square in the XY-plane is the triangular signal. In this case, the square shape is rotated of 45 degrees with respect to the shape obtained with a square reference signal. The triangular wave reference signal with simulation and experimental results will be illustrated in Section 5.4. Unfortunately, triangular signal has a discontinuous derivative (the velocity waveform is a square wave); therefore it would require an infinite system acceleration to be followed accurately. To overcome this problem, another reference signal was designed in order to draw a square on the XY-plane. This reference signal is a smooth trapezoidal signal and it will be described in Section 5.5.

5.2 Y-AXIS CONTROL

The Y-axis control algorithm was implemented to be identical to the X-axis one, illustrated in chapter 4. The only difference was the amplifier gain and therefore the PID gains. The PID was tuned using the Ziegler-Nichols method, explained in Section 2.2. For the Y-axis, the ultimate gain K_u and the oscillation period T_u resulted in parameters that are equal to 0.53372 and to 0.015 s, respectively. Therefore, using the "PID no overshoot" gain formulas showed in Table 2.1, the following PID gains resulted:

- $K_p = 0.2K_u = 0.10674$
- $T_i = \frac{T_u}{2} = 0.0075s \rightarrow K_i = \frac{K_p}{T_i} = 14.233$
- $T_d = \frac{T_u}{3} = 0.005s \rightarrow K_d = K_p T_d = 0.000534$

As for the X-axis, also the error terms in the Y-axis Matlab functions, related to the feed-forward force and non-linear stiffness, were tuned experimentally.

5.2.1 *Experimental Results*

Some experimental results about the Y-axis performance are shown in this subsection. Figure 5.1 shows the Y-axis capability to follow a ± 100 µm (linear range) smooth step reference with a rise time of 0.1s, while in Figure 5.2 the behaviour related to a ± 1000 µm (non-linear range) smooth step reference with the same time rise is shown.

The maximum absolute and RMS (Root Mean Square) values of the error between the measurement results and the reference signal is reported in Table 5.1 for the different amplitudes chosen. Data show that both the maximum error and the RMS error are in the micrometer range and they assume values close to those obtained for the experimental analysis of the X-axis (reported in section 4.6).

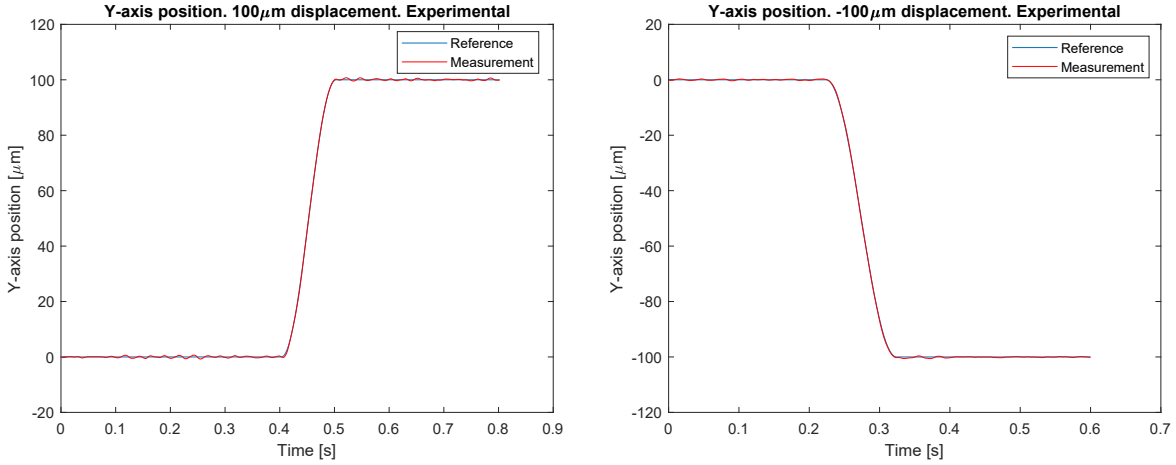

Figure 5.1: Y-axis position, ±100 µm displacement. Reference signals and experimental results

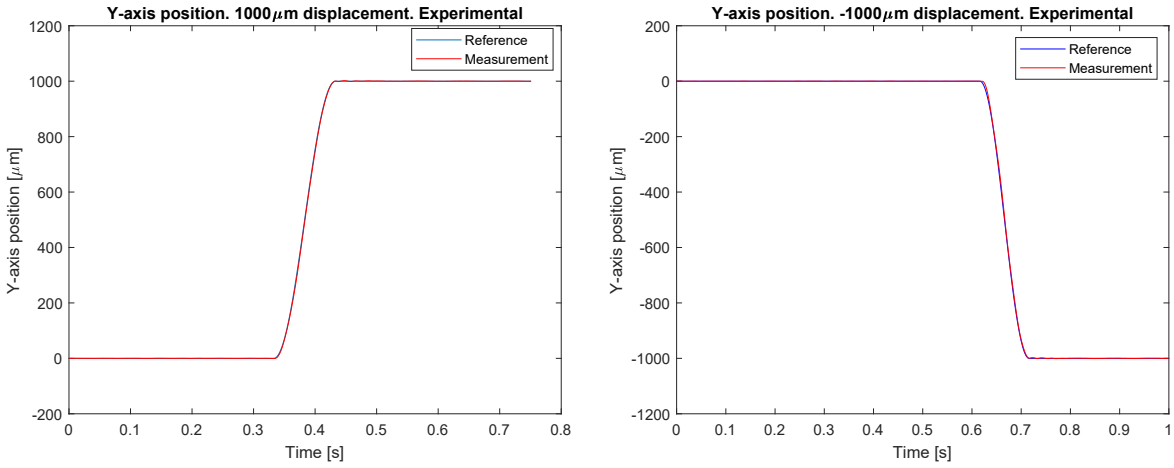

Figure 5.2: Y-axis position, ±1000 µm displacement. Reference signals and experimental results

Axis	Y	Y	Y	Y
Displacement Amplitude [µm]	100	1000	-100	-1000
Maximum Absolute Error Value [µm]	0.84	11.8	0.68	17.9
RMS Error Value [µm]	0.28	2.66	0.23	3.33

Table 5.1: Maximum absolute error and RMS error values for the different displacements chosen on the Y-axis. Experimental results.

5.3 SINUSOIDAL WAVE REFERENCE SIGNAL

The first shape performed in the XY-plane, moving both axes simultaneously, was a circular trajectory. To achieve this target, two sinusoidal reference signals of equal amplitude and with a 90° phase-shift each other were applied on the axes concurrently. The Matlab script that generate these reference signals is reported in Appendix A.5, while the time domain signals and the related XY-plane plot are shown in Figure 5.3.

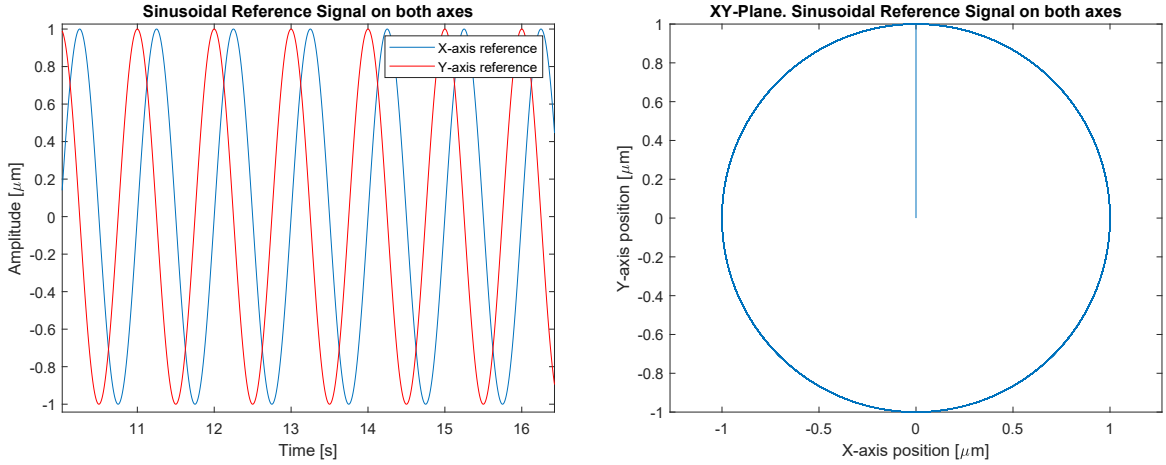

Figure 5.3: Sinusoidal wave reference signals on both axes

Simulations and experiments were performed considering these reference signals with different amplitude and frequency. The results achieved with amplitude 100 µm (linear range) and 500 µm (non-linear range), and frequency 1 Hz and 10 Hz are reported in this section. The simulation results can be found in Subsection 5.3.1, while the experimental results are shown in Subsection 5.3.2.
Different shapes on the XY-plane obtained with the sinusoidal reference signal with different amplitude and phase-shift between the two axes are reported in Subsection 5.3.3.

5.3.1 *Simulation Results*

The simulation results achieved in the XY-plane with the 100 µm amplitude sinusoidal reference signal at 1 Hz and 10 Hz frequency on both axes are shown in Figure 5.4, while the results achieved when the amplitude is 500 µm are shown in Figure 5.5.

The maximum absolute and the RMS values of the position error are reported in Table 5.2 for the different amplitudes and frequencies considered.

As it can be noticed both from the plots and the RMS error values, the difference between the output and the reference signals increases with frequency. This is clearly due to the system inertial behavior,

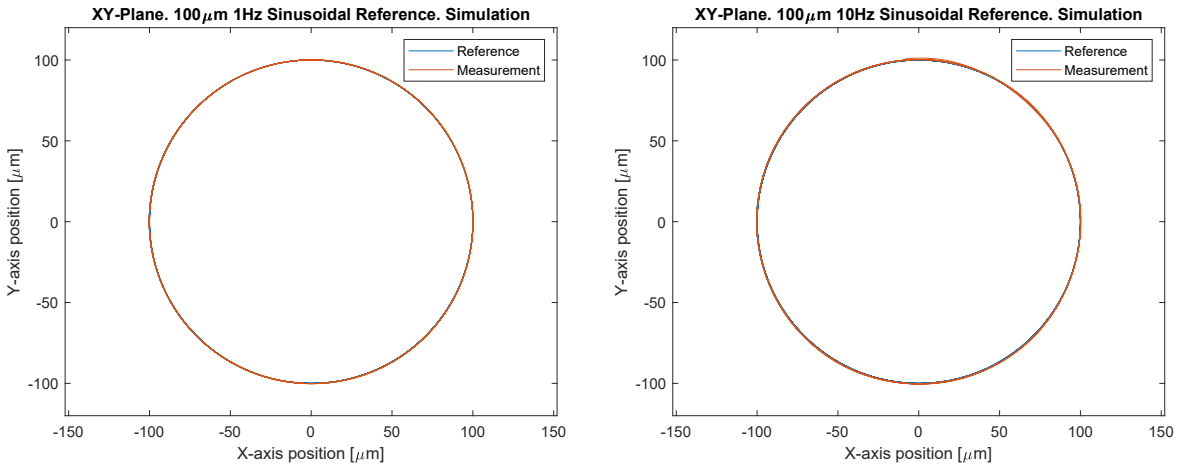

Figure 5.4: Sinusoidal wave reference signals 100 µm on both axes. XY-plane. Reference signals and simulation results

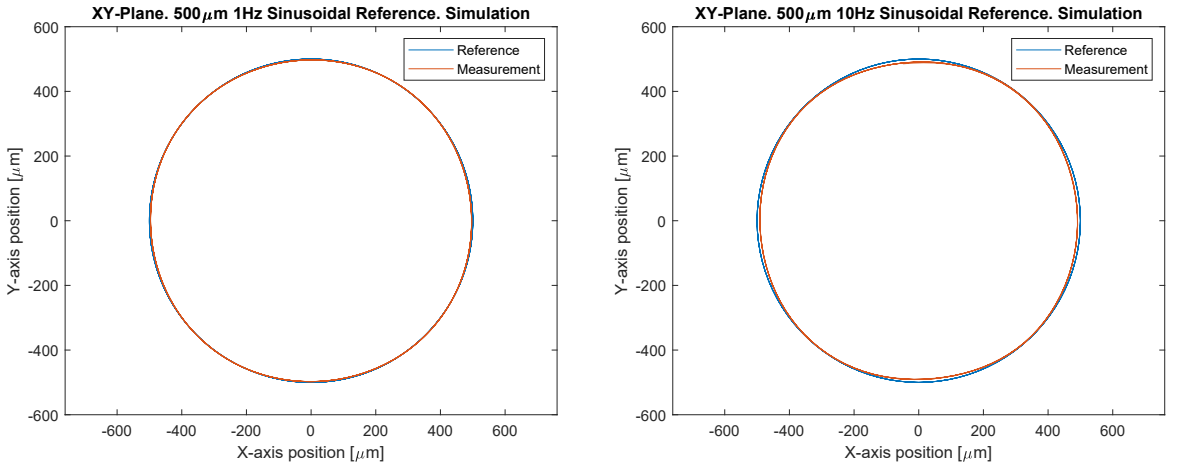

Figure 5.5: Sinusoidal wave reference signals 500 µm on both axes. XY-plane. Reference signals and simulation results

Axis	X	Y	X	Y	X	Y	X	Y
Amplitude [µm]	100	100	100	100	500	500	500	500
Frequency [Hz]	1	1	10	10	1	1	10	10
Maximum Absolute Error Value [µm]	0.90	0.91	2.94	3.49	5.49	5.07	17.4	18.2
RMS Error Value [µm]	0.14	0.12	1.96	1.93	3.61	3.17	11.4	11.4

Table 5.2: Maximum absolute error and RMS error values obtained with sinusoidal reference signal. Simulation results

because when the frequency is increased, the system is required to move faster and therefore it is more difficult to follow correctly the reference.
However, the simulation results show a good overall system performance on the whole over the range of amplitude and frequency values chosen.

5.3.2 *Experimental Results*

The experimental results achieved in the XY-plane with the sinusoidal reference signal of 100 µm amplitude at 1 Hz and 10 Hz frequency on both axes are shown in Figure 5.6, while the results achieved when the amplitude is 500 µm are shown in Figure 5.7.

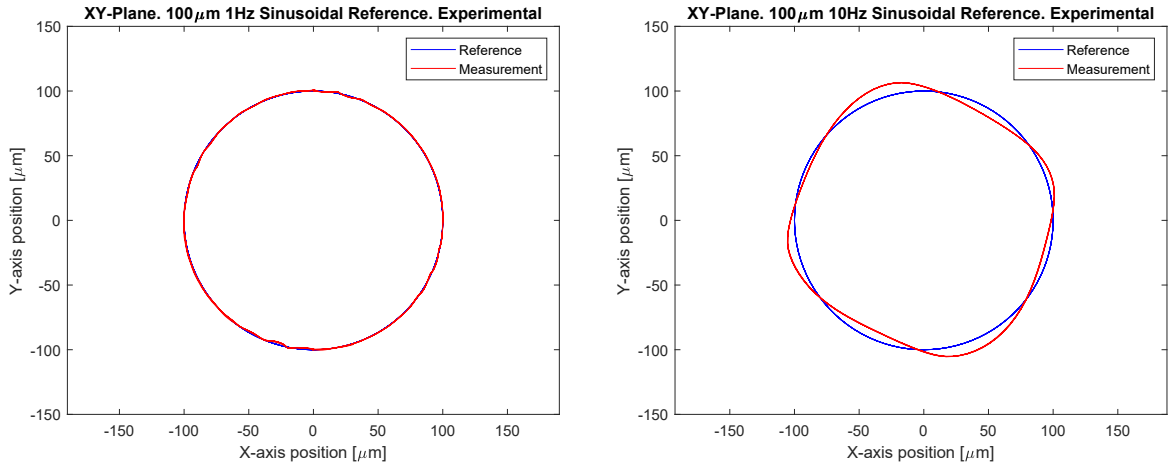

Figure 5.6: Sinusoidal wave reference signals 100 µm on both axes. XY-plane. Reference signals and experimental results

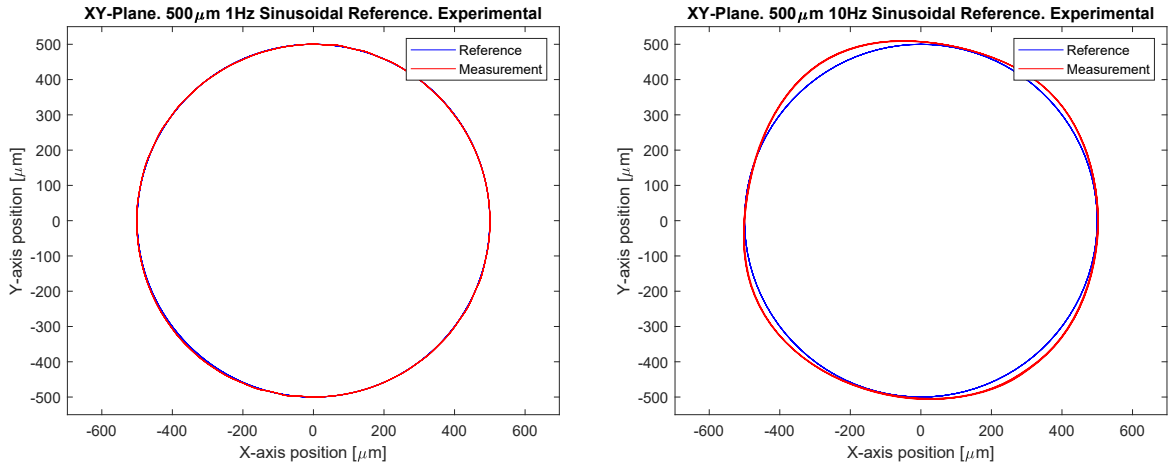

Figure 5.7: Sinusoidal wave reference signals 500 µm on both axes. XY-plane. Reference signals and experimental results

The maximum absolute and the RMS values of the position error are reported in Table 5.3 for the different amplitudes and frequencies considered.

Axis	X	Y	X	Y	X	Y	X	Y
Amplitude [µm]	100	100	100	100	500	500	500	500
Frequency [Hz]	1	1	10	10	1	1	10	10
Maximum Absolute Error Value [µm]	10.6	9.57	13.5	15.9	13.0	9.44	30.3	33.8
RMS error value [µm]	1.84	1.57	5.41	7.71	2.51	1.74	16.7	19.8

Table 5.3: Maximum absolute error and RMS error values obtained with sinusoidal reference signal. Experimental results

Comparing these results with the simulation ones, in the experimental data the performance difference between the analyses at 1 Hz and 10 Hz is most relevant informative. As expected, in most cases both the maximum absolute error and the RMS error values are bigger than the corresponding values returned by simulations.

5.3.3 *Different Shapes using Sinusoidal Reference Signal*

Changing the amplitude and/or the phase-shift of the two sinusoidal reference signals, different shapes can be plotted on the XY-plane. Modifying the amplitude of one of the two signals and maintaining the 90° phase-shift between them, it is possible to obtain an ellipse. Moreover, if the phase-shift is modified, the ratio between the ellipse axes change and they also rotate on the XY-plane. With a 0° phase-shift, a diagonal line on the XY-plane is plotted.
In Figure 5.8, two examples of different shapes obtained experimentally with sinusoidal reference signals at 1 Hz are shown.

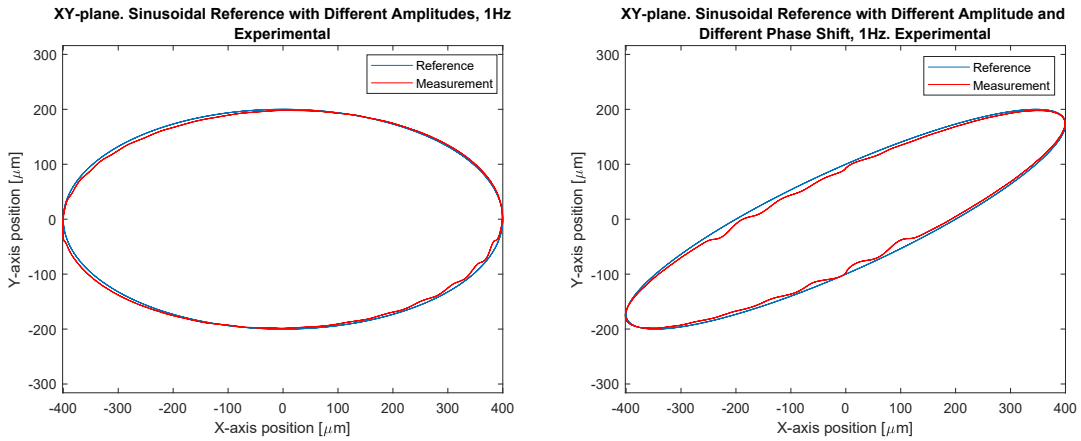

Figure 5.8: Examples of XY-plane results with modified sinusoidal reference signal. Reference signals and experimental results

5.4 TRIANGULAR WAVE REFERENCE SIGNAL

A couple of triangular waveforms with 90° phase-shift were first considered as reference signals to performed a square in the XY-plane. The square is rotated of 45° with respect to the X and Y axes. The Matlab script that generate these reference signals is reported in Appendix A.6, while the time-domain signals and the related XY-plane plot are shown in Figure 5.9.

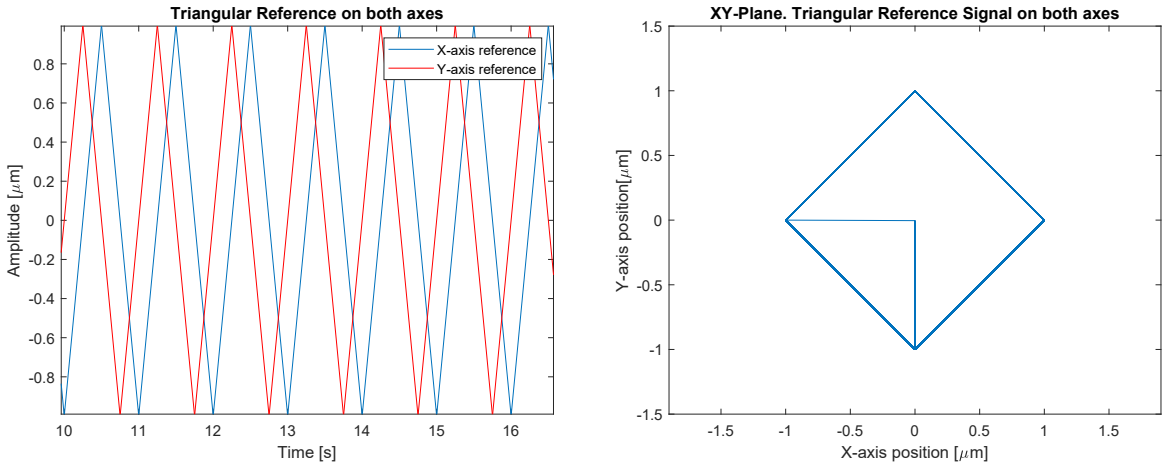

Figure 5.9: Triangular wave reference signals on both axes

As for the sinusoidal reference signal, simulations and experiments were performed considering triangular reference signals of different amplitudes and frequencies. The results achieved with amplitude 100 µm (linear range) and 500 µm (non-linear range) and frequency at 1Hz and 10Hz are reported in this section. The simulation results can be found in Subsection 5.4.1, while the experimental results are shown in Subsection 5.4.2.

5.4.1 *Simulation Results*

The simulation results achieved in the XY-plane with the 100 µm triangular reference signal at 1 Hz and 10 Hz frequency on both axes are shown in Figure 5.10, while the results obtained when the amplitude is 500µm are shown in Figure 5.11.

The maximum absolute and the RMS values of the position error are reported in Table 5.4 for the different amplitudes and frequencies considered for the triangular reference signals.

As it can be noticed from both the plots and the error data, when the amplitude or the frequency increases, it is more difficult to follow accurately the reference signal and therefore the position error increases (in terms of both maximum and RMS values).
Due to the nature of the triangular signal, that is less smooth than

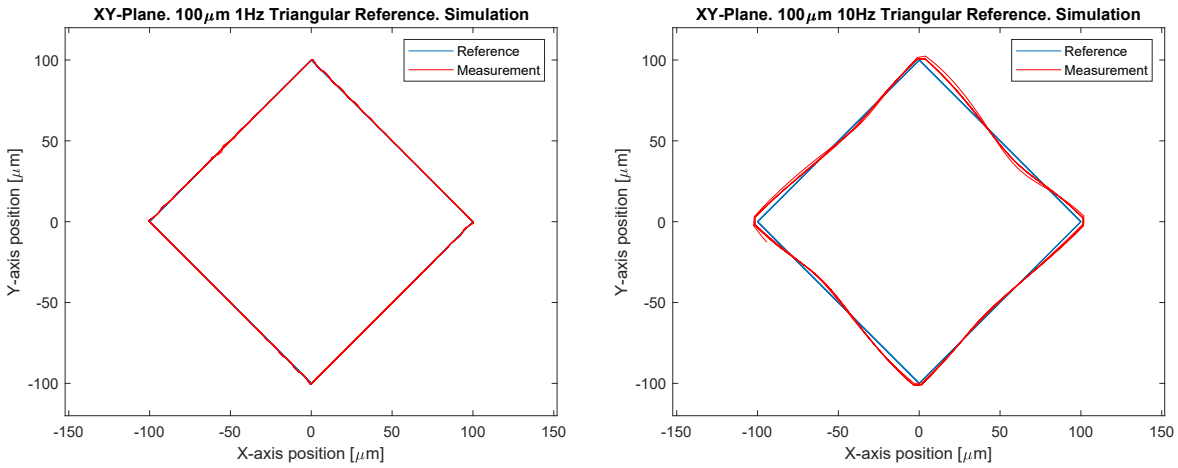

Figure 5.10: Triangular wave reference signals 100 µm on both axes. XY-plane. Reference signals and simulation results

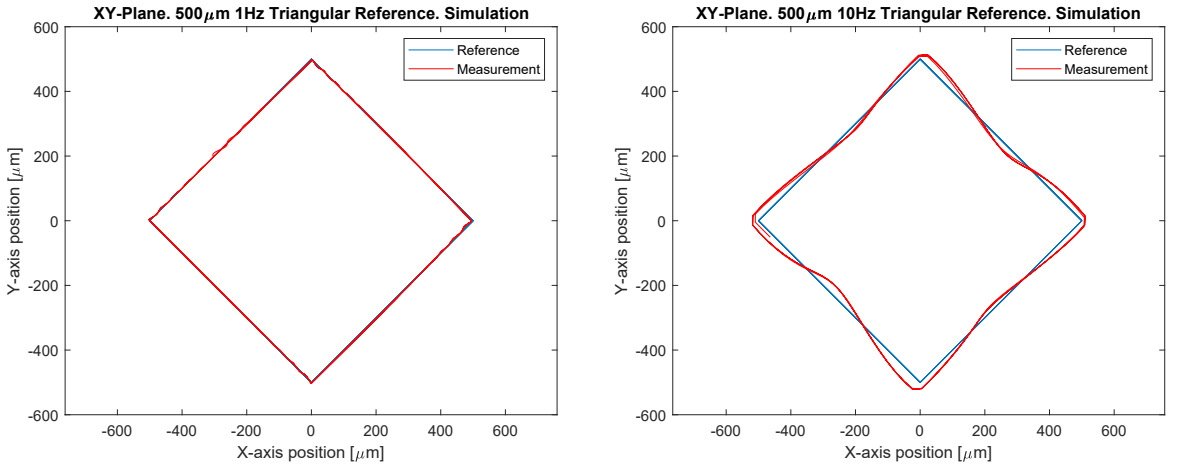

Figure 5.11: Triangular wave reference signals 500 µm on both axes. XY-plane. Reference signals and simulation results

Axis	X	Y	X	Y	X	Y	X	Y
Amplitude [µm]	100	100	100	100	500	500	500	500
Frequency [Hz]	1	1	10	10	1	1	10	10
Maximum Absolute Error Value [µm]	1.23	1.22	9.75	9.07	7.19	5.72	57.3	60.9
RMS error value [µm]	0.66	0.73	3.76	3.89	3.84	3.79	23.1	26.8

Table 5.4: Maximum absolute error and RMS error values obtained with triangular reference signal. Simulation results

the sinusoidal signal, the displacement error is larger than in the sinusoidal case.

5.4.2 *Experimental Results*

The experimental results achieved in the XY-plane with the 100 µm triangular reference signal at 1 Hz and 10 Hz frequency on both axes are shown in Figure 5.12, while the results obtained when the amplitude is 500µm are shown in Figure 5.13.

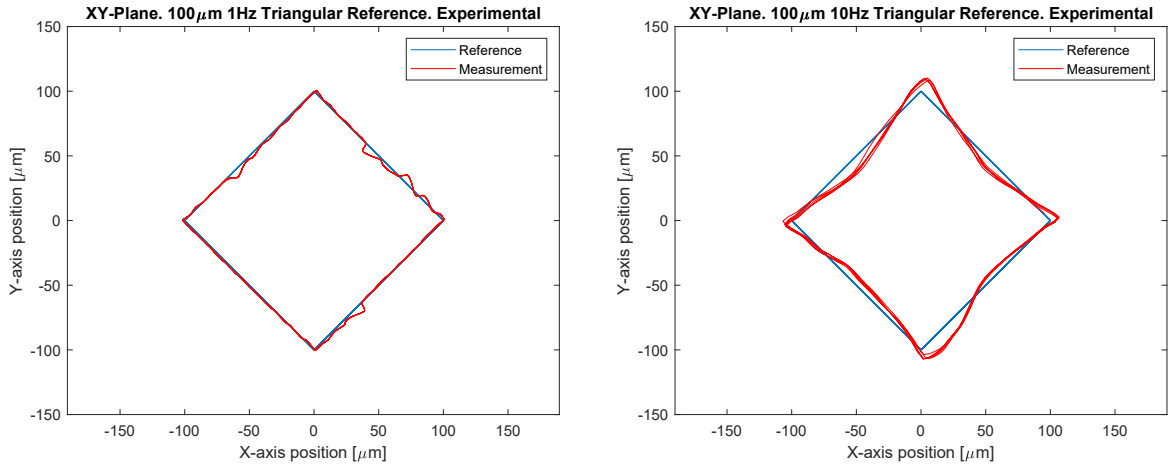

Figure 5.12: Triangular wave reference signals 100 µm on both axes. XY-plane. Reference signals and experimental results

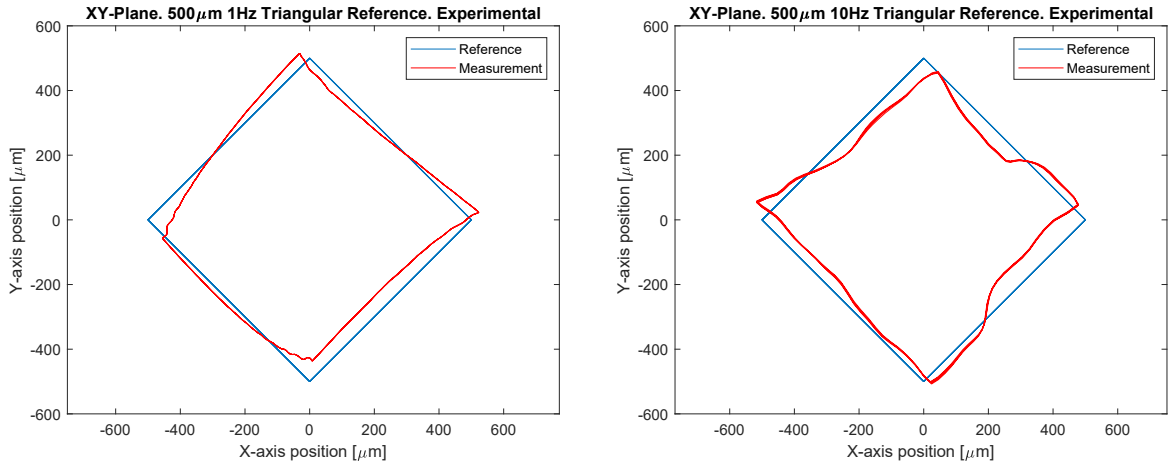

Figure 5.13: Triangular wave reference signals 500 µm on both axes. XY-plane. Reference signals and experimental results

The maximum absolute and the RMS values of the position error are reported in Table 5.5 for different amplitudes and frequencies of the triangular reference signals.

As for the simulations, when the amplitude or frequency increases it is more difficult to follow accurately the reference signal and there-

Axis	X	Y	X	Y	X	Y	X	Y
Amplitude [μm]	100	100	100	100	500	500	500	500
Frequency [Hz]	1	1	10	10	1	1	10	10
Maximum Absolute Error Value [μm]	9.51	8.90	16.2	18.3	47.8	57.2	66.1	92.0
RMS error value [μm]	1.91	1.62	6.15	7.62	25.2	39.7	33.6	44.0

Table 5.5: Maximum absolute error and RMS error values obtained with triangular reference signal. Experimental results

fore the position error increases (in terms of both maximum and RMS values). Moreover, as expected, the experimental position errors (both maximum and RMS values) are worse than in simulations. In addition, due to the signal discontinuities, the error is bigger than with the sinusoidal reference signal.

5.5 SMOOTH TRAPEZOIDAL WAVE REFERENCE SIGNAL

To overcome the velocity discontinuity problem present in the triangular waveform, a new reference signal was designed with the target drawing a square in the XY-plane. In addition, the resulting square shape is not rotated, as happens when using the triangular reference signal.
The idea was to exploit a couple of trapezoidal waveforms, with 90° phase-shift between the two signals. In this way, when one axis is moving, as the result of the application of the linear "ramp" of the trapezoidal signal, the other axis is fixed at a specified position. Unfortunately, the "ramp" of the trapezoid exhibits the same problem of discontinuity of the triangular waveform. Since the axis velocity is not required to be constant, the "ramp" of the trapezoidal signal was implemented by using half of a sinewave period (designed similarly to the one-axis reference signal reported in section 4.2). In this way, the velocity at both the beginning and at the end of the "ramp" is zero and the continuity of the signal's first derivative is guaranteed. It is important to observe that the time dedicated to the movement of one axis must coincide with the time in which the other axis remains in a fixed position. Therefore, the trapezoidal signal period was split in four equal in time parts (sinusoidal positive ramp, constant higher level, sinusoidal negative ramp, constant lower level).
The Matlab script that generates this reference signal is reported in Appendix A.7 while the time domain signals for both axes and the related XY-plane plot are shown in Figure 5.14.

As done with the sinusoidal and triangular reference signals, some simulations and experiments were performed by considering different amplitudes and frequencies of the trapezoidal reference signal. The results achieved with amplitude of 100 μm (linear range) and

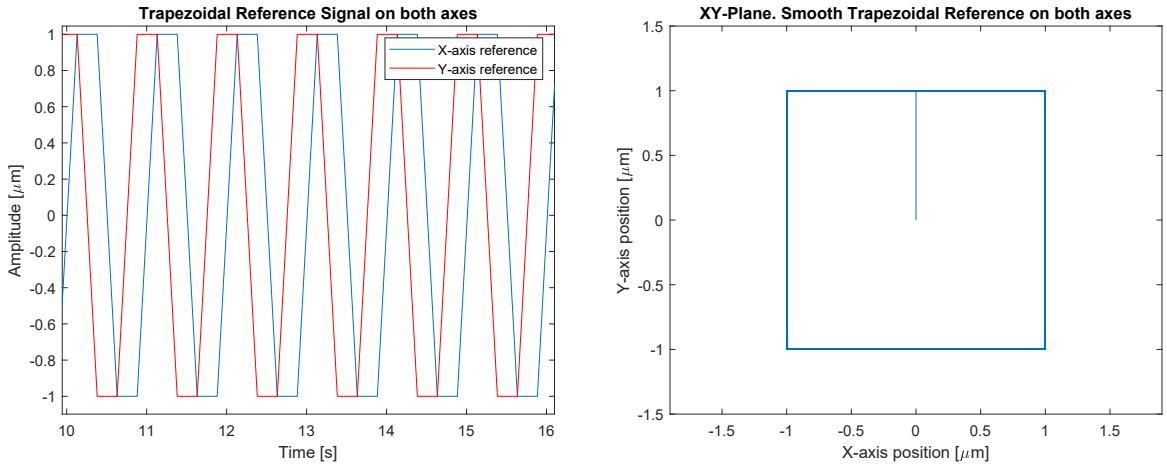

Figure 5.14: Smooth trapezoidal wave reference signals on both axes

500 µm (non-linear range) at 1Hz and 10Hz are reported in this section. The simulation results can be found in Subsection 5.5.1, while the experimental results are shown in Subsection 5.5.2.

5.5.1 *Simulation Results*

The simulation results achieved in the XY-plane with the 100 µm amplitude trapezoidal reference signal at 1 Hz and 10 Hz frequency on both axes are shown in Figure 5.15, while the results obtained when the amplitude is 500 µm are shown in Figure 5.16.

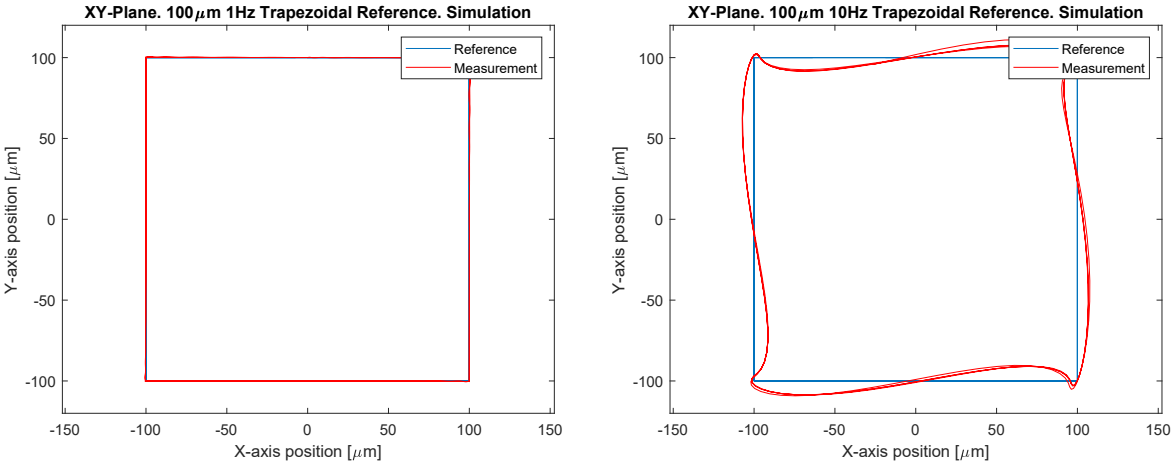

Figure 5.15: Smooth trapezoidal wave reference signals 100 µm on both axes. XY-plane. Reference signals and simulation results

The maximum absolute and RMS (Root Mean Square) values of the position error are reported in Table 5.6 for different amplitudes and frequencies of the trapezoidal reference signals.
From both the plots and data it can be noticed that the position error (expressed in terns of RMS or maximum values) is slightly worse

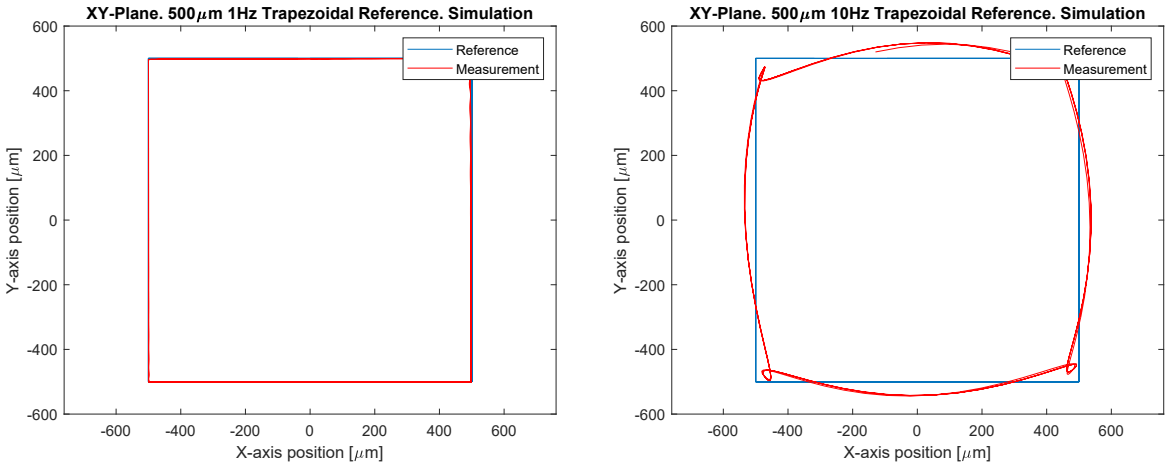

Figure 5.16: Smooth trapezoidal wave reference signals 500 µm on both axes. XY-plane. Reference signal and simulation results

than the one obtained with the sinusoidal reference signal. Moreover, the difference increases at the higher frequency and higher amplitude chosen. This is probably due to the acceleration signal discontinuities. However, comparing the results with those related to the triangular reference signal, the improvement achieved is clear and the advantage of using this reference when drawing a square in the XY-plane is evident, especially in terms of RMS error value.

Axis	X	Y	X	Y	X	Y	X	Y
Amplitude [µm]	100	100	100	100	500	500	500	500
Frequency [Hz]	1	1	10	10	1	1	10	10
Maximum Absolute Error Value [µm]	0.55	0.48	8.52	9.05	9.93	8.87	62.1	71.5
RMS error value [µm]	0.23	0.19	2.08	2.35	3.50	2.84	14.3	17.3

Table 5.6: Maximum absolute error and RMS error values obtained with smooth trapezoidal reference signal. Simulation results

5.5.2 *Experimental Results*

The experimental results achieved in the XY-plane with the 100 µm amplitude trapezoidal reference signals at 1 Hz and 10 Hz frequency on both axes are shown in Figure 5.17, while the results obtained when the amplitude is 500 µm are shown in Figure 5.18.

The maximum absolute and RMS values of the position error are reported in Table 5.7 for different amplitudes and frequencies of the trapezoidal reference signals.

From both the plot and the error values, the big error produced with the 500 µm amplitude trapezoidal reference signal at 10 Hz frequency is evident. The obtained result is very different from the

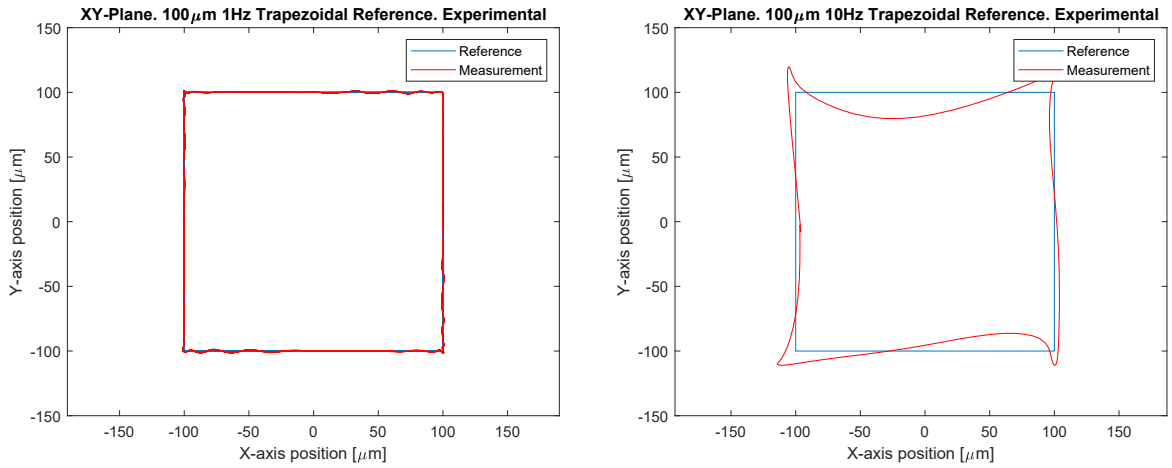

Figure 5.17: Smooth trapezoidal wave reference signals 100 µm on both axes. XY-plane. Reference signal and experimental results

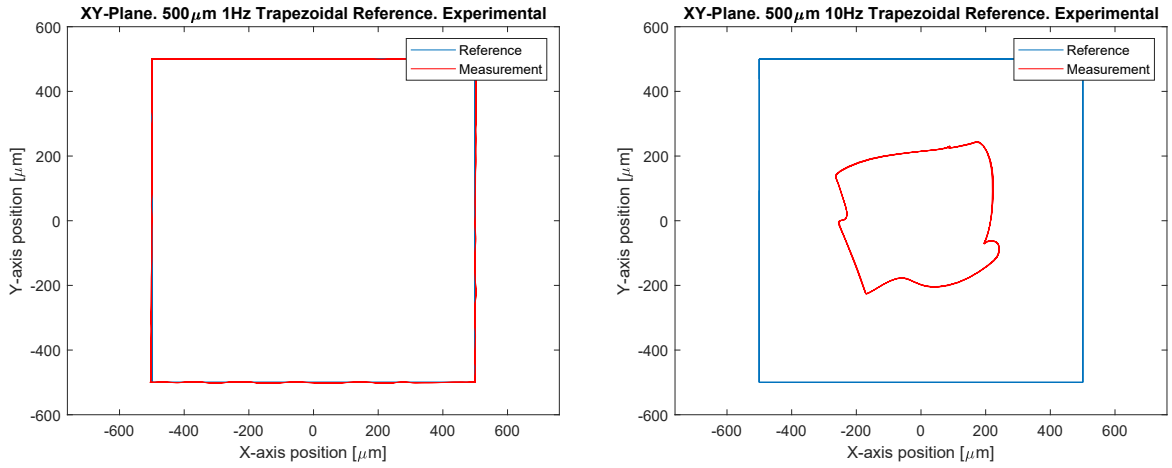

Figure 5.18: Smooth trapezoidal wave reference signals 500 µm on both axes. XY-plane. Reference signal and experimental results

Axis	X	Y	X	Y	X	Y	X	Y
Amplitude [µm]	100	100	100	100	500	500	500	500
Frequency [Hz]	1	1	10	10	1	1	10	10
Maximum Absolute Error Value [µm]	10.7	10.5	21.1	24.3	9.03	12.8	375	416
RMS error value [µm]	1.58	1.82	8.78	10.48	3.24	2.40	261	284

Table 5.7: Maximum absolute error and RMS error values obtained with smooth trapezoidal reference signal. Experimental Results

one returned by the simulation. To understand the cause of this bad behaviour, the discrete Fourier transforms of the three selected reference signals at frequency 10 Hz and normalized amplitude were evaluated over an observation interval of duration 10 periods. The result is shown in Figure 5.19. Moreover, the amplitudes of the first and the third harmonics were measured and the obtained results are reported in Table 5.8.

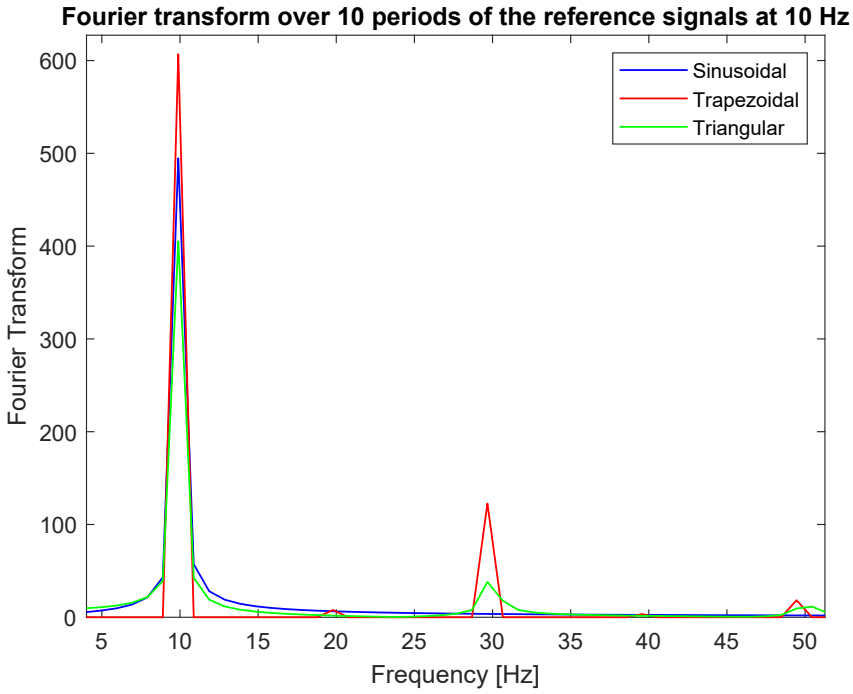

Figure 5.19: Fourier transform over 10 periods of the reference signals at 10 Hz

	Sinusoidal	Trapezoidal	Triangular	$\frac{\text{Trapezoidal}}{\text{Sinusoidal}}$	$\frac{\text{Trapezoidal}}{\text{Triangular}}$
1st harmonic	495	607	405	1.23	1.49
3rd harmonic	0	113	38	-	2.97

Table 5.8: Reference signal Fourier transform analysis

Both the plot and the numerical values in Table 5.8 show that, for the same signal amplitude and frequency, the fundamental of the smooth trapezoidal signal is about 1.23 and 1.49 times that of the sinusoidal and the triangular waveform fundamentals, respectively. Moreover, to make the behaviour even worse the third harmonic of the smooth trapezoidal signal is about 2.97 times that of the triangular one. Due to these higher amplitudes of both the first and the third harmonic, to perform a given movement at a given speed, the system needs to absorb more power from the supply when a trapezoidal reference signal is used.

As a further check, the powers of the three selected reference signals were evaluate over exactly 10 periods, obtaining the following values:

- Sinusoidal reference signal power: 0.496
- Trapezoidal reference signal power: 0.753
- Triangular reference signal power: 0.337

These values confirm that the power required by the smooth trapezoidal reference signal is higher than the one associate to the other two signals. In particular, it can be noticed that the trapezoidal reference signal power requires more than double the signal power associated with the triangular signal.
Therefore, it can reasonably be concluded that the bad system behaviour achieved with the 500 μm trapezoidal reference signal at 10 Hz is due the higher power request to perform the movement, and that this is probably bigger than the power limit of the power supply or the amplifiers. This justifies also the cause of the extremely different behaviour between the experimental and the simulation (where there is no power limit) analysis.
In contrast, for lower values of the smooth trapezoidal reference signal amplitude and frequency, the simulation and experimental results show a similar behaviour. At 1 Hz, in most cases the error is only slightly higher than the one obtained with the sinusoidal reference signal, but smaller than the one obtained with triangular waveform. When the reference signal frequency is at 10Hz with 100 μm amplitude, the system performance is quite poor and the error is slightly higher than the one obtained with the triangular reference signal. This behaviour is probably due to the significant power of the third harmonic of the trapezoidal signal. Therefore, we can conclude that the smooth trapezoidal reference signal provides a significant improvement in the system behaviour compared to the triangular reference signal as long as the adopted frequency is low enough. Moreover, it has the advantage that the obtained square shape in the XY-plane is not rotated with respect to the axis of the XY-plane. However, when the frequency grows, the trapezoidal reference signal provides poor performance, probably due to the limited power capabilities of the adopted circuits, whose effect overcome the one due to the discontinuity in the derivatives of the triangular reference signal.

5.5.3 *Rectangular Shape using Smooth Trapezoidal Reference Signal*

Using trapezoidal reference signals of different amplitudes it is possible to obtain rectangular trajectories on the XY-plane. With this aim, the amplitudes related to the two axes reference signals have to be different. As an example, two different rectangular trajectories were

plotted using a couple of trapezoidal reference signals at 2 Hz. The related experimental results are shown in Figures 5.20.

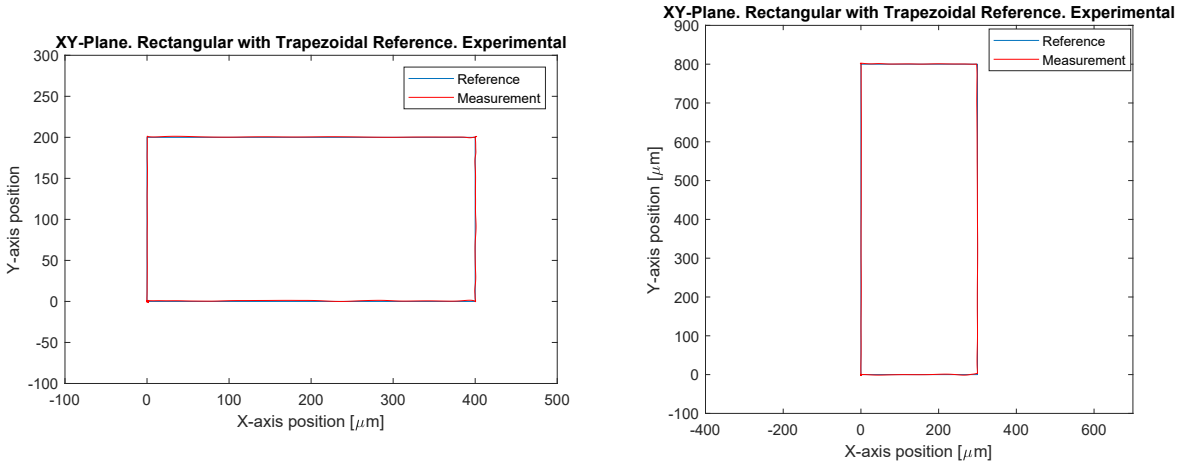

Figure 5.20: Smooth trapezoidal wave reference signals with different amplitudes on both axes. Examples of rectangular shape in the XY-plane. Reference signal and experimental results

6

CROSS-COUPLING

6.1 INTRODUCTION

In a multi-axis system, the cross-coupling interaction is an unwanted motion interference along one degree of freedom due to the motion, performed intentionally, along another degree of freedom, as shown in Figure 6.1 [8].

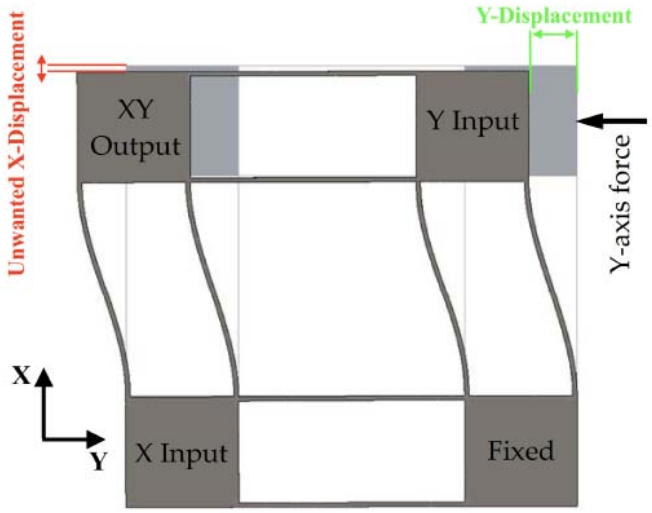

Figure 6.1: Cross-axis coupling along the X-axis in a compliant mechanism [8]

The multi-axis component of the high-precision positioning system analyzed in this thesis work is the XYZ CPM, described in Section 3.2.2; therefore, the cross-coupling effect is due to this compliant component. The manipulator studied in this thesis work is affected by two different kinds of cross-coupling interactions. The first one is the kinematic cross-coupling, which means that a movement of one axis produces an unwanted movement on the other axis. This will be analyzed in Section 6.2. The second kind of cross-coupling that arises in the system is the kinetostatic cross-coupling, which increases the actuation force required to perform a movement on one axis if the orthogonal axis is not in the null position. It will be explained in Section 6.3.

6.2 KINEMATIC CROSS-COUPLING

The XYZ CPM shared between the two axes was designed in [5] to be symmetric. This design feature should lead to produce parasitic rotation and parasitic translation of the XYZ CPM component much smaller than that due to the primary translation. However, measurements showed a non-negligible parasitic movement on one axis when the other axis is moving. The data collected and analyzed in such situation are reported in Subsection 6.2.1, while the static compensation of this unwanted effect and the results after its implementation are reported in Subsection 6.2.2.

6.2.1 *Analysis*

To analyze the kinematic cross-coupling interaction between the two axes, the primary axis was fed with position reference signals and the movement inducted on the other axis was measured. The position reference signal designed in [8] for one axis movement and reported in chapter 4 was used. This reference signal was chosen because it allows static measurement of the kinematic cross-coupling interaction and, due to its continuous derivative, the system can follow it with an extremely small error.
To quantify the magnitude of the kinematic cross-coupling interaction, the movement of the non-fed axis (due to the displacement performed on the orthogonal axis) was recorded and its amplitude was measured. Three measurements were performed for each chosen amplitude of the primary axis movement and then the average was evaluated in order to obtain more accurate results. Initially, the X-axis was fed and the movement of the Y-axis was measured, later the same analysis was performed exchanging the role of the axes. The amplitude of the position reference chosen varied in a range of ± 1000 µm, with a step of 100 µm. The data collected when the X-axis was fed are reported in Table 6.1, while the data collected when Y is the primary axis are reported in Table 6.2. In Table 6.1 X refers to the movement of the primary axis, $<Y_X>$ is the average (of the three measurement performed) of the parasitic movement of the Y-axis due to the intentional movement on the X-axis and δY_X is half-width of the range of the three performed measurements. In Table 6.2, the roles of the axes are swapped.

Data reported in tables 6.1 and 6.2 show that the magnitude of the kinematic cross-coupling interaction differs between the two axes and, moreover, it is not symmetric around the null position of the primary axis. This behaviour is justified by the fact that this is an unwanted effect.
In Figures 6.2 and 6.3, the amplitude of the parasitic movement of the Y-axis and the X-axis, respectively, are plotted together with the

X [µm]	$<Y_X>$ [µm]	δY_X [µm]	X [µm]	$<Y_X>$ [µm]	δY_X [µm]
100	0.00	0.00	-100	0.00	0.00
200	0.00	0.00	-200	0.00	0.00
300	-0.35	0.00	-300	0.00	0.00
400	-0.52	0.01	-400	0.00	0.00
500	-0.87	0.02	-500	-0.22	0.01
600	- 1.16	0.02	-600	-0.52	0.01
700	-1.55	0.04	-700	-0.74	0.01
800	-2.04	0.04	-800	-1.17	0.02
900	-2.54	0.02	-9000	-1.52	0.03
1000	-3.28	0.01	-1000	-1.83	0.02

Table 6.1: Kinematic Cross-Coupling interaction on the Y-axis due to the movement of the X-axis. X represents to the movement of the X-axis, $<Y_X>$ is the average of three measurements of the parasitic movement of the Y-axis and δY_X is the half-width of the range of the performed measurements

Y [µm]	$<X_Y>$ [µm]	δX_Y [µm]	Y [µm]	$<X_Y>$ [µm]	δX_Y [µm]
100	-0.13	0.00	-100	0.00	0.00
200	-0.29	0.01	-200	0.12	0.01
300	-0.51	0.02	-300	0.00	0.00
400	-0.74	0.02	-400	0.00	0.00
500	-1.06	0.04	-500	-0.17	0.02
600	-1.45	0.03	-600	-0.30	0.02
700	-1.96	0.02	-700	-0.51	0.01
800	-2.53	0.05	-800	-0.77	0.03
900	-3.40	0.05	-9000	-1.08	0.01
1000	-4.16	0.04	-1000	-1.43	0.03

Table 6.2: Kinematic Cross-Coupling interaction on the X-axis due to the movement of the Y-axis. Y represents to the movement of the Y-axis, $<X_Y>$ is the average of three measurements of the parasitic movement of the X-axis and δX_Y is the half-width of the range of the performed measurements

corresponding linear and cubic fittings. It is clear from the figures, the kinematic cross-coupling interaction exhibits a cubic behaviour with respect to the movement of the fed-axis.

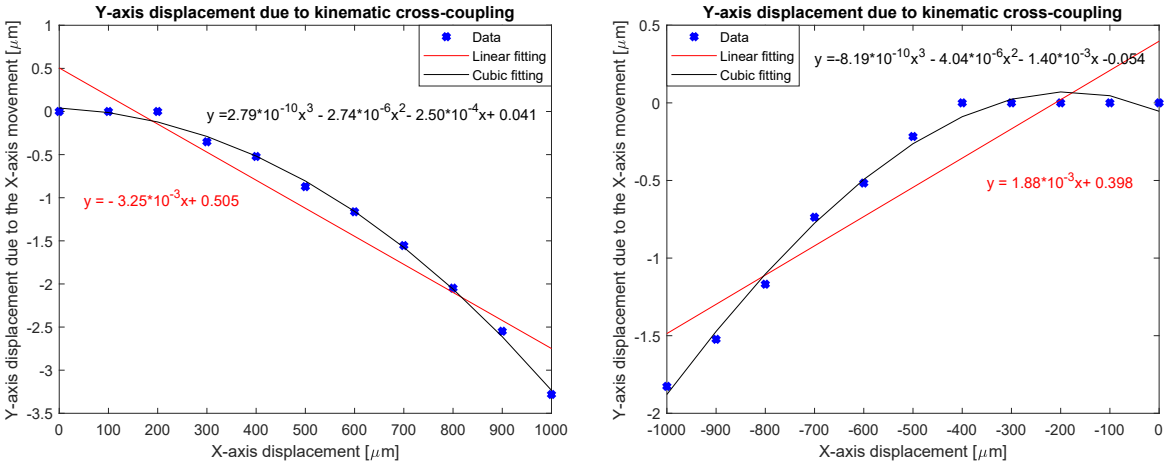

Figure 6.2: Kinematic Cross- Coupling. Y-axis parasitic movement due to X-axis displacement

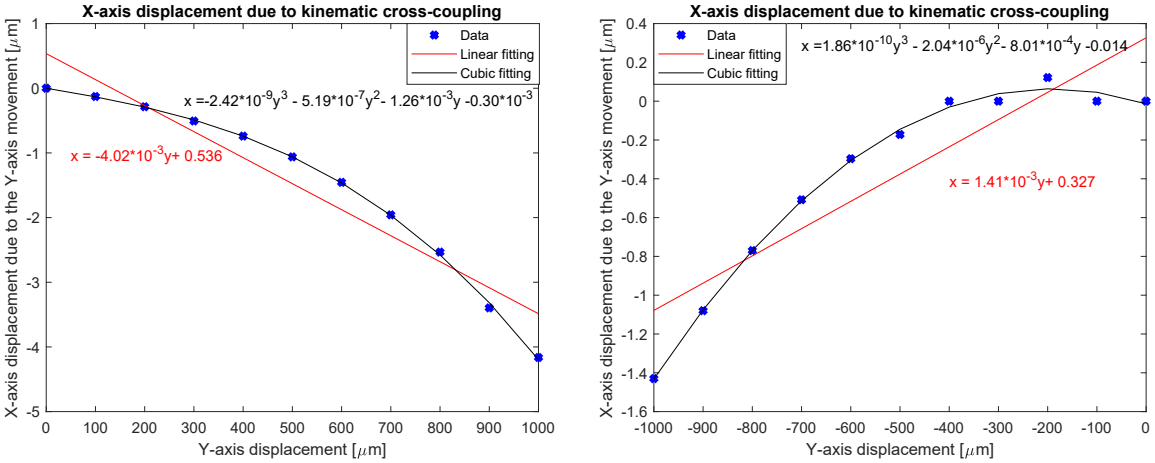

Figure 6.3: Kinematic Cross- Coupling. X-axis parasitic movement due to Y-axis displacement

Data show that the unwanted kinematic cross-coupling interaction is always less than 1% of the amplitude of the movement on the primary axis. However, since the target is to perform high-precision movement with the manipulator, it was decided to compensate for this unwanted effect, even if it is quite small.

6.2.2 *Compensation*

Although the analysis performed in the previous subsection shows that the kinematic cross-coupling interaction exhibits a cubic behaviour, due to its small magnitude, it was decided to compensate only its lin-

ear contribution since this can be implemented more simply and the residual effect can be neglected.
The information about the amplitude of the kinematic cross-coupling was used to modify the feed-forward inputs.
The Simulink model for the control of both axes, which includes also the kinematic cross-coupling compensation block, is reported in Figure 6.4, while the compensation block is shown in Figure 6.5. As can be seen from Figure 6.4 the feed-forward block was split into two equal blocks. This choice allows the compensation only of the direct feed-forward system, without affecting the observer input (that is used for feedback).

The Matlab function that implements the compensation can be found in appendix A.8 and it is based on the following matrix, where the values A and B in the matrix are the opposite of the slopes of the linear fittings shown Figures 6.2 and 6.3.

$$\begin{Bmatrix} X_o \\ \dot{X}_o \\ \ddot{X}_o \\ Y_o \\ \dot{Y}_o \\ \ddot{Y}_o \end{Bmatrix} = \begin{bmatrix} 1 & 0 & 0 & A & 0 & 0 \\ 0 & 1 & 0 & 0 & A & 0 \\ 0 & 0 & 1 & 0 & 0 & A \\ B & 0 & 0 & 1 & 0 & 0 \\ 0 & B & 0 & 0 & 1 & 0 \\ 0 & 0 & B & 0 & 0 & 1 \end{bmatrix} \begin{Bmatrix} X_i \\ \dot{X}_i \\ \ddot{X}_i \\ Y_i \\ \dot{Y}_i \\ \ddot{Y}_i \end{Bmatrix} \tag{6.1}$$

Matrix (6.1) provides only a static compensation of the kinematic cross-coupling effect since only steady-state position data are used. Indeed, a dynamic compensation would require a more complex compensation based also on velocity and acceleration measurements. Therefore, in this work only the static compensation is implemented. In the next figures, some examples of the position plots related to the non-fed axis are reported without, and with, the implementation of the static compensation. Figures 6.6 and 6.7 show the Y-axis movement when the displacement on the X-axis was 800 µm or −800 µm, respectively; while Figure 6.8 and 6.9 show the X-axis movement when the displacement on the Y-axis was 800 µm or −800 µm, respectively.

As it can be seen from Figures 6.6 - 6.9, without the compensation the kinematic cross-coupling effect produces an unwanted movement on the non-fed axis and there is a measurable steady-state effect. Conversely, when the compensation is implemented, the steady-state effect becomes negligible, and only a transient behaviour can be detected. Therefore it can be concluded that the proposed static compensation works as expected.

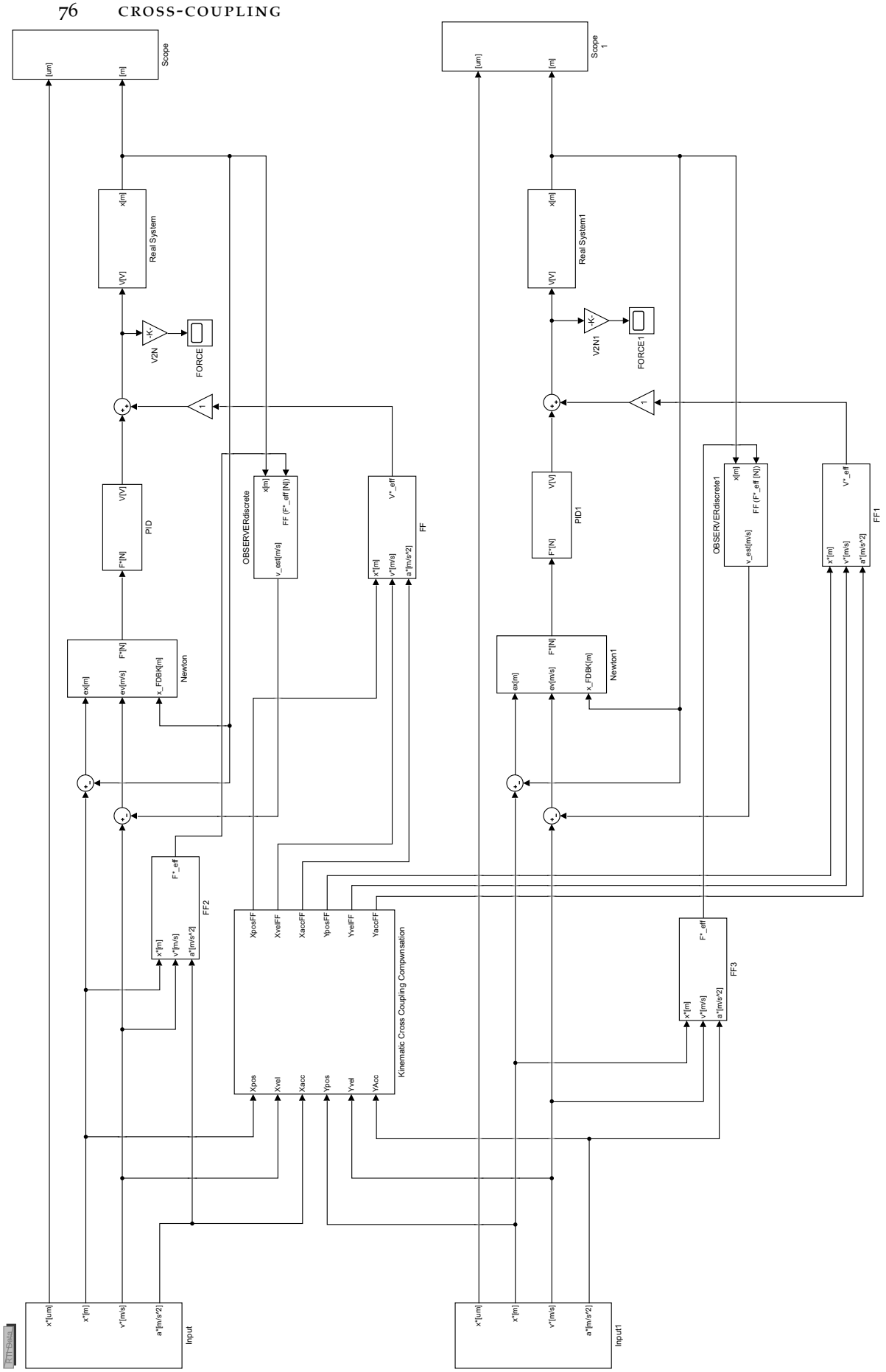

Figure 6.4: Two Axes Control Scheme in Simulink with Kinematic Cross-Coupling Compensation

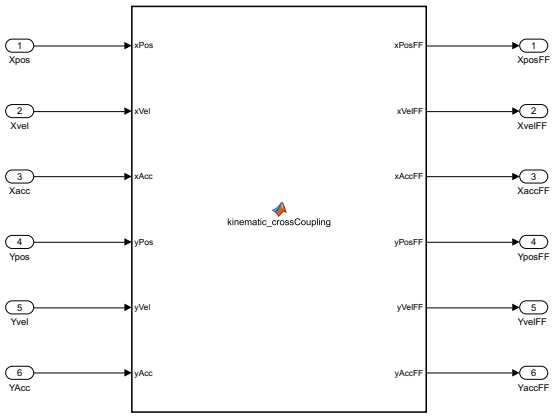

Figure 6.5: Kinematic Cross - Coupling Simulink Block

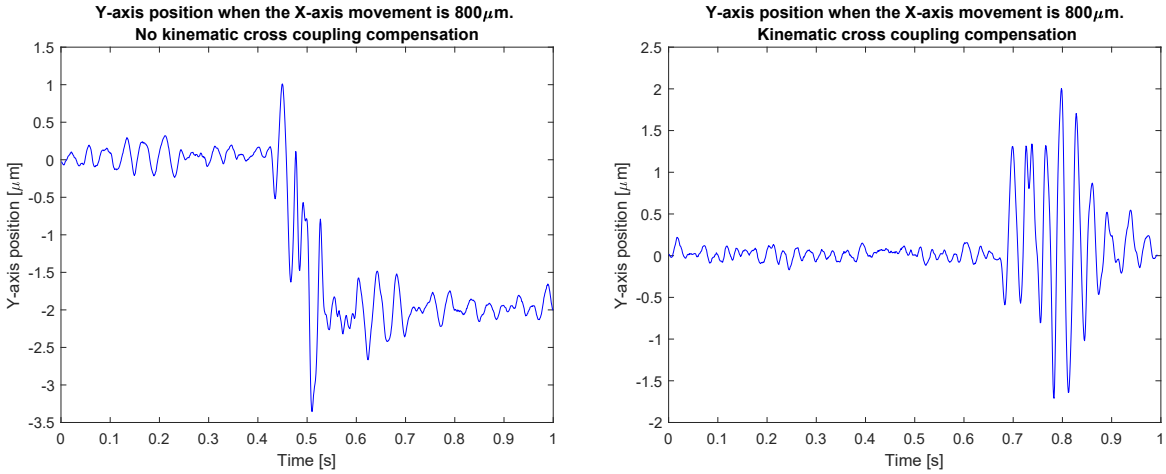

Figure 6.6: Y-Axis Movement due to X-axis 800µm displacement. Without and With Kinematic Cross-Coupling Compensation

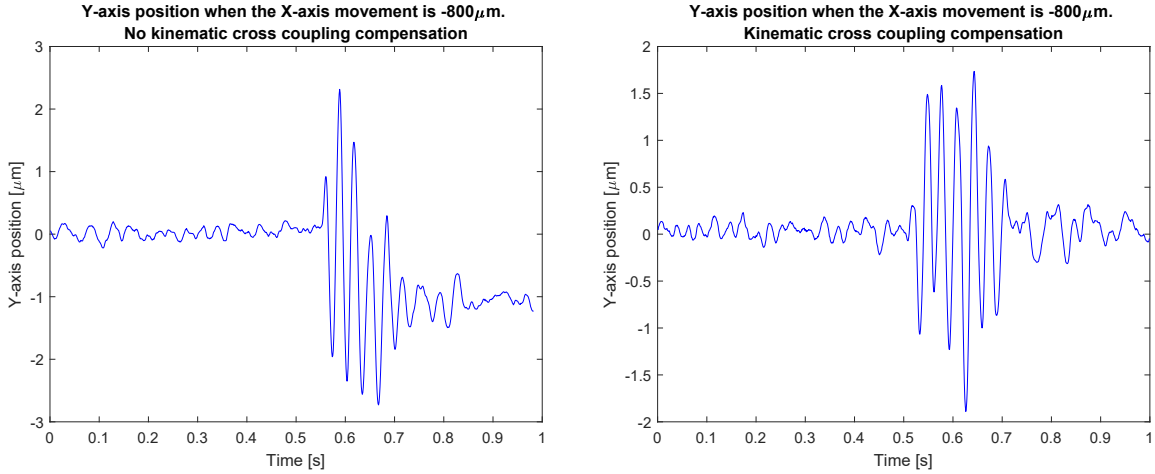

Figure 6.7: Y-Axis Movement due to X-axis −800µm displacement. Without and With Kinematic Cross-Coupling Compensation

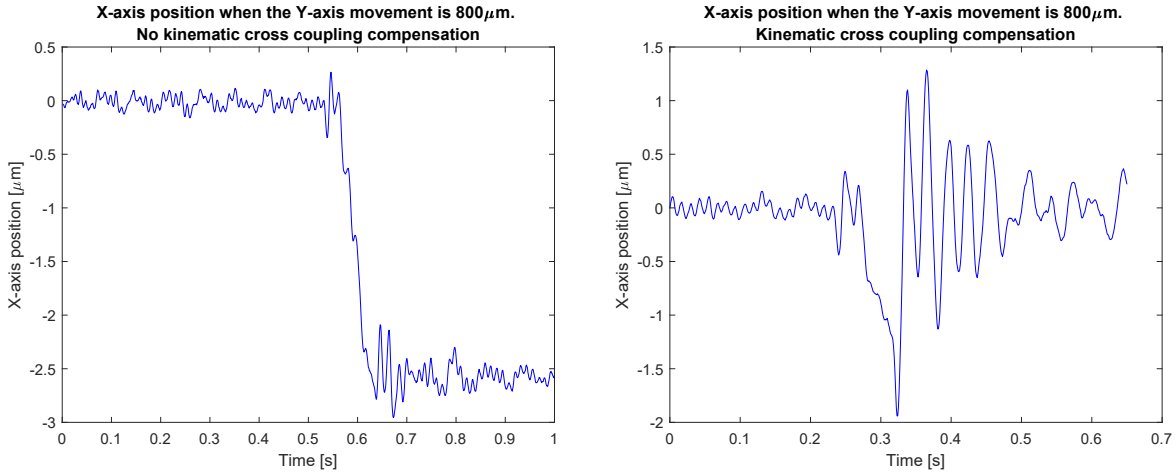

Figure 6.8: X-Axis Movement due to Y-axis 800µm displacement. Without and With Kinematic Cross-Coupling Compensation

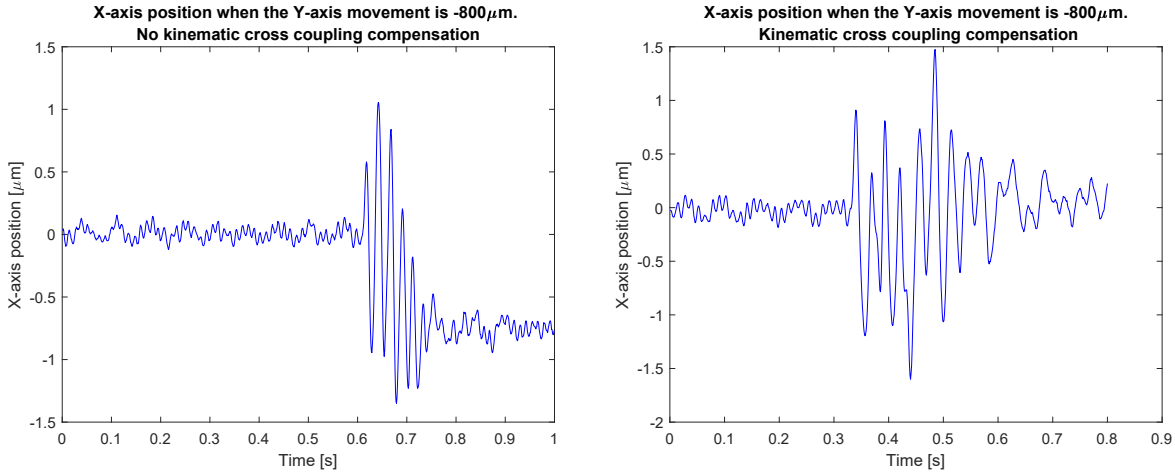

Figure 6.9: X-Axis Movement due to Y-axis −800µm displacement. Without and With Kinematic Cross-Coupling Compensation

6.3 KINETOSTATIC CROSS-COUPLING

In [5] it has been proved that the actuation stiffness along the X-axis increases when the primary translation along the Y-axis direction increases. This was verified both analytically and experimentally. As the motion characteristics of the symmetric XYZ CPM along the three axes are isotropic, what is true for the X-axis holds also for the other axes.

6.3.1 *Analysis*

In chapter 3, the theoretical actuation force required to perform a movement along one axis was evaluated without considering the kinetostatic cross-coupling interaction with the other axes. In [5] the normalized actuation force equations, considering also the kinetostatic cross-coupling interaction between the axes, were obtained neglecting the dynamic contribution because the primary translation was considered to be slow varying. The same normalization factors used in Chapter 3 were adopted in the following: the translational displacements are normalized by the beam actual length L, while the forces are normalized by EI/L^2, where E is the Young's modulus and I is the second moment of area of a rectangular cross-section. The normalized actuation force equations are reported in the following equations:

$$\begin{aligned} f_x = &\frac{48x_s(129x_s^2 + 129z_s^2 + 175t^2)}{3x_s^2 + 3z_s^2 + 175t^2} + \\ &\frac{48x_s(129x_s^2 + 129y_s^2 + 175t^2)}{3x_s^2 + 3y_s^2 + 175t^2} + \\ &\frac{192x_s(129x_s^2 + 175t^2)}{3x_s^2 + 175t^2} \end{aligned} \tag{6.2}$$

$$\begin{aligned} f_y = &\frac{48y_s(129y_s^2 + 129z_s^2 + 175t^2)}{3y_s^2 + 3z_s^2 + 175t^2} + \\ &\frac{48y_s(129y_s^2 + 129x_s^2 + 175t^2)}{3y_s^2 + 3x_s^2 + 175t^2} + \\ &\frac{192y_s(129y_s^2 + 175t^2)}{3y_s^2 + 175t^2} \end{aligned} \tag{6.3}$$

$$
\begin{aligned}
f_z = &\frac{48z_s(129z_s^2 + 129x_s^2 + 175t^2)}{3z_s^2 + 3x_s^2 + 175t^2} + \\
&\frac{48z_s(129z_s^2 + 129y_s^2 + 175t^2)}{3z_s^2 + 3y_s^2 + 175t^2} + \\
&\frac{192z_s(129z_s^2 + 175t^2)}{3z_s^2 + 175t^2}
\end{aligned}
\tag{6.4}
$$

where:
- f_x is the normalized actuation force of the x-axis,
- f_y is the normalized actuation force of the y-axis,
- f_z is the normalized actuation force of the z-axis,
- x_s is the normalized displacement of the x-axis,
- y_s is the normalized displacement of the y-axis,
- z_s is the normalized displacement of the z-axis,

and
- t is the normalized thickness of the beam.

An evaluation of the increase Δf_{xy} of the X-axis actuation force due to the kinetostatic cross-coupling with the Y-axis is required. This increase is evaluated as the difference between the force along the X-axis related to given displacements along the X-axis and Y-axis ($f_x(z_s = 0)$) and the force along the X-axis related to a given displacement along only the X-axis ($f_x(y_s = 0, z_s = 0)$).

$$
\begin{aligned}
\Delta f_{xy} &= f_x(z_s = 0) - f_x(y_s = 0, z_s = 0) = \\
&= \frac{48x_s(129x_s^2 + 129y_s^2 + 175t^2)}{3x_s^2 + 3y_s^2 + 175t^2} - \frac{48x_s(129x_s^2 + 175t^2)}{3x_s^2 + 175t^2} = \\
&= 48x_s[\frac{(129x_s^2 + 129y_s^2 + 175t^2)(3x_s^2 + 175t^2) - (129x_s^2 + 175t^2)(3x_s^2 + 3y_s^2 + 175t^2)}{(3x_s^2 + 3y_s^2 + 175t^2)(3x_s^2 + 175t^2)}] \\
&= 48x_s[\frac{129 \cdot 175y_s^2t^2 - 175 \cdot 3y_s^2t^2}{(3x_s^2 + 3y_s^2 + 175t^2)(3x_s^2 + 175t^2)}] = \\
&= \frac{1058400x_sy_s^2t^2}{(3x_s^2 + 3y_s^2 + 175t^2)(3x_s^2 + 175t^2)}
\end{aligned}
\tag{6.5}
$$

Considering the normalization factors, equation (6.5) become:

$$
\frac{\Delta F_{xy}}{\frac{EI}{L^2}} = \frac{1058400\frac{X_s}{L}\frac{Y_s^2}{L^2}\frac{T^2}{L^2}}{(3\frac{X_s^2}{L^2} + 3\frac{Y_s^2}{L^2} + 175\frac{T^2}{L^2})(3\frac{X_s^2}{L^2} + 175\frac{T^2}{L^2})}
\tag{6.6}
$$

Therefore:

$$
\Delta F_{xy} = \frac{EI}{L^3}\frac{1058400X_sY_s^2T^2}{(3X_s^2 + 3Y_s^2 + 175T^2)(3X_s^2 + 175T^2)}
\tag{6.7}
$$

The same analysis can be done for the other axes and the same results will be obtained, due to the symmetry of the XYZ CPM. Using the equation (6.7), the behaviour of the X-axis actuation force increases due to the kinetostatic cross-coupling with the Y-axis. This is plotted and the obtained result is shown in Figure 6.10.

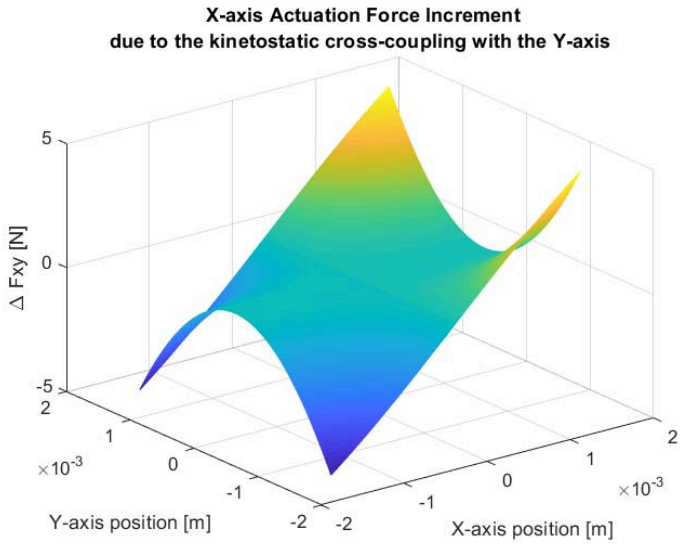

Figure 6.10: 3D plot of the X-axis actuation force increment due to the kinetostatic cross-coupling interaction with the Y-axis

As it can be seen from Figure 6.10, the increment of the X-axis actuation force is significant only when both axes are far from the null position. Indeed, the 3D plot is flat and the force increment is negligible when at least one of the two axes position is small.
As written above, the theoretical analysis performed for the X-axis actuation force increment due to kinetostatic cross-coupling interaction with the Y-axis holds also for all the other axes combinations.

The effect of the kinetostatic cross-coupling interaction was verified experimentally. For this purpose, one axis was held in a constant position (0 mm, 0.5 mm, 1 mm , -0.5 mm and -1 mm) and the actuation force needed to perform a given displacement on the other axis was recorded. Three measurements were performed and the average value was evaluated in order to obtain more accurate results. In Table 6.3, the data regarding the average $< F_x >$ of the X-axis force when the position of the Y-axis is null and the half-width δF_x of the range of the three performed measurements are reported. Moreover, the averages of the X-axis actuation force increment $< \Delta F_{xy} >$ due to the kinetostatic cross-coupling corresponding to different Y-axis constant positions are also reported. The range of variation of the X-axis actuation force increment is not reported in the table for the sake of conciseness. However, it is similar to δF_x. The data reported in Table 6.3 for the average X-axis actuation force are shown in Figure 6.11 for

different Y-axis constant positions; the corresponding cubic fitting is also reported. Moreover, the increments of the X-axis force due to the kinetostatic cross-coupling are shown in Figure 6.12 in the case when the Y-axis is held at ± 1 mm, the corresponding linear fitting is also reported. The same analysis was performed on the Y-axis actuation force, considering different X-axis constant positions. The results are shown in Table 6.4 and Figures 6.13 and 6.14.

x [µm]	$<F_x>$ [N] $y = 0$ mm	δF_x [N] $y = 0$ mm	$<\Delta F_{xy}>$ [N] $y = 0.5$ mm	$<\Delta F_{xy}>$ [N] $y = 1$ mm	$<\Delta F_{xy}>$ [N] $y = -0.5$ mm	$<\Delta F_{xy}>$ [N] $y = -1$ mm
100	9.61	0.01	+0.08	+0.18	+0.02	+0.07
200	19.72	0.01	+0.09	+0.21	+0.02	+0.08
300	30.66	0.02	+0.15	+0.38	+0.09	+0.19
400	42.41	0.02	+0.18	+0.44	+0.05	+0.13
500	54.25	0.03	+0.29	+0.83	+0.71	+0.99
600	68.62	0.01	+0.39	+0.96	+0.86	+1.11
700	84.44	0.03	+0.41	+1.12	+0.47	+0.87
800	101.75	0.05	+0.46	+0.93	+0.60	+0.80
900	120.58	0.07	+0.83	+1.27	+0.63	+1.07
1000	141.19	0.07	+1.41	+1.60	+0.72	+0.39
-100	-10.59	0.01	-0.09	-0.18	-0.12	-0.16
-200	-20.38	0.01	-0.15	-0.37	-0.16	-0.29
-300	-30.51	0.01	-0.20	-0.63	-0.19	-0.35
-400	-40.68	0.01	-0.24	-0.88	-0.09	-0.55
-500	-52.56	0.01	-0.29	-0.79	-0.65	-0.98
-600	-64.68	0.02	-0.28	-0.84	-0.29	-0.79
-700	-77.80	0.02	-0.32	-0.98	-0.30	-0.85
-800	-90.75	0.06	-0.51	-1.59	-2.63	-3.57
-900	-106.55	0.02	-0.36	-1.39	-3.61	-4.32
-1000	-126.19	0.07	-0.28	-1.02	-0.99	-2.23

Table 6.3: Kinetostatic Cross-Coupling interaction. X-Axis force needed to perform a specific X-axis movement with the Y-Axis fixed at different positions. x represents to the movement of the X-axis, $<F_x>$ is the average of three actuation force measurements, δF_x is the half-width of the range of the performed measurements and $<\Delta F_{xy}>$ is the average of the X-axis actuation force increment due to the kinetostatic cross-coupling.

6.3.2 *Compensation*

Since data shows that the required force increase is around 1% when the largest displacement is considered, (that is about 10 µm for a dis-

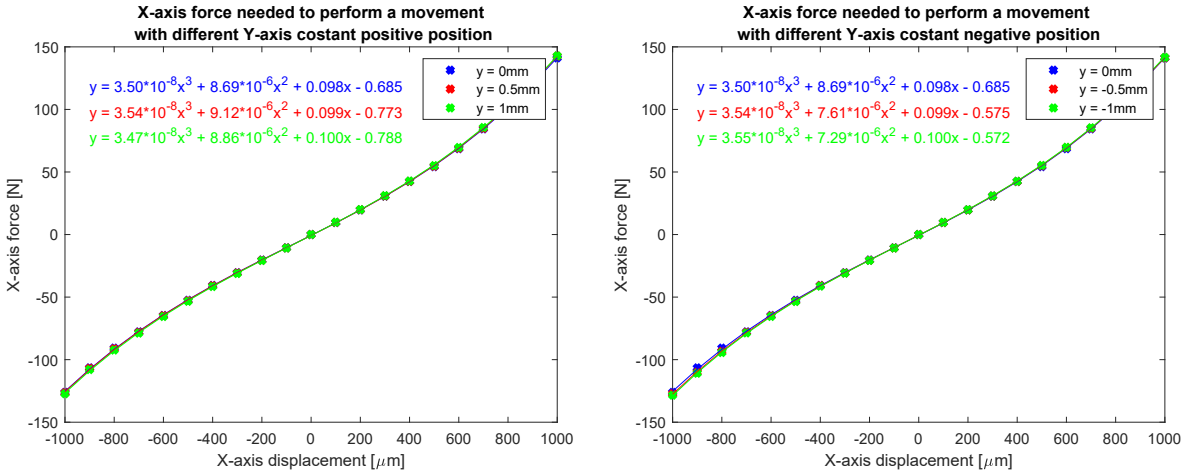

Figure 6.11: X-Axis force needed to cause a movement on the X-axis considering different constant displacement on the Y-axis

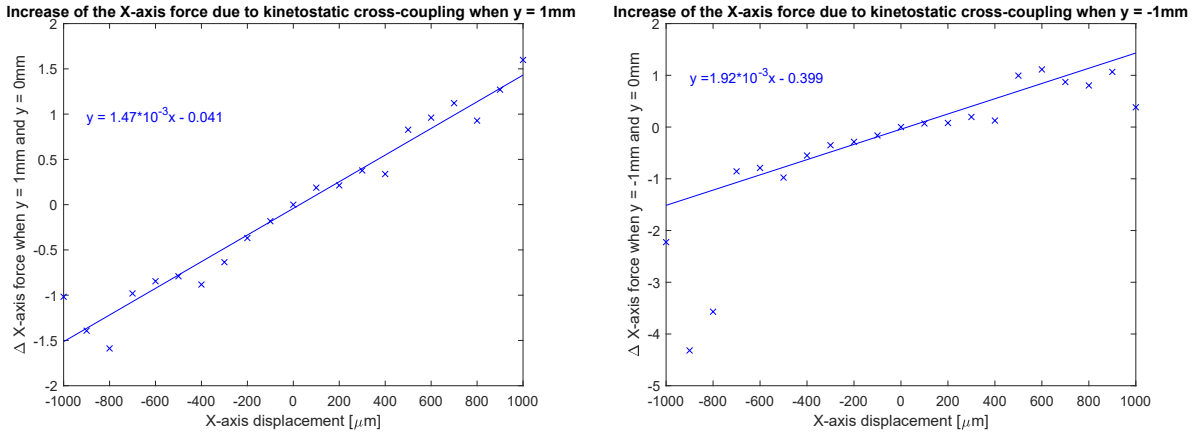

Figure 6.12: Increment of the X-Axis force needed to cause a movement on the X-axis with different constant displacement on the Y-axis

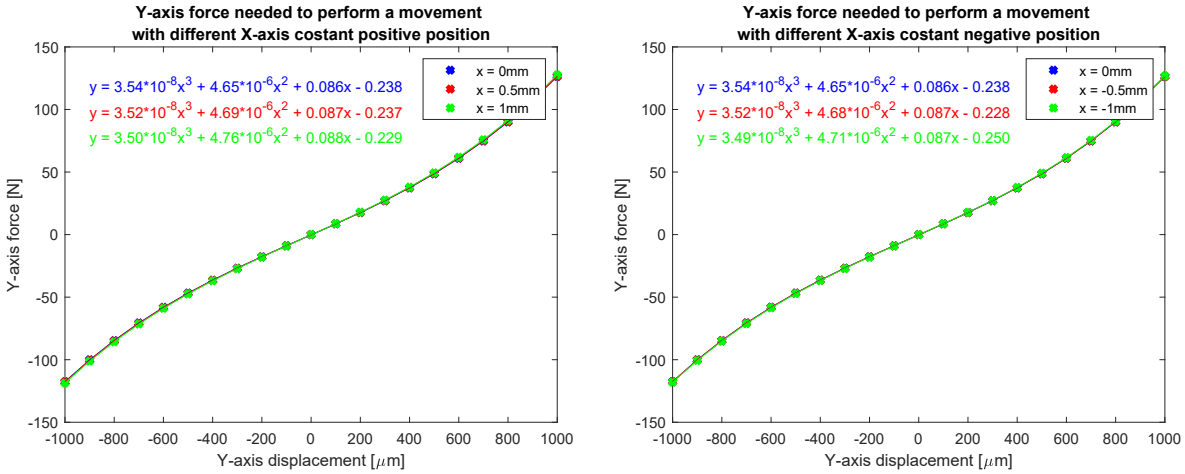

Figure 6.13: Y-Axis force needed to cause a movement on the Y-axis considering different constant displacement on the X-axis

y [μm]	$\langle F_y \rangle$ [N] $x = 0$ mm	δF_y [N] $x = 0$ mm	$\langle \Delta F_{yx} \rangle$ [N] $x = 0.5$ mm	$\langle \Delta F_{yx} \rangle$ [N] $x = 1$ mm	$\langle \Delta F_{yx} \rangle$ [N] $x = -0.5$ mm	$\langle \Delta F_{yx} \rangle$ [N] $x = -1$ mm
100	8.66	0.01	+0.02	+0.13	+0.01	+0.05
200	17.57	0.01	+0.09	+0.30	+0.07	+0.18
300	27.05	0.01	+0.13	+0.53	+0.05	+0.23
400	37.31	0.01	+0.18	+0.60	+0.10	+0.35
500	48.58	0.01	+0.19	+0.73	+0.15	+0.45
600	61.01	0.01	+0.23	+0.81	+0.08	+0.37
700	74.77	0.01	+0.30	+1.04	+0.23	+0.59
800	90.03	0.01	+0.51	+1.25	+0.09	+0.62
900	107.32	0.03	+0.25	+1.13	+0.04	+0.40
1000	126.36	0.07	+0.28	+1.27	+0.02	+0.45
-100	-8.91	0.02	-0.09	-0.23	-0.14	-0.25
-200	-17.71	0.02	-0.11	-0.30	-0.08	-0.24
-300	-26.90	0.01	-0.10	-0.39	-0.02	-0.23
-400	-36.46	0.02	-0.12	-0.50	-0.02	-0.24
-500	-46.77	0.01	-0.18	-0.64	-0.05	-0.35
-600	-58.12	0.01	-0.23	-0.80	-0.03	-0.36
-700	-70.61	0.02	-0.22	-0.87	-0.04	-0.54
-800	-84.75	0.01	-0.24	-0.94	-0.01	-0.37
-900	-100.07	0.05	-0.31	-1.05	-0.02	-0.55
-1000	-117.58	0.03	-0.25	-1.03	-0.02	-0.33

Table 6.4: Kinetostatic Cross-Coupling interaction. Y-Axis force needed to perform a specific Y-axis movement with the X-Axis fixed at different positions. y represents to the movement of the Y-axis, $\langle F_y \rangle$ is the average of three actuation force measurements, δF_y is the half-width of the range of the performed measurements and $\langle \Delta F_{yx} \rangle$ is the average of the Y-axis actuation force increment due to the kinetostatic cross-coupling.

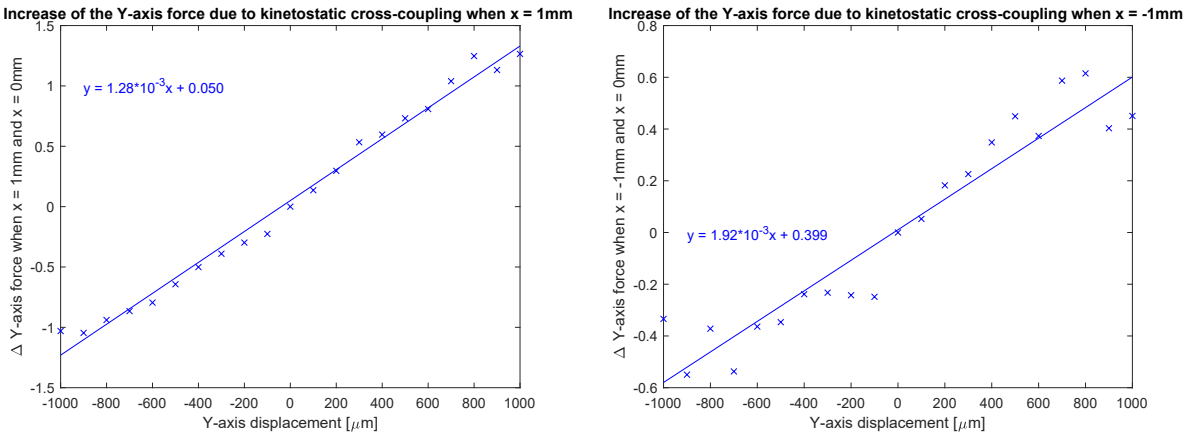

Figure 6.14: Increment of the Y-axis force needed to cause a movement on the Y-axis with different constant displacement on the X-axis

placement of 1 mm), it has to be compensate to ensure high system performance.

The approach used to compensated the kinetostatic cross-coupling interaction has been described in section 2.4. Measurement results show that the force needed to perform a movement on the X-axis is a function of the position of both axes, but the effect of y is much smaller than the effect of x. Consequently, the behaviour of the actuation force can be accurately expressed using the Taylor's series about $y = 0$, truncated to the first order term.

$$F_x = f(x, y) = f(x, 0) + f'(x, 0)y \tag{6.8}$$

In (6.8), the first term, $f(x, 0)$ is the output of the feed-forward term when the cross-coupling interaction is not considered. Due to the small contribution of the second term of (6.8), the factor $f'(x, 0)$ can be reasonably approximated with the linear fitting reported in Figure 6.12, , assuming that a similar behaviour occurs also for $|y| < 1$. The same approach can be used also on the Y-axis and the term $f'(0, y)$ has been approximated with the linear fitting reported in Figure 6.14.

To implement the compensation in the Simulink control scheme, the feed-forward block in the two axes control scheme was modified, as shown in Figure 6.15, while the modified X-axis feed-forward block is shown in Figure 6.16. (The corresponding Y-axis block has been implemented in the same way). The KinetostaticCC Matlab function included in the feed-forward block is reported in Appendix A.9. This function simply implements the term $f'(x, 0)y$ (or $f'(0, y)x$ in the Y-axis case) of the truncated Taylor's series (6.8) which is then added to the one axis feed-forward force.

To verify the effectiveness of the compensation, different measurements were performed. The X-axis displacement were: 100 μm, 500

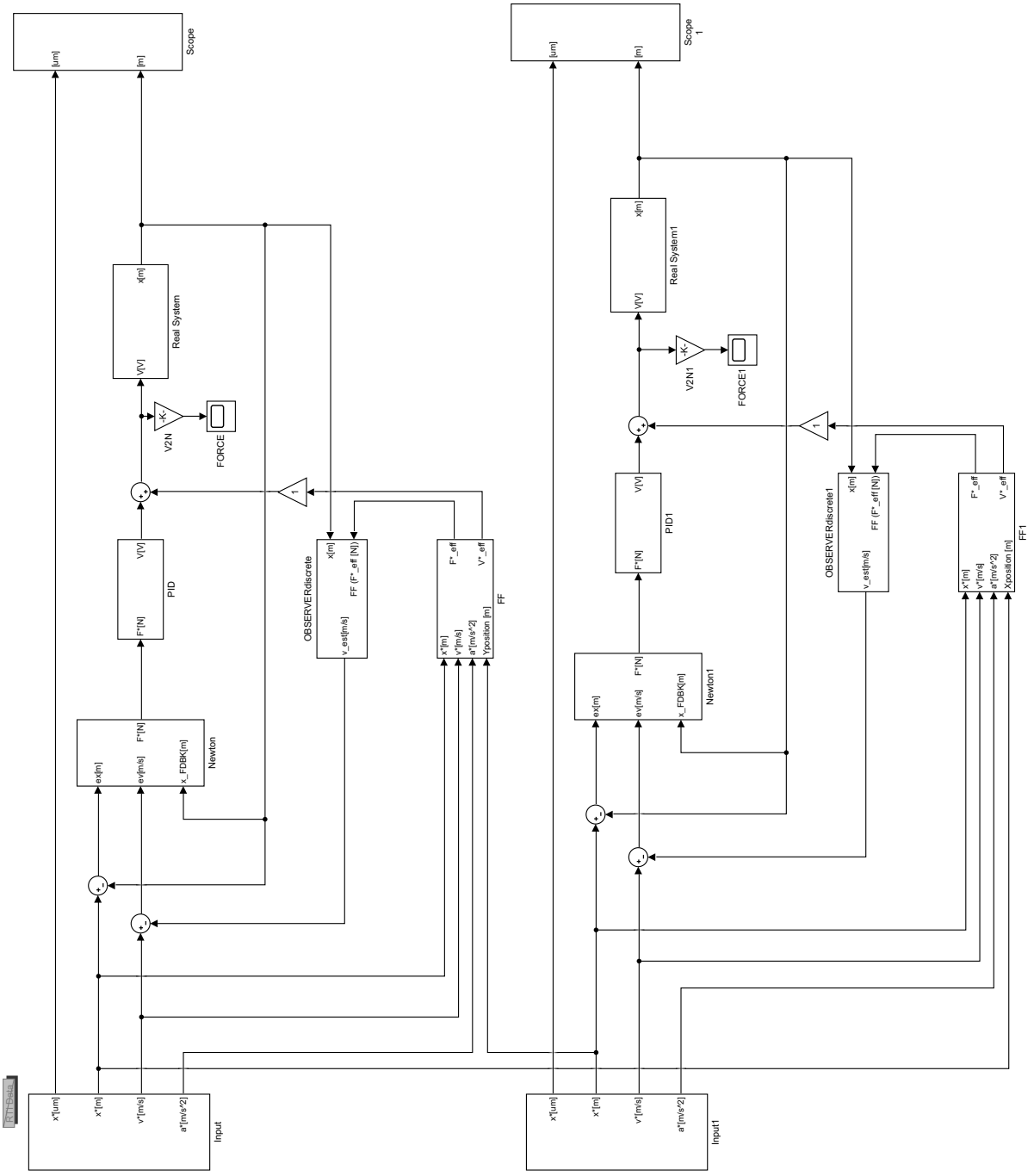

Figure 6.15: Two Axes Control Scheme in Simulink with Kinetostatic Cross-Coupling Compensation

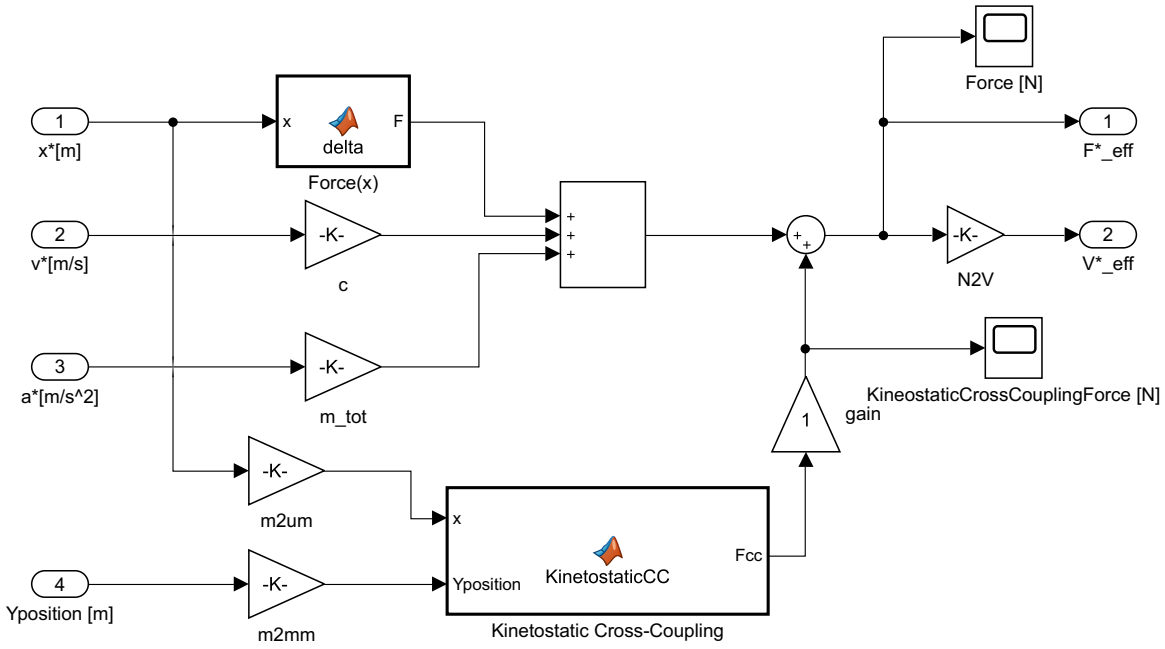

Figure 6.16: Kinetostatic Cross-Coupling Feed-Forward Simulink Block

µm and ±1000 µm when the Y-axis was held fixed at 0 µm, 500 µm and ±1000 µm. The same movements were performed also on the Y-axis when the X-axis was held in a fixed position.
For all the considered configurations, the following quantities where measured, with or without the application of the kinetostatic cross-coupling compensation: axis input force, total feed-forward force (as defined as the sum of the one axis feed-forward force and the compensation force), PID output force and the kinetostatic cross-coupling compensation force.
The data collected for the PID output force are reported in Tables 6.5 and 6.6, for the X-axis and Y-axis displacements, respectively.

As expected, when the perpendicular axis is not in a null fixed position and no compensation is implemented, the PID output force of the moving axis is greater than the force required when the perpendicular axis is in the null position. This is a consequence of the cross-coupling effect, according to which a greater input force is required to perform a given displacement. Without the compensation, the increase of the force required to perform a movement is not provided and therefore greater position and velocity errors are expecting, so increasing the feedback force. When the compensation is implemented, independently on the position of the perpendicular axis, the PID output force is close to the one measured when the perpendicular axis is at 0 µm. This means that the compensation works and it significantly reduces the kinetostatic cross-coupling effect. To support such a conclusion, the position error was measured with and without the

X-axis movement [µm]	Y-axis fixed position [µm]	Compensation	PID output force [N]
100	0	-	0.01
100	500	NO	0.09
100	500	YES	0.06
100	1000	NO	0.16
100	1000	YES	0.01
500	0	-	0.27
500	500	NO	0.52
500	500	YES	0.23
500	1000	NO	0.97
500	1000	YES	0.26
1000	0	-	1.52
1000	500	NO	2.08
1000	500	YES	1.30
1000	1000	NO	3.26
1000	1000	YES	1.68
1000	-1000	NO	2.63
1000	-1000	YES	1.59
-1000	0	-	-0.29
-1000	1000	NO	-1.73
-1000	1000	YES	-0.33
-1000	-1000	NO	-0.81
-1000	-1000	YES	-0.11

Table 6.5: Kinetostatic Cross-Coupling compensation. Effect on the PID output force. X-axis displacement, Y-axis fixed

Y-axis movement [μm]	X-axis fixed position [μm]	Compensation	PID output force [N]
100	0	-	0.20
100	500	NO	0.25
100	500	YES	0.18
100	1000	NO	0.36
100	1000	YES	0.21
500	0	-	0.71
500	500	NO	1.01
500	500	YES	0.70
500	1000	NO	1.50
500	1000	YES	0.85
1000	0	-	1.77
1000	500	NO	2.11
1000	500	YES	1.61
1000	1000	NO	3.12
1000	1000	YES	1.71
1000	-1000	NO	2.39
1000	-1000	YES	1.60
-1000	0	-	-2.50
-1000	1000	NO	-3.71
-1000	1000	YES	-2.42
-1000	-1000	NO	-3.26
-1000	-1000	YES	-2.69

Table 6.6: Kinetostatic Cross-Coupling compensation. Effect on the PID output force. Y-axis displacement, X-axis fixed

kinetostatic cross-coupling compensation. As an example, the result achieved when a 500 µm displacement on the X-axis was performed while the Y-axis was held fixed at 1000 µm, with and without the kinetostatic cross-coupling compensation, is shown in Figure 6.17.

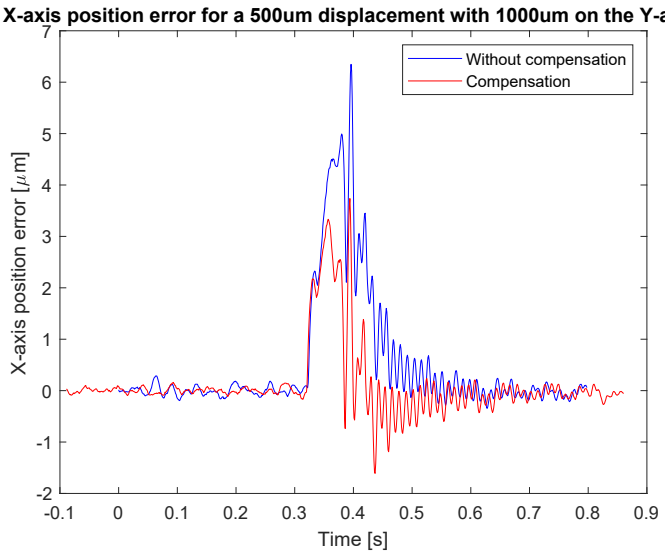

Figure 6.17: X-axis position error with and without kinematic cross-coupling compensation. 500 µm displacement on the X-axis, Y-axis constant at 1000 µm

As expected, the application of the compensation reduces the X-axis position error during the transient, thus reducing the involvement of the PID controller.

7

REPETITIVE CONTROL AND ITERATIVE LEARNING CONTROL

7.1 INTRODUCTION

When performing circular or square trajectories in the XY-plane, the system performance can be improved using high-performance controllers designed for periodic reference signals, such as RPC (Repetitive Control) or ILC (Iterative Learning Control). These controllers are added in parallel to the control scheme already implemented in the system and discussed in the previous chapters of this thesis. In this chapter, it will be explained how these high-performance controllers have been implemented using Matlab-Simulink and the background theory presented in Chapter 2. Both simulation and experimental results achieved will be discussed. The RPC implementation and results are presented in section 7.2, while the ILC implementation and results are presented in section 7.3. The RPC and ILC controllers have been added to the control scheme without cross-coupling compensation. Indeed, that compensation holds for static signals and it is useless when repetitive reference signals are applied.

7.2 REPETITIVE CONTROL (RPC)

As explained in Section 2.5, the RPC is an high-performance controller used with periodic or repetitive reference signals. It is added in parallel to the feedback controller (as shown in Figure 2.7). Therefore, in the Matlab-Simulink control scheme, the RPC block was added in parallel to the Newton and PID subsystems, as shown in Figure 7.1 for the two-axis system, where the Repetitive Control subsystem implements the RPC.

As explained in Section 2.5, the RPC algorithm is based on the system closed-loop transfer function, which needs to be known. In particular, the linear model of the system was used to implement the RPC on the compliant manipulator. The open loop transfer-function $G(s)$ in the Laplace domain is:

$$G(s) = \frac{X(s)}{V(s)} = \frac{K_f K_d}{m_{tot} s^2 + cs + k_t} \tag{7.1}$$

where:
- $X(s)$ is the axis position in the Laplace domain,
- $V(s)$ is the input voltage in the Laplace domain,

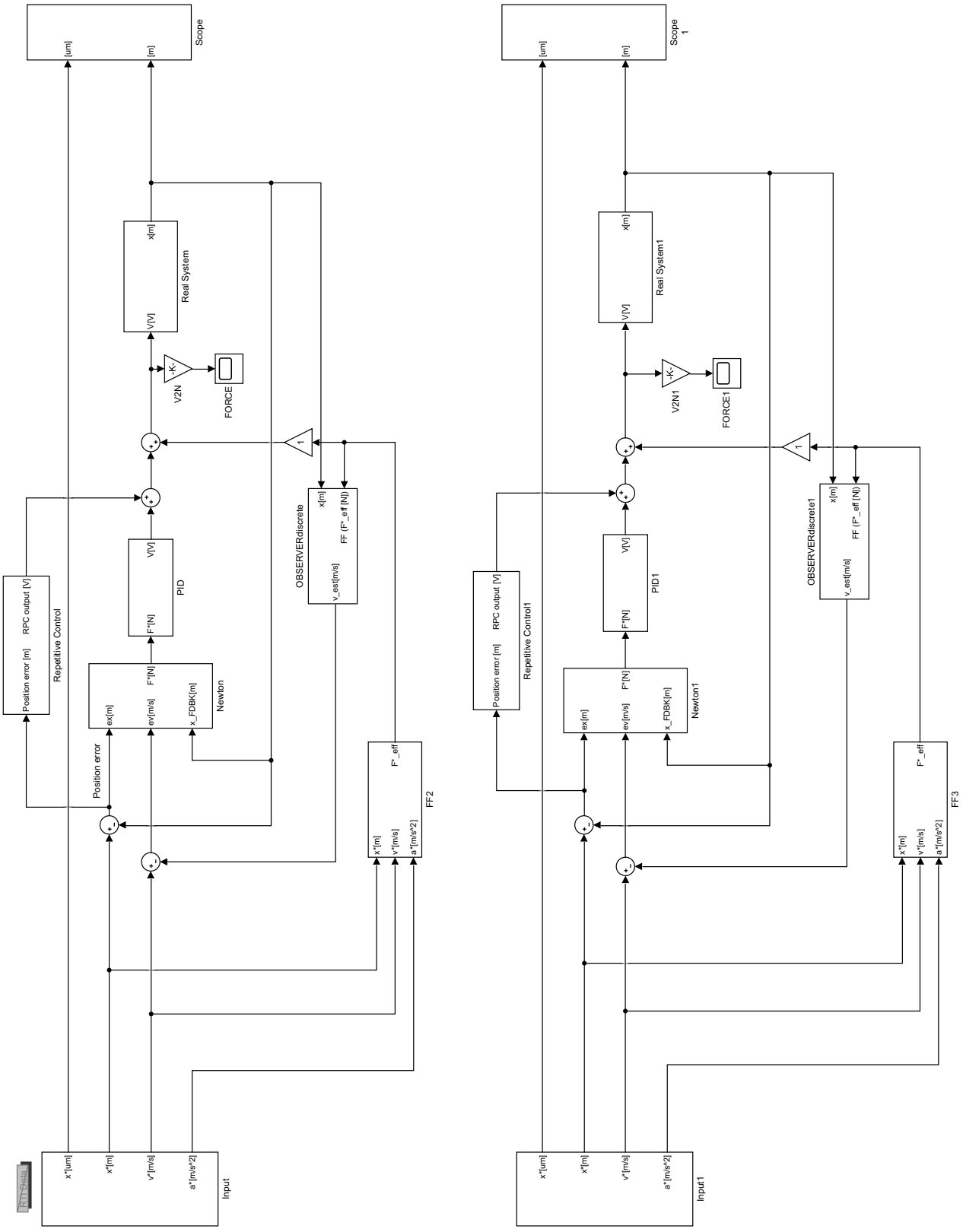

Figure 7.1: Two axes control scheme in Simulink with the RPC

- K_f is the voice coil actuator gain,
- K_d is the servo amplifier gain,
- m_{tot} is the axis total mass,
- c is the viscous damping coefficient
and
- k_t is the axis linear stiffness.
Thus, the close-loop transfer function is:

$$W(s) = \frac{G(s)}{1 + G(s)} = \frac{K_f K_d}{m_{tot} s^2 + cs + k_t + K_f K_d} \tag{7.2}$$

The RPC is implemented in the discrete domain, so that the closed-loop transfer function needs to be discretized. Moreover, the locations of the discrete function zeros need to be identified to check if the transfer-function can be reversed, so that the RPC can be implemented using Equation (2.25). If not the RPC has to be implemented with Equation (2.29). The zero of the discrete closed-loop transfer-function $W(z)$ for both system axes is located at -1, so that it is marginally stable. As a consequence, it was decided to consider that zero unstable and thus equation (2.29) has been used to implement the RPC. The resulting RPC structure $G_r(z)$ is:

$$G_r(z) = \frac{1}{1 - z^{-N}} K_r \frac{z^{-N+d+m} A(z^{-1}) z^{-m} B^+(z)}{b B^-(z^{-1})} \tag{7.3}$$

where:
- N is the number of samples in a period of the periodic signal,
- $\frac{1}{1-z^{-N}}$ is a common factor for all the repetitive controllers,
- K_r is the controller gain. To make the RPC controller stable, it was proved in Section 2.5 that the condition $0 < K_r < 2$ is required.
- d is the relative degree of the transfer-function, which, in this case, is equal to 1
- The zeros of the discrete time transfer function $W(z)$ were split in order to consider separately the stable zeros (related to $B^-(z)$, which in this case is equal to 1), and in the unstable zeros (related to $B^+(z)$, which in this case is equal to the whole discrete transfer-function numerator),
- m is the number of unstable zeros, which, in this case, is equal to 1,
- z^{-N+d+m} is necessary for physical feasibility,
- $A(z^{-1})$ is the denominator polynomial of $W(z)$
- $b \geqslant max[B^+(e^{j\omega T})]^2$ with $0 \leqslant \omega T \leqslant \pi$,
- $N \geqslant d + m$ for the controller physical feasibility,
- $B^+(z)$ is equal to $B^+(z^{-1})$, where z^{-1} is substituted with z: $B^+(z)$ is not physically feasible, but $z^{-m}B^+(z)$ is physically feasible.
The Simulink RPC controller subsystem, implemented with the structure reported in Equation (7.3), is shown in Figure 7.2. A clock is also added to switch off the RPC action after an appropriate time. This

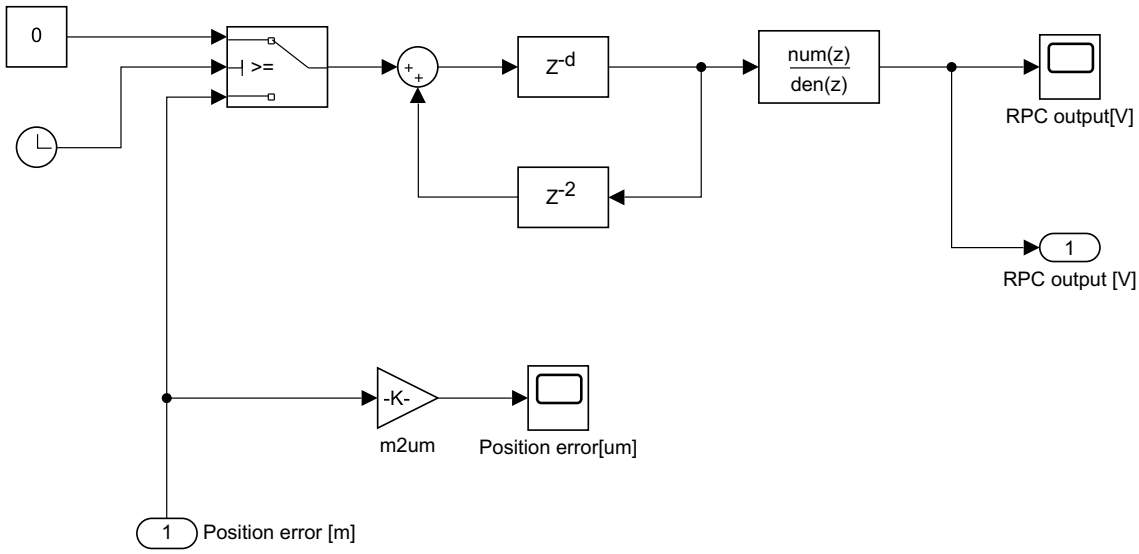

Figure 7.2: Simulink RPC Block

The Matlab code used to evaluate the discrete transfer-function and to produce all the numerical parameters needed in the RPC implementation is reported in A.10. To run the Simulink model with the implemented RPC controller, it is first necessary to run this Matlab script. To achieve the best performance, the value of the K_r gain used in the Matlab script was experimentally tuned. The higher is this gain, the faster is the compensation action. However, a higher gain can also lead to a system that will diverge faster, perhaps it do not reach the minimum position error possible. It follows that the tuning of K_r is the result of a trade-off between the controller speed and the position error reduction. It is also important to ensure that $0 < K_r < 2$ to ensure system stability.
The system performance improvement due to the RPC controller was verified using both simulation and experimental results. The results related to the sinusoidal reference signals are reported in Section 7.2.1, those achieved using the triangular reference are reported in Section 7.2.2 and finally the results achieved using the trapezoidal reference signals are reported in Section 7.2.3. Most of the reported results are related to the real system, while only few significant simulation results are shown.

7.2.1 *Sinusoidal Reference Signal*

To improve the system performance in drawing a circumference in the XY-plane the RPC was implemented with a sinusoidal reference signals on both axes. Simulations and experiments were performed considering sinusoidal reference signals with different amplitudes and frequencies.

7.2.1.1 *Simulations*

The simulation time plots are reported only for one axis because the obtained results for the two axes are very similar. Indeed the related models differ only by the servo amplifier gain. The results achieved for the position error with a sinusoidal reference signal of amplitude 1000 µm and 10 Hz frequency are shown in Figure 7.3. These simulations were performed using the system non-linear model explained in Section 3.9. The results achieved without adding an external random noise to the system input are shown in the plot on the left, while those obtained when external noise is added are shown in the plot on the right in order to better reproduce the real system behaviour. Both plots show the position error signal returned by the simulation performed in different situations: without the RPC action, with continuous RPC action (thus showing the divergence of the position error after a certain time), and with RPC action interrupted after a suitable time.

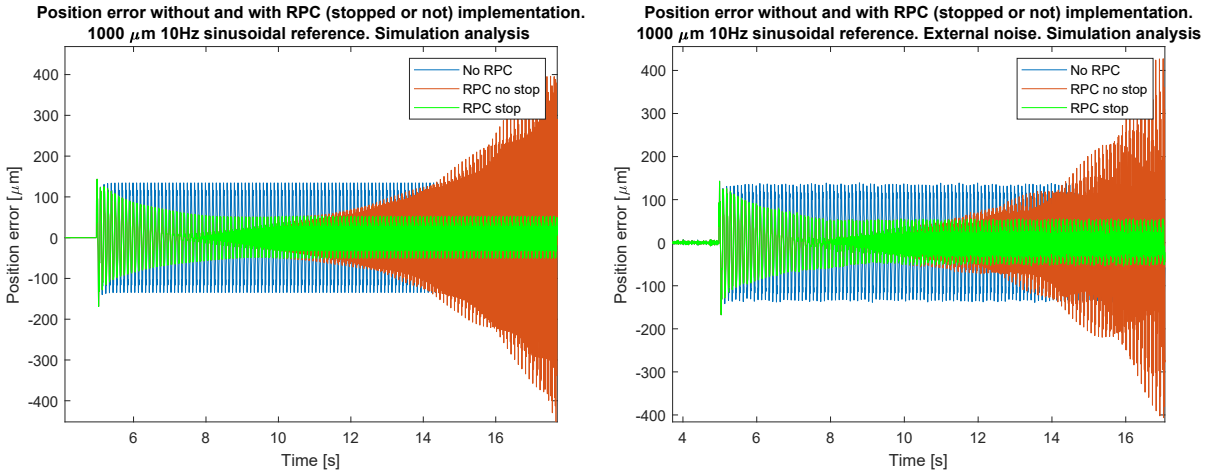

Figure 7.3: Simulation results for the position error without and with the RPC action (continuous or stopped after a suitable time). 1000 µm, 10 Hz sinusoidal wave reference signal. Non-linear model, without and with external noise.

As can be seen from the figures, when the RPC was implemented the position error diverges both without, and with,the external noise added to the system input. Moreover, in both cases it is clear that, if the RPC is interrupted at an appropriate time, the position error is

significantly reduced so that the improvement obtained with the RPC action is clear.
The theory of the RPC does not explain the divergent behaviour of the system. On the contrary, the position error is expected to be null after a certain time when the RPC is implemented if no external noise is superimposed to the system input. The behaviour showed by simulations (and confirmed by experimental results) probably happens because the RPC design is based on the linear model of the system, while a non-linear model was used for simulating the real system. To verify this hypothesis, further simulations using the same reference signal, but considering the linear model instead of the non-linear one, were performed. The obtained results are shown in Figure 7.4.

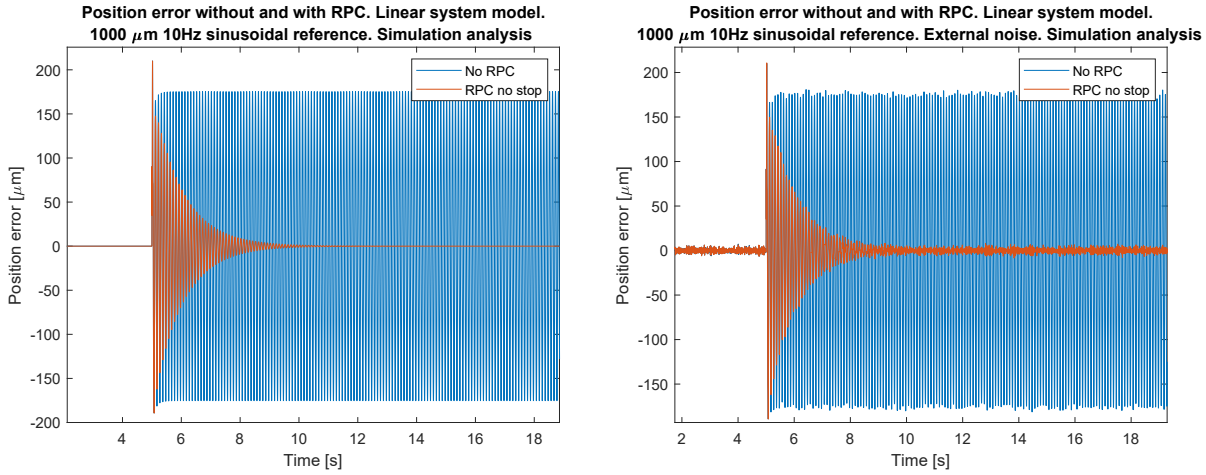

Figure 7.4: Simulation results for the position error without and with the RPC action. 1000 μm, 10 Hz sinusoidal wave reference signal. Linear model, without and with external noise.

As expected, when the RPC is implemented and no noise is added, after an initial transient the position error becomes null. Moreover, when the external random noise is added, the position error amplitude is similar to that of the external noise, which can not be eliminate by the RPC because it is not a periodic or repetitive signal.
Thus, it is reasonable to conclude that the divergent behaviour shown by simulation results when using the non-linear model, occurs because the RPC is based on a linear model assumption. However, the RPC action is useful also under such simplifying condition if it is stopped at an appropriate time that can be determined experimentally.

7.2.1.2 *Experiments*

Because the real system is non-linear, it is expected that it exhibits a divergent behaviour on the position error when the RPC is used, as happened in the simulation with the non-linear system. However, if the RPC action is stopped after an appropriate time, the system per-

formance is expected to be improved.
The amplitudes chosen for the sinusoidal reference signals on both axes are: 100 µm and 500 µm, while the frequencies are: 1 Hz, 5 Hz and 10 Hz. For the smaller amplitude selected (100 µm) the frequency of the sinusoidal reference was also increased to 20 Hz and 50Hz. The available power supply did not allow the system to be driven at these frequencies when the sinusoidal reference amplitude was 500 µm. Some examples of position error measurements, without and with the RPC action (continuous or interrupted), are shown in Figure 7.5. The figure on the left represents the X-axis position error signal with 100 µm amplitude and a 10 Hz frequency sinusoidal reference signal, while the plot on the right represent the Y-axis position error with 500 µm amplitude and a 10 Hz frequency sinusoidal reference signal.

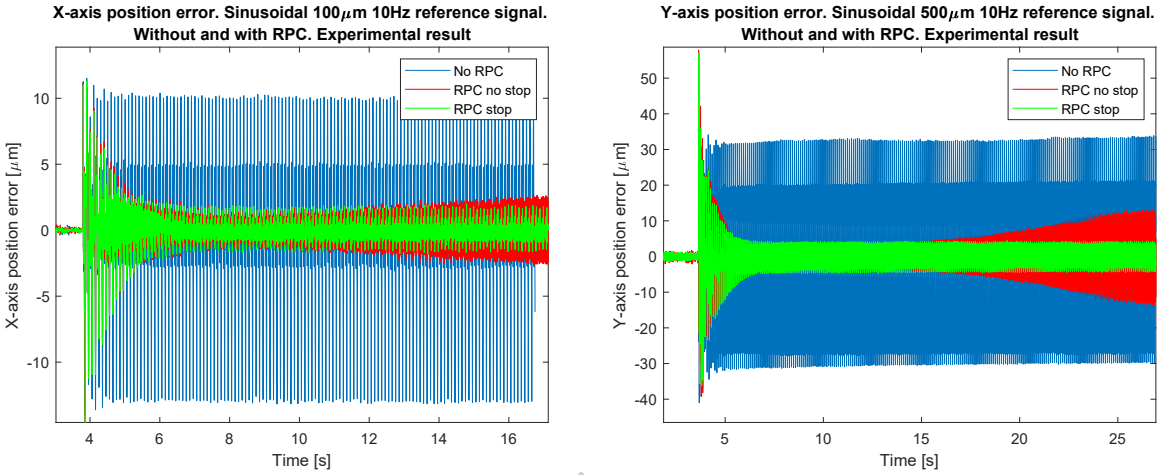

Figure 7.5: Experimental results for the position error without and with the RPC action (continuous or stopped after a suitable time). X-axis example on the left, Y-axis example on the right.

As it can be seen from Figure 7.5, the behaviour of experimental results and simulation results obtained with the non-linear model are equivalent. When the RPC is used, the position error is reduced, but if it is not interrupted at the appropriate time the position error tends to diverge. However, if the RPC action is stopped, the position error reduction remains.
In Figure 7.6 the position errors measured, without the RPC action and with the RPC action interrupted at the appropriate time, when feeding both axes with a 100 µm amplitude and 50 Hz frequency sinusoidal reference signal are shown.

As it can be seen, the position error without the RPC is very high (about 90 µm), that it is almost equal to the reference signal amplitude (100 µm). Conversely, when the RPC is applied, the position error amplitude greatly decreases, thus significantly improving the system performance. The steady-state plots on the XY-plane related to the

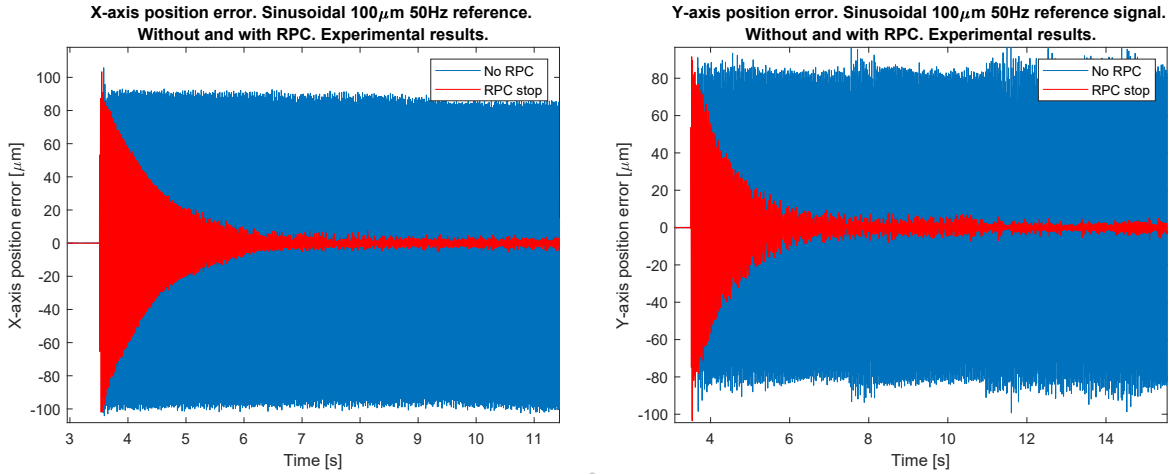

Figure 7.6: Experimental result for the position error without and with the RPC action. Sinusoidal wave reference signal 100 µm 50 Hz on both axes.

same experiment, without and with the RPC action, are shown in Figure 7.7.

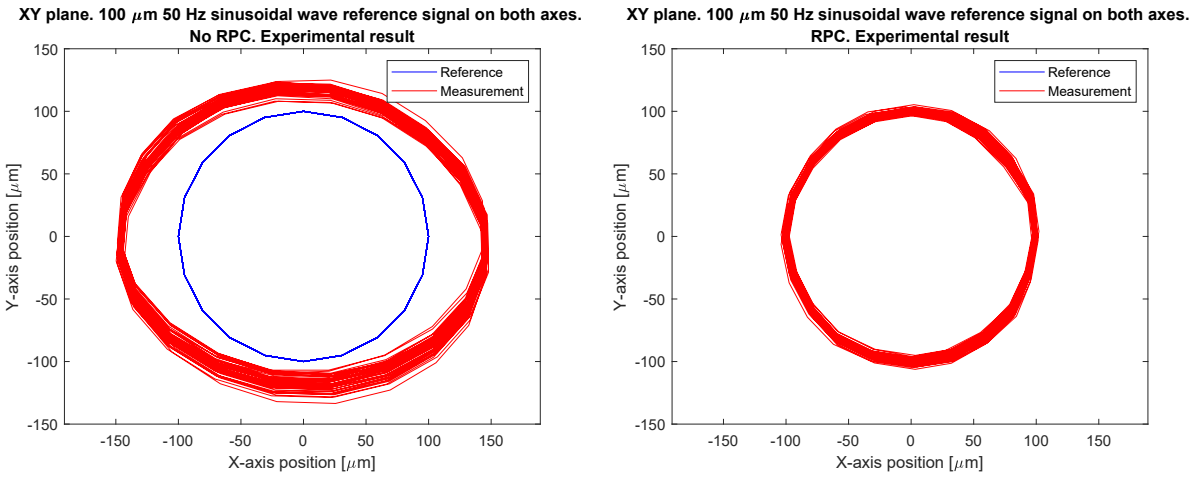

Figure 7.7: Experimental plots of the XY-plane with sinusoidal wave reference signal of 100 µm amplitude and 50 Hz frequency on both axes. Without RPC action (left plots) and with the RPC action interrupted at the appropriate time (right plots).

Moreover, the steady-state XY-plane plots obtained, without and with the RPC action, when feeding both axes with a 500 µm amplitude, and 1 Hz and 10 Hz frequency sinusoidal reference signals on both axes are shown in Figure 7.8 and 7.9, respectively.

The RMS values of the position error, without and with the RPC action, are reported in Tables 7.1 and 7.2 for 100 µm amplitude sinusoidal wave reference signals for the X-axis and the Y-axis respectively. Moreover, the RMS values of the position error, without and with the RPC action, are reported in Tables 7.3 and 7.4 for the sinusoidal ref-

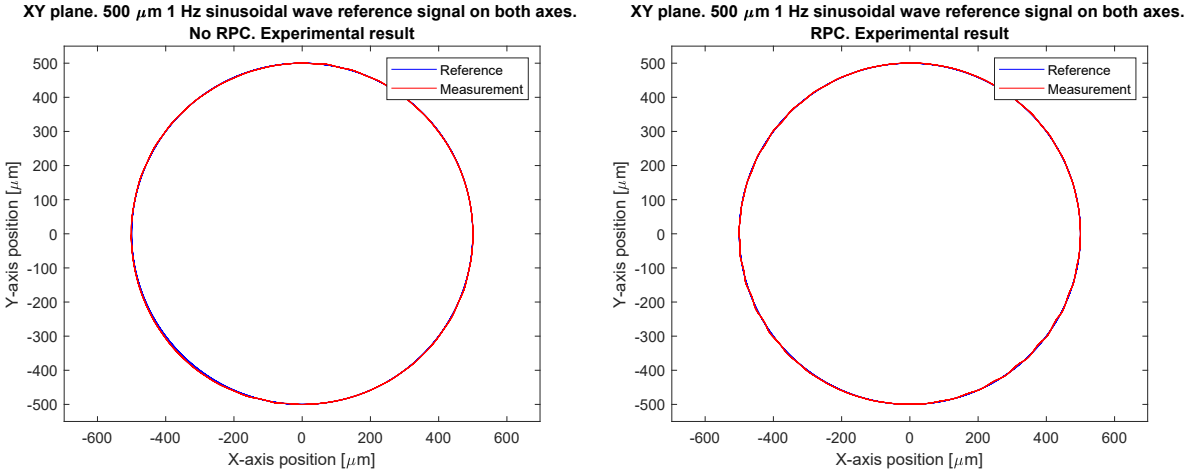

Figure 7.8: Experimental plots of the XY-plane with sinusoidal wave reference signal of 500 μm amplitude and 1 Hz frequency on both axes. Without RPC action (left plots) and with the RPC action interrupted at the appropriate time (right plots).

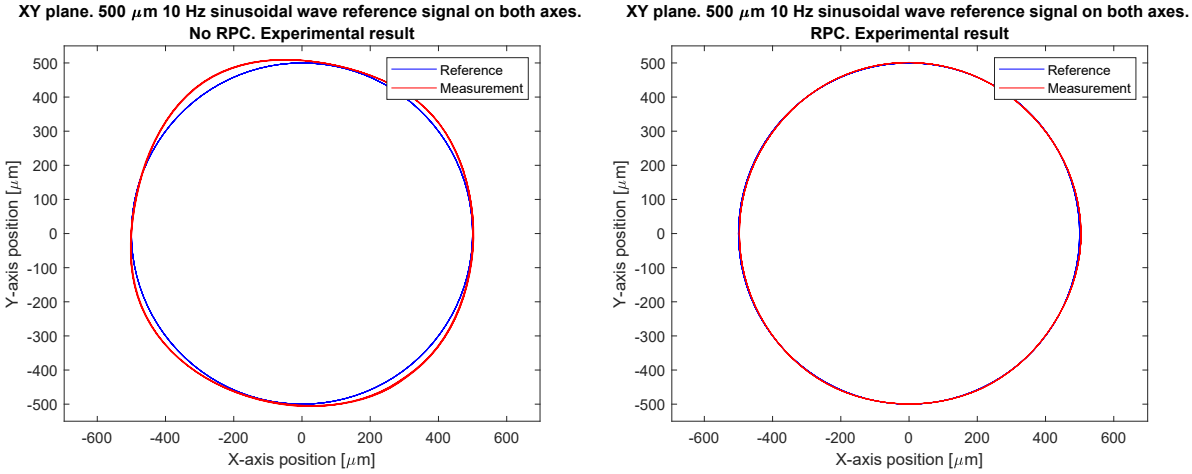

Figure 7.9: Experimental plots of the XY-plane with sinusoidal wave reference signal of 500 μm amplitude and 10 Hz frequency on both axes. Without RPC action (left plots) and with the RPC action interrupted at the appropriate time (right plots).

erence signal with 500 µm amplitude for the X-axis and the Y-axis, respectively.

Frequency [Hz]	1	1	5	5	10	10	20	20	50	50
RPC	No	Yes	No	Yes	No	Yes	No	Yes	No	Yes
RMSE [µm]	1.84	1.19	3.61	0.74	5.41	0.55	6.45	2.98	78.87	1.57

Table 7.1: RMS position error value without and with RPC action when feeding the X-axis sinusoidal reference signal of 100 µm amplitude.

Frequency [Hz]	1	1	5	5	10	10	20	20	50	50
RPC	No	Yes	No	Yes	No	Yes	No	Yes	No	Yes
RMSE [µm]	1.57	1.46	3.81	2.66	7.71	1.78	11.39	2.28	57.82	2.43

Table 7.2: RMS position error value without and with RPC action when feeding the Y-axis sinusoidal reference signal of 100 µm amplitude.

Frequency [Hz]	1	1	5	5	10	10
RPC	No	Yes	No	Yes	No	Yes
RMSE [µm]	2.50	1.46	8.20	0.29	16.69	1.54

Table 7.3: RMS position error value without and with RPC action when feeding the X-axis sinusoidal reference signal of 500 µm amplitude.

As it can be seen from Figure 7.7, 7.8 and 7.9 and from the data in Tables 7.1 - 7.4, the RPC improves the system performance in all the chosen configurations. However, the improvement is more significant at higher frequencies. This is probably due to a higher position error without the RPC, so the RPC action is more evident. At the lowest frequency chosen (1 Hz), the system provides good performance also when the RPC is not used and thus, the improvement achieved with the RPC action is smaller.

7.2.2 *Triangular Reference Signal*

To improve the system performance when drawing a square in the XY-plane, the RPC was implemented also when feeding both axes with a triangular reference signal.

7.2.2.1 *Simulations*

As for the sinusoidal reference signal, the simulations were performed using a triangular reference signal with 1000 µm amplitude and 10 Hz frequency. The position error results using the system non-linear model, without and with the RPC action, are shown in Figure 7.10. The results achieved without adding an external random noise to

Frequency [Hz]	1	1	5	5	10	10
RPC	No	Yes	No	Yes	No	Yes
RMSE [µm]	1.74	1.34	6.95	3.52	19.88	1.39

Table 7.4: RMS position error value without and with RPC action when feeding the Y-axis sinusoidal reference signal of 500 µm amplitude.

the system input are shown in the plot on the left, while the results achieved when the external noise is added are shown in the plot on the right in order to better reproduce the real system behaviour. Simulations show that, to avoid a divergent behaviour of the position error, the RPC action needs to be interrupted also when the triangular reference signal is used.

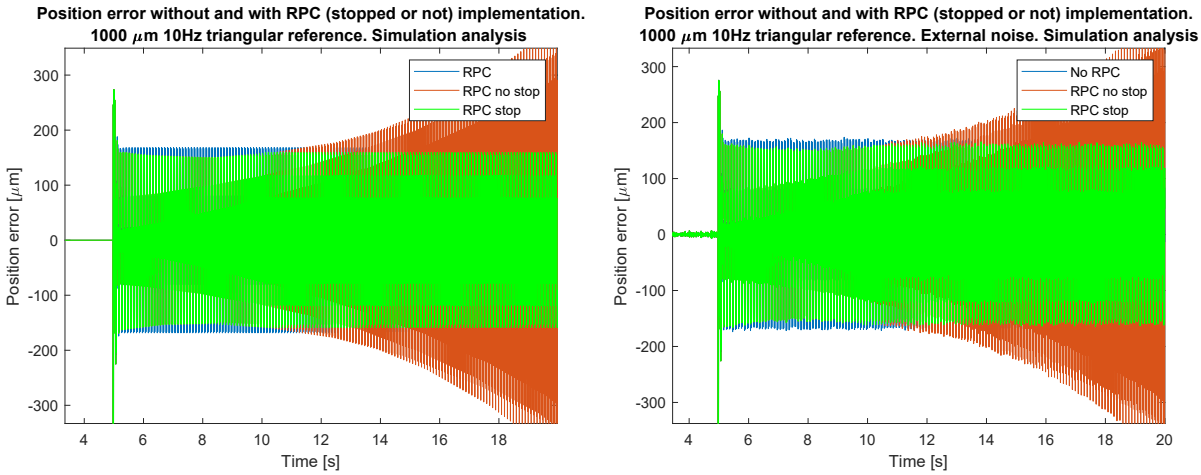

Figure 7.10: Simulation results for the position Error without and with RPC action (continuous or stopped after a suitable time). 1000 µm, 10 Hz triangular wave reference signal. Non-Linear Model, without and with external noise.

Compared to the improvement achieved in the simulation of the sinusoidal reference signal, the figures show that the positive impact of the RPC action on the reduction of the position error amplitude is significantly lower with the triangular reference signal. Moreover, simulation using the linear system model showed that the RPC action is theoretically capable of nullifying the position error and that the divergent behaviour is due to the system non-linearity and to the fact that the RPC was implemented based on the assumption of a linear transfer-function. The obtained results are shown in Figure 7.11. Thus the same conclusions as for the sinusoidal reference signal can be drawn.

7.2.2.2 *Experiments*

Different experimental analyses were performed also with the triangular reference signal. The signal amplitudes chosen for both axes

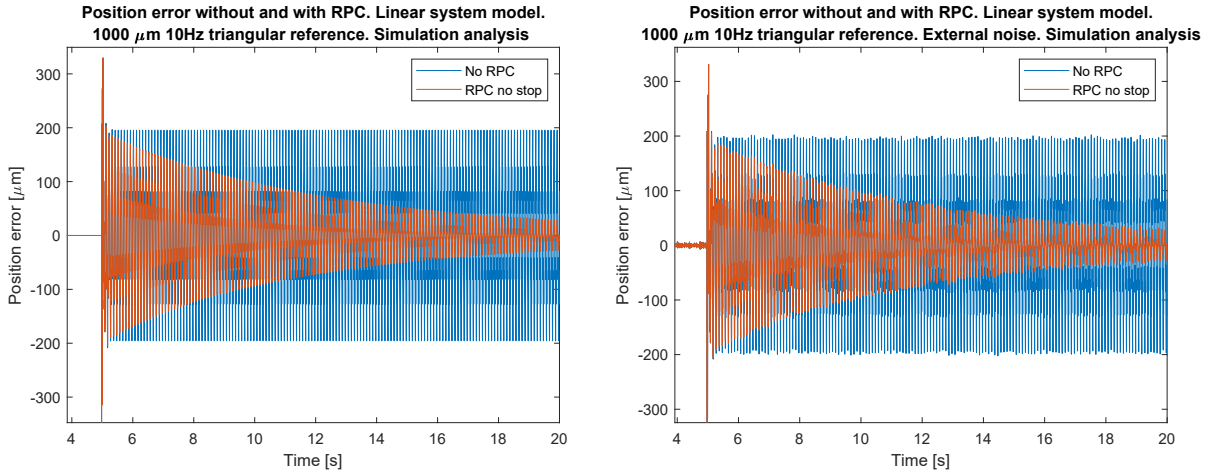

Figure 7.11: Simulation results for the position error without and with RPC action. 1000 μm, 10 Hz triangular wave reference signal. Linear model, without and with external noise.

were: 100 μm and 500 μm, while the frequencies used were: 1 Hz, 5 Hz and 10 Hz. Only for the smallest amplitude selected (100 μm) the frequency of the triangular reference signal was increased to 20 Hz and 50 Hz. As with the sinusoidal reference signal, the power supply was not able to drive the system at these frequencies when the amplitude is 500 μm.

As happened during the simulation analysis, the experimental results also show a divergence of the position error after some periods of the triangular signal when the RPC is used. However, also in this case, if the RPC action is stopped at the appropriate time, it allows the reduction of the position error amplitude and it does not diverge. Therefore the system performances are improved. Two examples of the position errors measured, without the RPC action and with the RPC action stopped at the appropriate time, are shown in Figure 7.12. The plot on the left is related to the X-axis position error signal with a 500 μm amplitude and of 10 Hz frequency triangular reference signal, while the figure on the right shows the Y-axis position error measured with a 100 μm amplitude and 10 Hz frequency triangular reference signal.

The results reported in Figure 7.12 show that the RPC action significantly improved the system performance also when the triangular reference signal is used. Moreover, improvement shown by measurement is more relevant than that achieved in simulations.

In Figure 7.13, position errors measured, without and with the RPC action, with 100 μm amplitude and 50 Hz frequency triangular reference signal on both axes are shown. The improvement provided by the RPC is evident also in these situations. The XY-plane plots obtained, without and with the RPC action, when feeding both axes with a triangular reference signal are shown in Figure 7.15 and Fig-

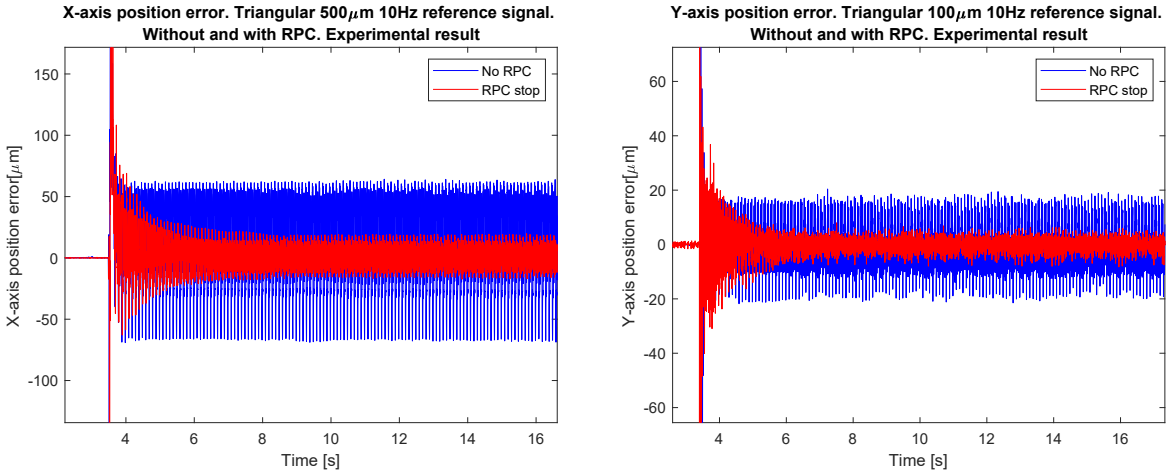

Figure 7.12: Experimental results for the position Error without and with RPC action stopped after a suitable time. X-axis example on the left, Y-axis example on the right.

ure 7.14. The first one is for 500 μm amplitude and 10 Hz frequency, while the second one is for 100 μm amplitude and 50 Hz frequency.

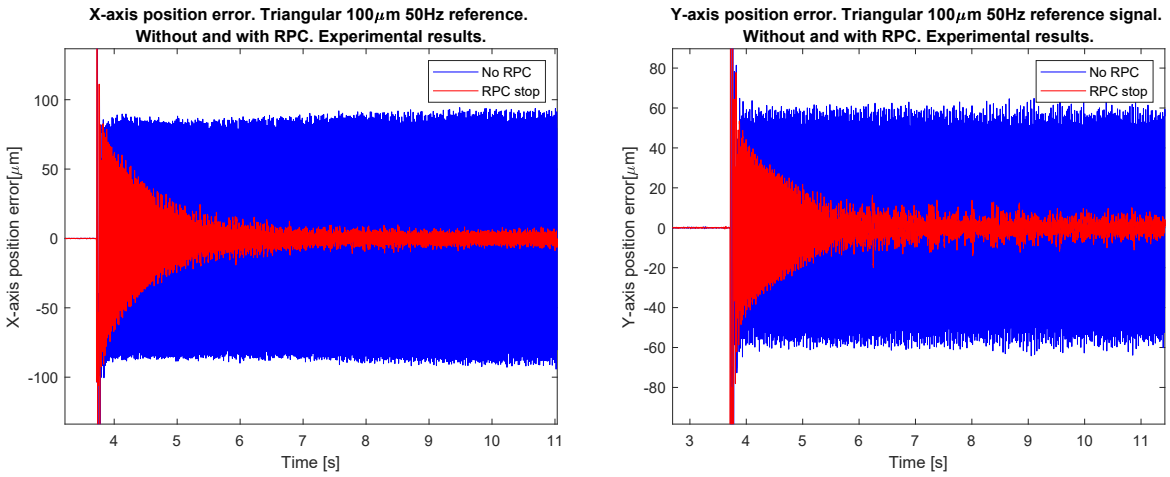

Figure 7.13: Experimental results for the position error without and with RPC action. Triangular wave reference signal 100 μm 50 Hz on both axes.

The RMS values of the position error obtained without and with the RPC action, are reported in Tables 7.5 and 7.6 for the triangular reference signal with 100 μm amplitude. Moreover, the RMS values of the position error, without and with the RPC action are reported in Tables 7.7 and 7.8 for the triangular reference signal with 500 μm amplitude.

As it can be seen from Tables 7.5 and 7.6 when the amplitude of the reference signal is 100 μm the RPC does not improve the system performance at the lower frequencies selected (1 Hz and 5 Hz), but conversely it disimproves them. However, at 10 Hz or above, the RPC

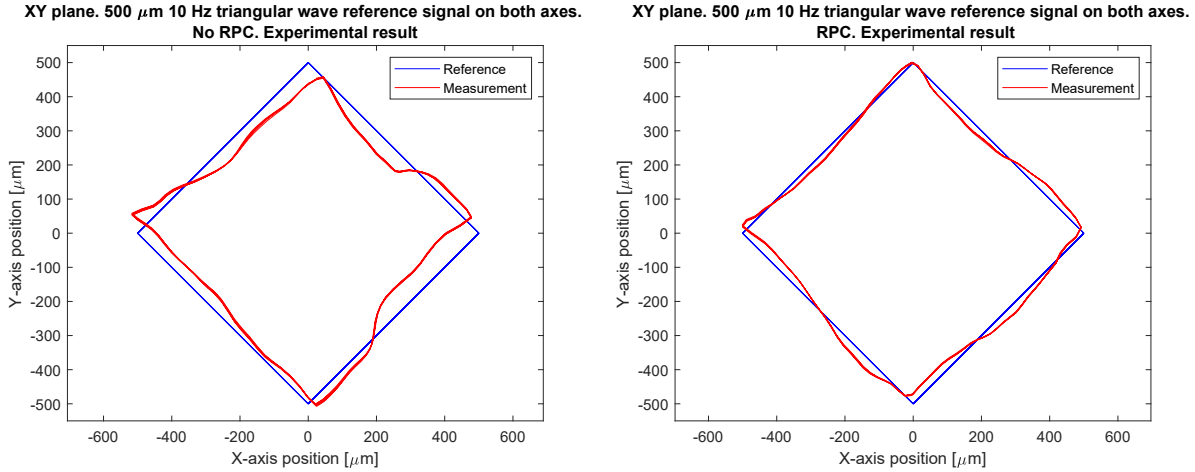

Figure 7.14: Experimental plots of the XY-plane with triangular wave reference signal 500 μm amplitude and 10 Hz frequency on both axes. Without RPC action (left plot) and with RPC action interrupted at the appropriate time (right plot).

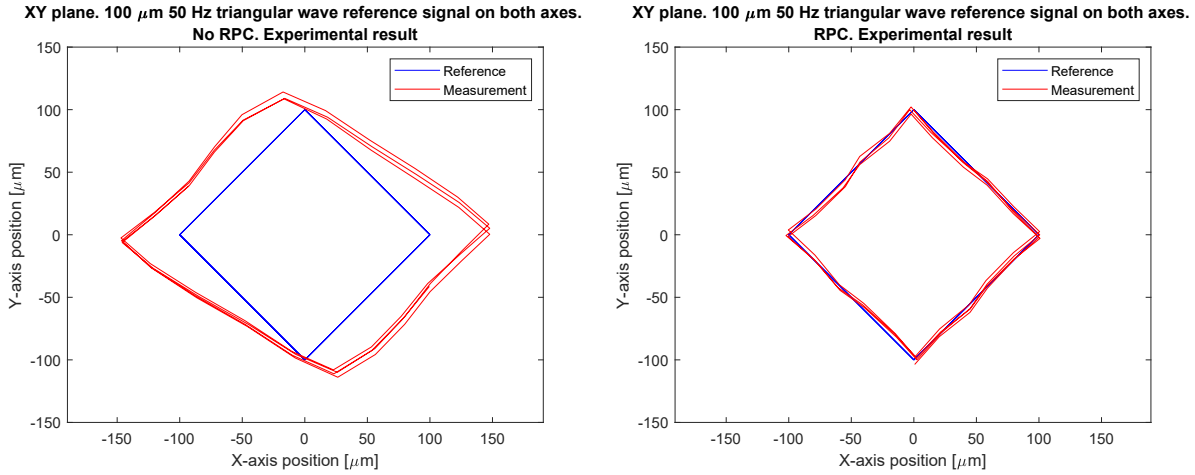

Figure 7.15: Experimental plots of the XY-plane with triangular wave reference signal 100 μm amplitude and 50 Hz frequency on both axes. Without RPC action (left plot) and with RPC action interrupted at the appropriate time (right plot).

Frequency [Hz]	1	1	5	5	10	10	20	20	50	50
RPC	No	Yes	No	Yes	No	Yes	No	Yes	No	Yes
RMSE [μm]	1.90	2.90	3.82	4.35	6.04	2.50	9.21	3.01	64.78	2.97

Table 7.5: RMS position error value without and with RPC action when feeding the X-axis triangular reference signal of 100 μm amplitude.

Frequency [Hz]	1	1	5	5	10	10	20	20	50	50
RPC	No	Yes	No	Yes	No	Yes	No	Yes	No	Yes
RMSE [μm]	1.58	3.10	3.99	3.47	8.43	2.41	13.73	5.25	44.71	3.75

Table 7.6: RMS position error value without and with RPC action when feeding the Y-axis triangular reference signal of 100 μm amplitude.

Frequency [Hz]	1	1	5	5	10	10
RPC	No	Yes	No	Yes	No	Yes
RMSE [μm]	25.72	12.38	12.30	3.13	35.99	8.86

Table 7.7: RMS position error value without and with RPC action when feeding the X-axis triangular reference signal of 500 μm amplitude.

significantly reduces the amplitude of the position error. When the amplitude is 500 μm, the position error is always reduced when the RPC is applied, as shown in Tables 7.7 and 7.8. Therefore, it can be concluded that, when a triangular wave reference signal is applied, the RPC always improves the system performance at the higher frequencies selected, while at lower frequencies its action is beneficial only if the signal amplitude is at least about 500 μm.

7.2.3 *Smooth Trapezoidal Reference Signal*

The RPC was applied also when a smooth trapezoidal reference signal is applied to both axes. Some simulation and experimental results are reported in this section.

7.2.3.1 *Simulations*

As done with the sinusoidal and the triangular reference signals, some meaningful simulations were performed using also a trapezoidal reference signal with 1000 μm amplitude and 1 Hz frequency. The position error results obtained using the system non-linear model, without and with the RPC action, are shown in Figure 7.16. The results achieved without the addiction of an external random noise to the system input are shown in the plot on the left, while the results achieved when the external noise is added are shown in the plot on the right, in order to better reproduce the real system behaviour.

Frequency [Hz]	1	1	5	5	10	10
RPC	No	Yes	No	Yes	No	Yes
RMSE [μm]	39.18	35.58	34.48	10.97	44.72	29.90

Table 7.8: RMS position error value without and with RPC action when feeding the Y-axis triangular reference signal of 500 μm amplitude.

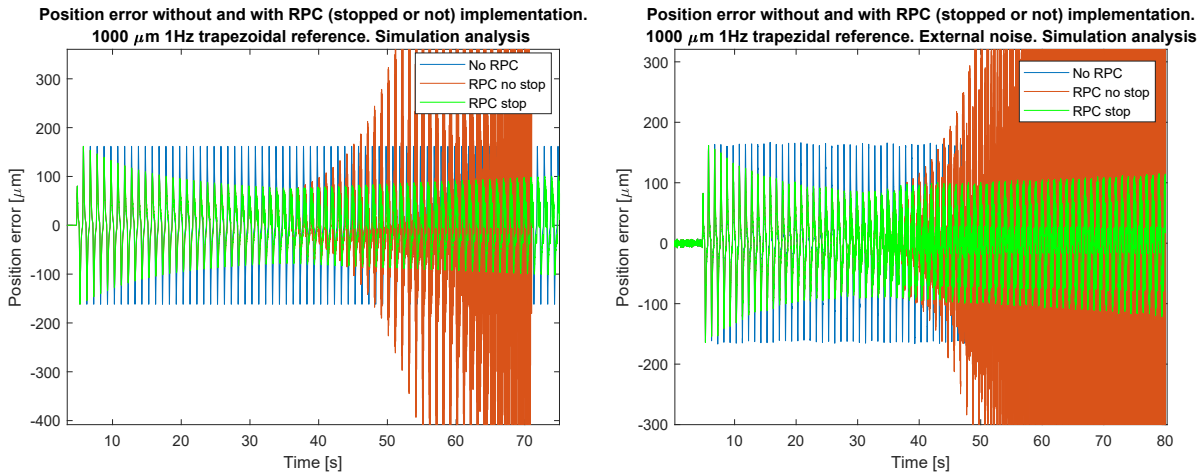

Figure 7.16: Simulation results for the position error without and with RPC (continuous or stopped after a suitable time). 1000 μm, 1 Hz trapezoidal wave reference signal. Non-linear model, without and with external noise.

As happened with the sinusoidal and the triangular reference signals, simulations show that the position error exhibits a divergent behaviour when the RPC action is applied. To avoid this undesirable behaviour, the RPC action was interrupted at an appropriate time when a sinusoidal or a triangular reference signals are applied. On the contrary, when the trapezoidal reference signal is used, simulations show that the position error increases even if the RPC action is stopped, even if the error amplitude increasing rate decreases when the RPC action is interrupted. However, since this behaviour is not acceptable, the use of the RPC should be avoided with trapezoidal reference signals.
For the sinusoidal and the triangular reference signals, it was concluded that the position error divergent behaviour is due to the system non-linearity and to the fact that the RPC was implemented based on the linear transfer-function. To test if the same hypothesis holds also with the trapezoidal reference signal some simulations were performed using the system linear model. The obtained results, without (left plot) and with (right plot) the addition of the external random noise to the system input, are shown in Figure 7.17. That figure confirms that the divergent behaviour of the position error is due to the the system non-linearity also for the trapezoidal reference signal.

7.2.3.2 *Experiments*

Being the system non-linear, simulations suggest that the position error exhibits a divergent behaviour when the RPC is used, even if its action is interrupted at the appropriate time.
The amplitudes chosen for the smooth trapezoidal reference signals

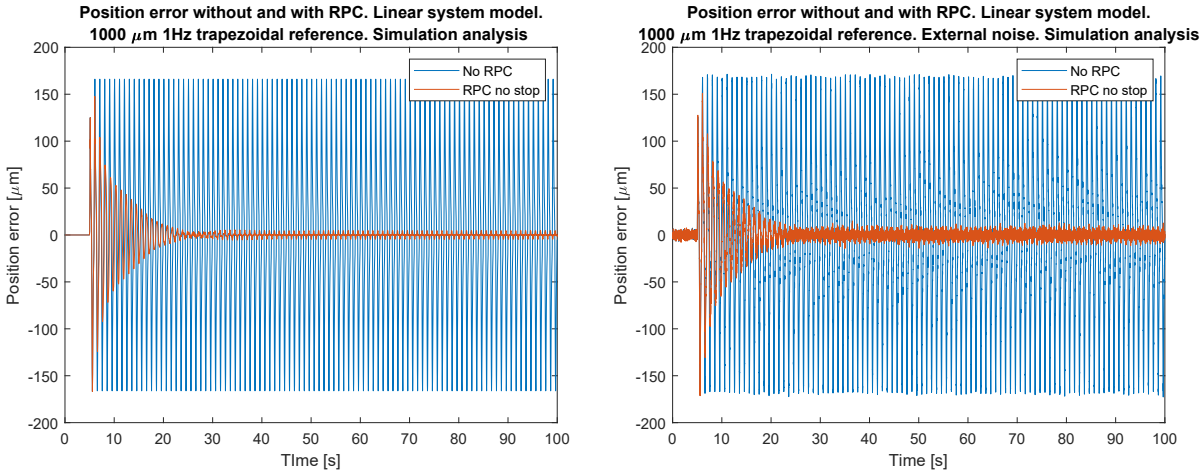

Figure 7.17: Simulation results for the position error without and with RPC. 1000 µm, 1 Hz trapezoidal wave reference signal. Linear model, without and with external noise.

on both axes were: 100 µm and 500 µm, while the frequency was firstly set at 1 Hz. The results achieved with 500 µm amplitude, without and with the RPC action (continuous or interrupted) are shown in Figure 7.18.

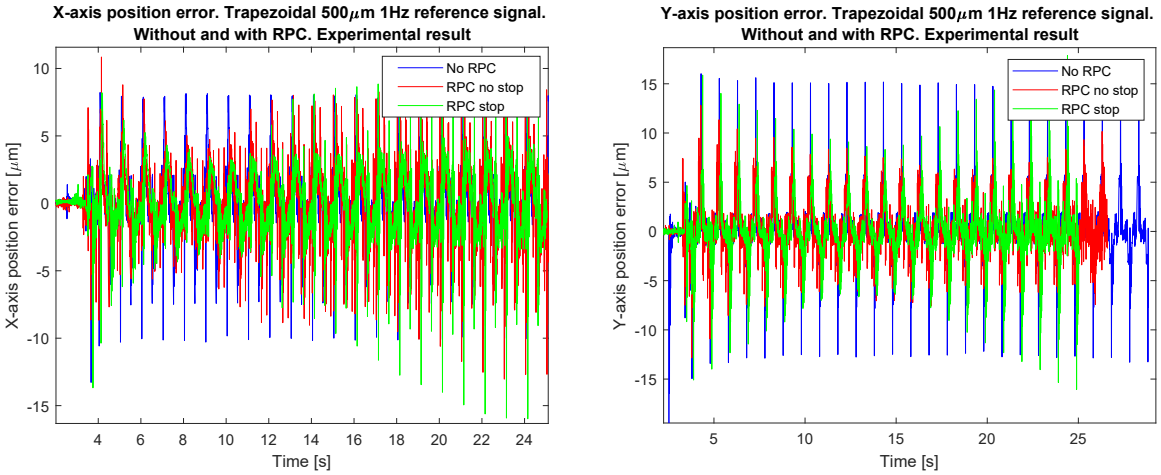

Figure 7.18: Experimental results for the position error without and with RPC action (continuous or stopped after a suitable time). Trapezoidal wave reference signal 500 µm 1 Hz on both axes.

As shown in Figure 7.18, the behaviour of the experimental results and the simulation results obtained using the non-linear model coincide: the position error start to decrease, but it diverges after a certain time independently of the RPC action interruption. Unlike simulations, in the experimental results the increasing rate of the position error is faster when the RPC action is stopped compared to when it is not stopped.
Since this undesirable behaviour was present both in simulations and

experiments performed at 1 Hz, experiments at higher frequencies were not performed to avoid movements that could have broken the system.
Since the "ramp" of the smooth trapezoidal reference signal was built using a half period of a sinusoidal wave, by removing the signal constant segments, a sinewave is obtained with a frequency of twice the trapezoidal signal frequency. It was verified that the RPC works properly with the sinusoidal reference signal. Hence it can be reasonably concluded that the undesirable behaviour of the RPC when the smooth trapezoidal reference signal is used can be related to the presence of its constant segments.
In conclusion, RPC can greatly improve the system performance when drawing circular trajectories in the XY-plane. To avoid the divergent behaviour of the position error, the RPC action needs to be interrupted after a suitable time that is determined experimentally. Moreover, to perform a square trajectory in the XY-plane two reference signals can be used: the triangular or the smooth trapezoidal reference signals. Both simulations and experiments show that without the RPC action the smooth trapezoidal reference signal allows the achievement of better performance than the triangular one due to the continuity of the signal derivative. Unfortunately, the RPC action does not work properly with this reference signal because the position error diverges even if the RPC action is interrupted at the optimum time. Conversely, the RPC action improves the system performance when the triangular reference signal is used, particularly at the higher frequencies analyzed. Therefore, the best solution to the drawing of a square trajectory in the XY-plane is the trapezoidal reference signal without the RPC action when the frequency is low and using the triangular reference signal with the RPC interrupted at the suitable time at higher frequencies.

7.3 ITERATIVE LEARNING CONTROL (ILC)

As explained in Section 2.6, the ILC is a high-performance controller that can be applied with periodic or repetitive reference signals. It is added in parallel to the feedback controller (as shown in Figure 2.8). Therefore, in the Matlab-Simulink control scheme, the ILC block is added in parallel to the Newton and PID subsystems, as shown in Figure 7.19 for the two-axis system. In that figure, the Iterative Learning Control subsystem implements the ILC and its Simulink scheme is shown in Figure 7.20.

As explained in Section 2.6, the ILC is a high performance control technique based on the idea that, when a periodic signal reference is used, the system performance can be improved by learning from the knowledge of the error signal related to the previous periods. The simplest ILC formulation, called the proportional type ILC, has

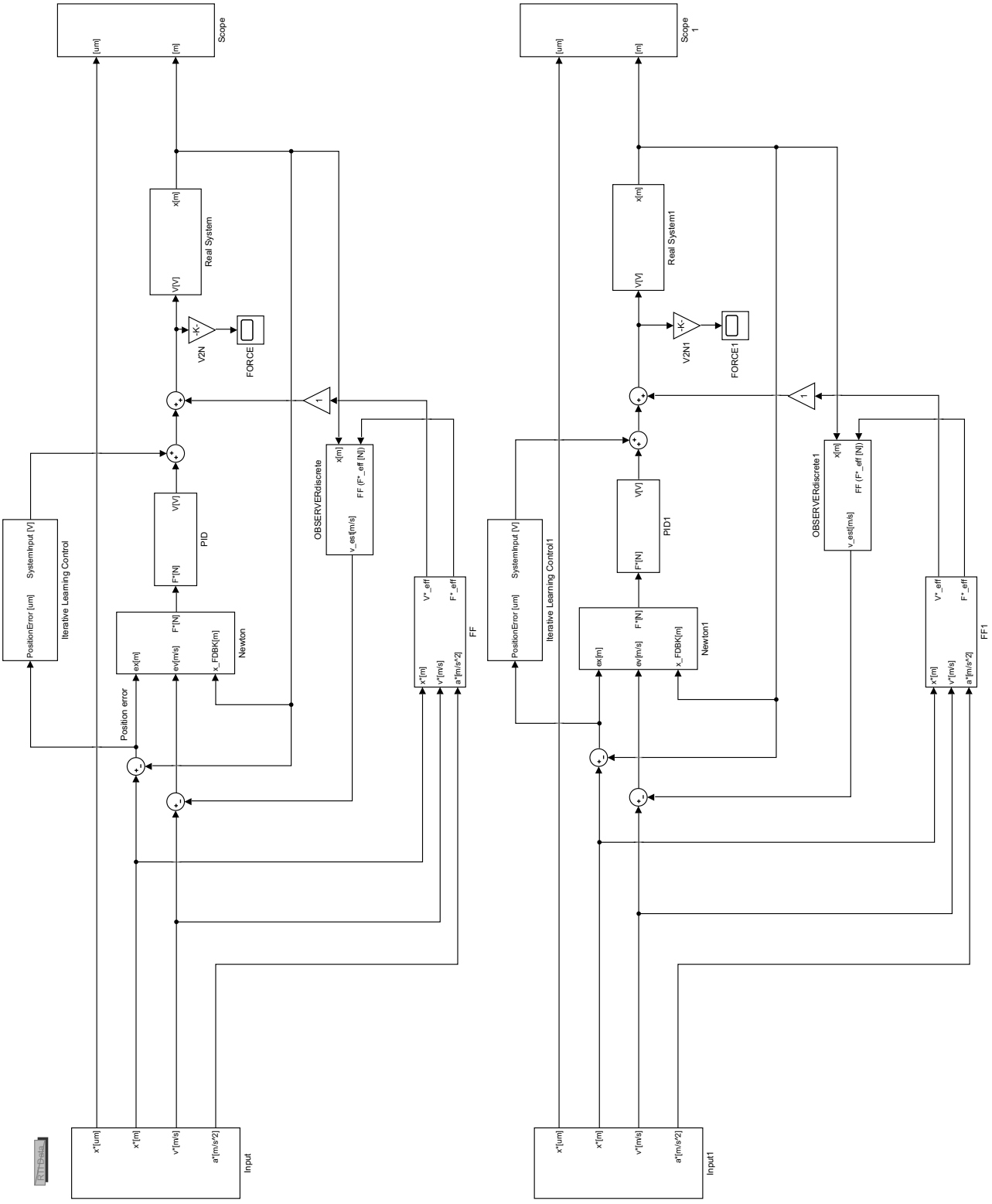

Figure 7.19: Two axes control scheme in Simulink with the ILC

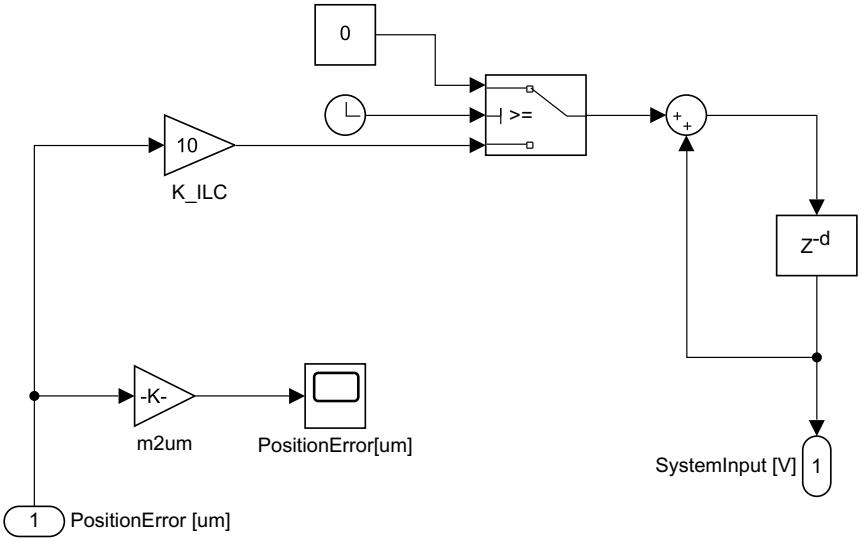

Figure 7.20: Simulink ILC Block

been used in this thesis work. Like in the application of the RPC, a clock has been added to switch off the ILC action after an appropriate time is elapsed, as shown in Figure 7.20. This solution was necessary to avoid the divergence of the position error. The clock stop time was tuned experimentally for each specific periodic reference signal analyzed.

7.3.1 *Sinusoidal Reference Signal*

Simulations and experiments were performed by feeding the system with sinusoidal reference signals of different amplitudes and frequencies in order to draw a circular shape in the XY-plane. The ILC was implemented to improve system performance.

7.3.1.1 *Simulations*

As for the RPC, only the simulation results related to one axis are reported because the results obtained on the other axis are very similar. The results achieved considering the non-linear model of the system for the position error when a sinusoidal reference signal with 1000 µm amplitude and 10 Hz frequency is used are shown in Figure 7.21. The plot on the left shows the results obtained without considering the addition of an external random noise to the system input, while the results achieved when the external random noise is added to better reproduce the real system behaviour are shown in the plot on the right. In both plots, three different condition are considered: without ILC action, with continuous ILC action and with ILC action interrupted after a suitable time.

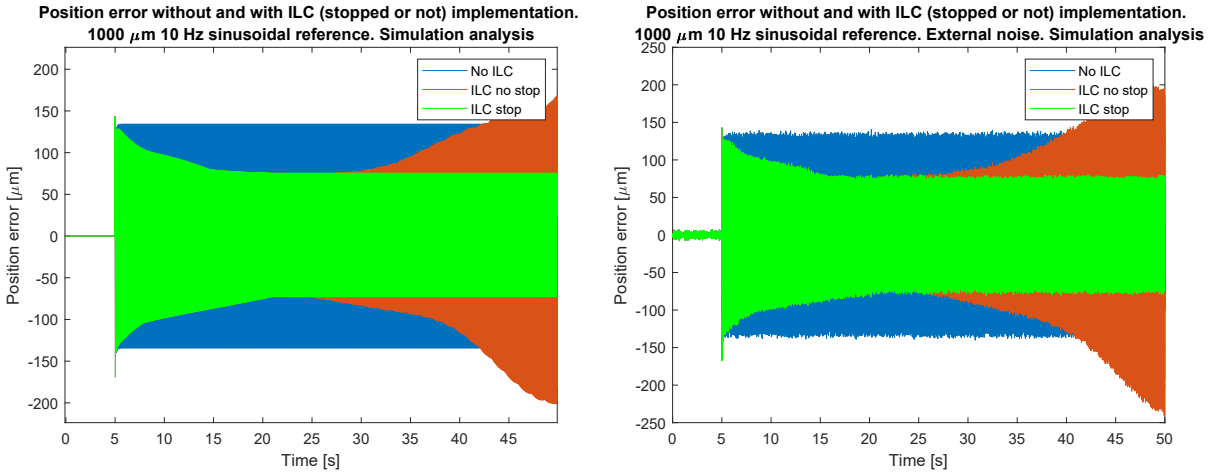

Figure 7.21: Simulation results for the position error without and with the ILC action (continuous or stopped after a suitable time). 1000 μm, 10 Hz sinusoidal wave reference signal. Non-linear model, without and with external noise.

As can be seen, when the ILC is used the position error diverges independently of the presence the external random noise added to the system input. However, in both cases, if the ILC action is interrupted at an appropriate time, the position error is significantly reduced and it does not diverge. Simulations related to the RPC showed that the error's divergent behaviour was due to the system's non-linearities and by the fact that the RPC implemention is based on the system linear transfer-function. To check if the ILC divergent behaviour shown in Figure 7.21 is due to the same cause, meaningful simulations were performed using the linear model. The results are shown in Figure 7.22. The plot on the left shows the results obtained without considering the addition of an external random noise to the system input, while the results achieved when the external random noise is added are shown in the plot on the right.

Unlike RPC, when the ILC is used, the divergent behaviour of the position error appears also when the linear model is used. Quite surprisingly, the error increases at a higher rate when the linear model is adopted. However, if the ILC action is interrupted at a suitable time, this undesirable behaviour is avoided.

7.3.1.2 *Experiments*

The sinusoidal reference signal amplitudes chosen in the experiments were: 100 μm and 500 μm, while the frequencies were: 1 Hz, 5 Hz and 10 Hz. The frequency of the sinusoidal reference signal was increased to 20 Hz only for the smaller amplitude selected (100 μm). Some meaningful examples of the measured position error, without and with the ILC (either continuous or interrupted after a suitable time) are shown in Figures 7.23 and 7.24. The first figure shows the results

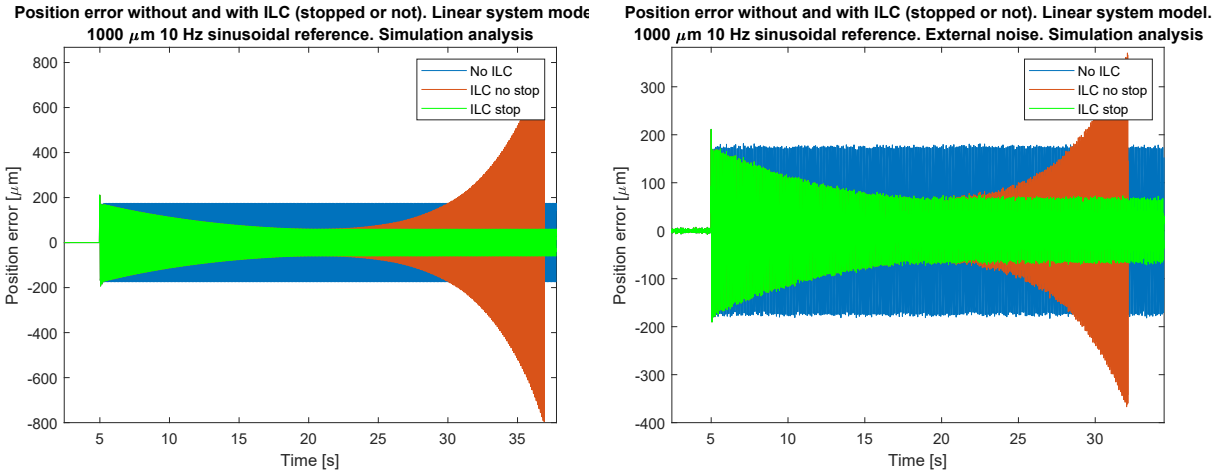

Figure 7.22: Simulation results for the position error without and with the ILC action (continuous or stopped after a suitable time). 1000 μm, 10 Hz sinusoidal wave reference signal. Linear model, without and with external noise.

achieved with the sinusoidal reference signal of 500 μm amplitude and 10 Hz frequency on both axes, while the second figure shows the results with amplitude 100 μm and frequency 20 Hz.

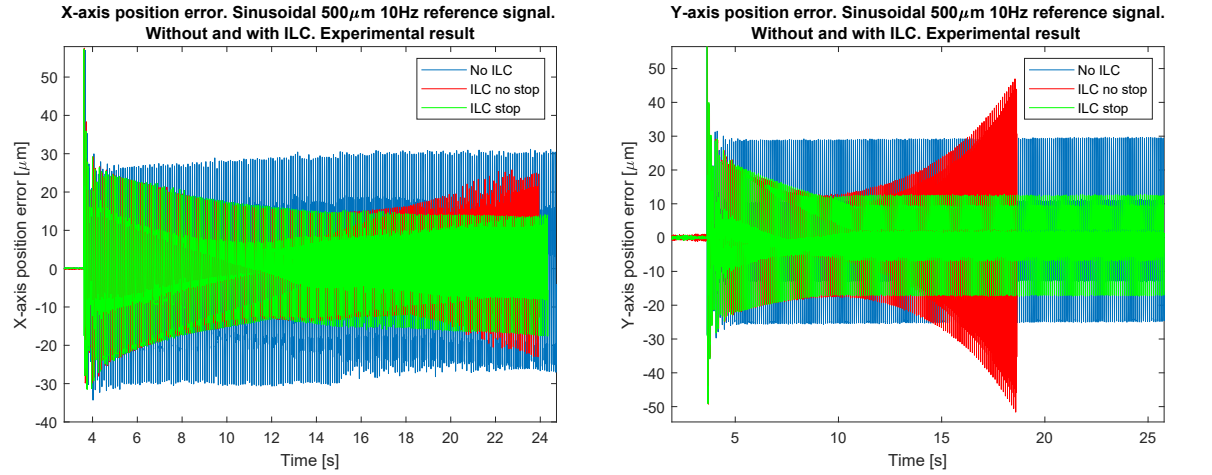

Figure 7.23: Experimental result for the position error without and with the ILC action (continuous or stopped after a suitable time). Sinusoidal wave reference signal 500 μm, 10 Hz on both axes.

As can be seen from Figures 7.23 and 7.24, the behaviours of the experimental and simulations results correspond well. Indeed, when the ILC is used, the position error is reduced, but, if it is not stopped at the appropriate time, the position error diverges.
As done for the RPC, the RMS value of the position error obtained without and with the ILC action was evaluated for all the configuration chosen, and the results are reported in Tables 7.9-7.12. Tables 7.9 and 7.10 show the results obtained when the sinusoidal reference

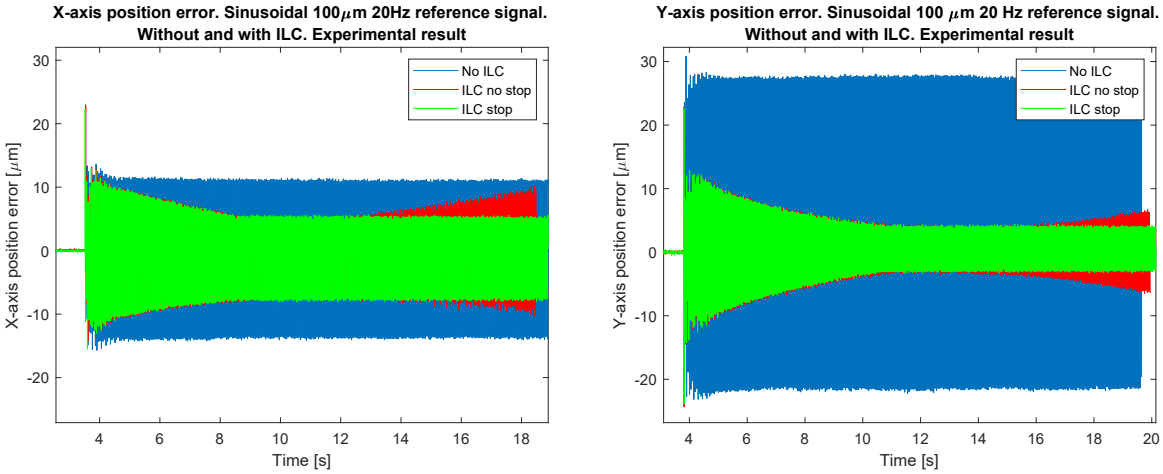

Figure 7.24: Experimental result for the position error without and with the ILC action (continuous or stopped after a suitable time). Sinusoidal wave reference signal 100 µm, 20 Hz on both axes.

signal with 100 µm amplitude was applied on both axes. Tables 7.11 and 7.12 show the results obtained when the amplitude was 500 µm for both axes.

Frequency [Hz]	1	1	5	5	10	10	20	20
ILC	No	Yes	No	Yes	No	Yes	No	Yes
RMSE [µm]	1.63	1.34	3.58	2.80	5.54	3.12	11.79	5.52

Table 7.9: RMS position error value without and with ILC action when feeding the X-axis sinusoidal reference signal of 100 µm amplitude.

Frequency [Hz]	1	1	5	5	10	10	20	20
ILC	No	Yes	No	Yes	No	Yes	No	Yes
RMSE [µm]	1.74	1.71	5.98	5.76	8.24	2.53	7.67	2.22

Table 7.10: RMS position error value without and with ILC action when feeding the Y-axis sinusoidal reference signal of 100 µm amplitude.

As Figures 7.23 and 7.24 and Tables 7.9-7.12 show, the ILC improves the system performance when the sinusoidal reference signal is used. However, a comparison with the results obtained when the RPC was applied, the RPC outperforms the ILC when it is used in a given configuration. Therefore, it can be concluded that when a sinusoidal reference signal is used, the RPC resulted to be the best choice for the system analyzed in this work when the aim is the minimization of the position error. For this reason, no measurements with the ILC action were performed when feeding the system with the triangular or the smooth trapezoidal reference signals.

Frequency [Hz]	1	1	5	5	10	10
ILC	No	Yes	No	Yes	No	Yes
RMSE [μm]	2.70	2.29	8.22	5.23	18.25	10.00

Table 7.11: RMS position error value without and with ILC action when feeding the X-axis sinusoidal reference signal of 500 μm amplitude.

Frequency [Hz]	1	1	5	5	10	10
ILC	No	Yes	No	Yes	No	Yes
RMSE [μm]	2.32	2.59	7.71	7.39	15.65	7.39

Table 7.12: RMS position error value without and with ILC action when feeding the Y-axis sinusoidal reference signal of 500 μm amplitude.

CONCLUSIONS AND FUTURE WORK

In this thesis, a two-axis high-performance compliant positioning system has been described and controlled using Matlab-Simulink. Different reference signals were used in order to draw distinct shapes in the XY-plane by moving both axes simultaneously over the complete permissible motion range. For example, sinusoidal reference signals on both axes were used to perform a circular shape, while triangular or smooth trapezoidal reference signals allowed the drawing of a square shape. The performance of both axes was analyzed using different amplitudes and frequencies of the reference signals. Due to a power limitation it was not possible to increase the signal frequency above 50 Hz. Moreover, that frequency was achieved only for small amplitude movements (up to 100 μm). Indeed, if the amplitude was increased to 500 μm, the system was able to work properly only up to a maximum frequency of 10 Hz. In addition, not all the reference signals selected allowed these values of amplitude and frequency to be achieved. For example, experimental results showed that the smooth trapezoidal reference signals do not work properly when the amplitude was 500 μm and the frequency was 10 Hz, because the associated power is greater than the one related to other reference signals selected. Thus, it was clear that the maximum power available imposes a trade-off between amplitude and frequency of the reference signals adopted. Consequently, a deep analysis of the resonant frequencies of the system was not necessary. Indeed, the knowledge of the first resonance frequency of a single axis (42.4 Hz) suffices to ensure that critical system excitations can be avoided.

When moving both axes simultaneously, two kinds of cross-coupling interaction were detected: kinematic and kinetostatic cross-coupling. Both of them are shown to be quite small, but to ensure the best achievable system performance, static compensations were implemented using extensive experimental data. In both cases, experiments show that the proposed compensations perform well for the working conditions considered. On the contrary, when dynamic reference signals were used (such as sinusoidal, triangular or smooth trapezoidal signals) the compensations implemented become useless. However, the cross-coupling effects are negligible compared to the system dynamic limitations, so that dynamic compensation of their effect, which would have required complex analysis and implementation procedures, was not implemented.

Measurements showed that the system performance significantly reduces when the signal reference frequency increases. Therefore high-performance control techniques specifically designed for periodic sig-

nals, such as the repetitive control (RPC) and the iterative learning control (ILC), were used to improve the system performance. Different simulation and experimental analyses showed that the RPC leads to the decrease of the position error, but after a certain time it tends to diverge. Simulation showed that this behaviour is related to the system non-linearity and to the use of a system linear transfer-function for the RPC implementation. However, when using sinusoidal or triangular reference signals, the interruption of the RPC action at a suitable time allowed a consistent reduction of the position error to be achieved, avoiding divergence. In such a way, the system performance were significantly improved, especially at the higher frequencies selected. Unfortunately, when the smooth trapezoidal reference signal was used, the RPC leads to a divergent behaviour also when its action was stopped. Thus the RPC is not suitable with this reference signal. The system performance was improved also using the ILC when the sinusoidal reference signal was selected. However, in that case, the RPC outperforms the ILC and so the ILC was not implemented when applying the other reference signals. In conclusion, the best solution to perform a circular trajectory in the XY-plane is using a sinusoidal reference signal on both axes and implementing the RPC interrupting its action at an appropriate time. Conversely, the best way to carry out a square shape in the XY-plane is to use the smooth trapezoidal reference signal on both axes without the RPC action when the frequency is low, and the triangular reference signal on both axes with the RPC interrupted at an appropriate time if the frequency is sufficiently high.

POSSIBLE FUTURE WORK DIRECTIONS

To further improve the system performance, a number of future works should be considered. Among them:

- Replace the servo amplifiers in order to obtain a lower output noise. Use of servo amplifiers with better characteristics will possible allow the system to perform movements in the nanometer range.
- Increase the power available to supply the system in order to enable axes movements at higher frequencies, hopefully over the full motion range. If this improvement is implemented, an in-depth vibrational analysis of the system should be performed to avoid movements at the resonant frequencies, which could break the manipulator.
- Implement a dynamic compensation of the detected cross-coupling effects. Dynamic compensation will be useful if the system performance approaches the nanometer range, because the cross-coupling interaction will be more relevant.

- Theoretically analyze the cause of the issue that arises when the RPC is used with the smooth trapezoidal reference signal and implement a possible solution, firstly using simulations and later by validating the obtained results in the real system.
- Modify the control scheme and implement a state-space control for the system. Since the state-space representation allows different and more effective controllers to be implemented, the system performance is expected to be improved.
- Extend the movement from two to three axes, adding an additional axis on the Z-direction of the XYZ compliant mechanism, with its associated actuator, CBPM component, servo amplifier and encoder.

APPENDIX

A

MATLAB CODES

A.1 K(x) FUNCTION

```
function Kx = K(x)
%#codegen
  E = 69e9;                                          % [Pa]

   W_CBPM  = 0.05;                                    % [m]
   T_CBPM  = 0.001;                                   % [m]
   l_CBPM  = 0.05;                                    % [m]
   EI_CBPM  = E * (1/12) * W_CBPM * T_CBPM^3;
   K_CBPM = (48*EI_CBPM)/l_CBPM^3;                    % [N/m]
   d = 12 / (T_CBPM / l_CBPM)^2;

   W_XYZ  = 0.001;                                    % [m]
   T_XYZ  = 0.001;                                    % [m]
   l_XYZ  = 0.05;                                     % [m]
   I_XYZ = (1/12)*( W_XYZ * T_XYZ^3);
   K_XYZ = 24*12*((E*I_XYZ) / l_XYZ^3);               % [N/m]

   D = l_CBPM^5 / d + ((x^2*l_CBPM^3)/700);

 Kx =(K_CBPM + K_XYZ)*x + (2.88 * EI_CBPM * x^3) / D;
```

A.2 ONE AXIS POSITION REFERENCE [8]

```
clear all
close all
clc

sample = 1e-3; % sample time
s_des = 1; % [mm] amplitude
t_des = 0.1; % [s] rise time desired
t_start = 5; %[s] delay time

%% Design

t_interval = 0:sample:t_des;
syms t;

f = 1/(2*t_des);
c = (2*s_des)/(1-cos(f*2*pi*t_des));
s = c * (( 1 - cos( f*2*pi*t ) ) / 2 );

S = c * (( 1 - cos( f*2*pi*t_interval ) ) / 2 );

figure
fplot( matlabFunction(s), [0 t_des] );

% add start delay
START = zeros(round(t_start/sample), 1);

TIME = 0:sample:(t_start+t_des);

X.time = TIME;
X.signals.values = [START; S'];

figure
plot(X.time,X.signals.values);
ylim([-.1 1.1])
xlim([4.98 5.11])
```

A.3 NON-LINEAR STIFFNESS FUNCTION [8]

```
function  Kx = K_function(ex,x_FDBK)
%#codegen

   E = 69e9;                                              % [Pa]

   W_CBPM  = 0.05;                                        % [m]
   T_CBPM  = 0.001;                                       % [m]
   l_CBPM  = 0.05;                                        % [m]
   Kt_CBPM = 4 * ((E * W_CBPM * T_CBPM^3) / l_CBPM^3); % [N/m]
   EI_CBPM  = E * (1/12) * W_CBPM * T_CBPM^3;
   d        = 12 / (T_CBPM / l_CBPM)^2;

   W_XYZ  = 0.001;                                        % [m]
   T_XYZ  = 0.001;                                        % [m]
   l_XYZ  = 0.05;                                         % [m]
   Kt_XYZ = 24* ((E * W_XYZ * T_XYZ^3) / l_XYZ^3);     % [N/m]

   x_FDBK2 = x_FDBK*x_FDBK;
   D = l_CBPM^5 / d + ((x_FDBK2*l_CBPM^3)/700);


   if ((x_FDBK+ex) < 0)
       error = -1e4;
   else
       error = -0.5e4;
   end

   k = Kt_CBPM + EI_CBPM*((8.64*x_FDBK2 / D) - ((5.76 * l_CBPM^3
       * x_FDBK2*x_FDBK2)...
    / (700 * D^2))) + Kt_XYZ + error;

Kx = k*ex;
```

A.4 NON-LINEAR FORCE FUNCTION [8]

```
function  F = delta(x)
%#codegen
   E = 69e9;                                              % [Pa]

   W_CBPM  = 0.05;                                        % [m]
   T_CBPM  = 0.001;                                       % [m]
   l_CBPM  = 0.05;                                        % [m]
   Kt_CBPM = 4 * ((E * W_CBPM * T_CBPM^3) / l_CBPM^3); % [N/m]
   EI_CBPM  = E * (1/12) * W_CBPM * T_CBPM^3;
   d        = 12 / (T_CBPM / l_CBPM)^2;

   W_XYZ  = 0.001;                                        % [m]
   T_XYZ  = 0.001;                                        % [m]
   l_XYZ  = 0.05;                                         % [m]
   Kt_XYZ = 24* ((E * W_XYZ * T_XYZ^3) / l_XYZ^3);     % [N/m]

   D = l_CBPM^5 / d + ((x^2*l_CBPM^3)/700);

   if (x < 0)
       errorL = -1e4;
       errorN = 1.8;
   else
       errorL = -0.5e4;
       errorN = 2;
   end

   % Theoretical Values
   % errorL = 0;
   % errorN = 2.88;

F = (Kt_CBPM + Kt_XYZ + errorL) * x + (errorN * EI_CBPM * x^3) /
    D;
```

A.5 SINUSOIDAL REFERENCE SIGNAL

```
clear all
close all
clc

tdelay1 = 5; %  delay [s]
t_des = 100; % run a sinusoidal for t_des seconds
sample = 1e-3; % sample time
t_interval = 0:sample:t_des-tdelay1;
f = 1; % hz
T = 1/f; % period [s]
START = zeros(round(tdelay1/sample), 1);

tdelay2 = 5 - T/4 ; %  delay [s] %T/4 to have pi/2 phase
    difference
t_interval2 = 0:sample:t_des-tdelay2;
START2 = zeros(round(tdelay2/sample), 1);

TIME = 0:sample:t_des;

sinWave1.time = TIME;
S1 = 1*sin(2*pi*f*t_interval);
sinWave1.signals.values = [START; S1'];

sinWave2.time = TIME;
S2 = 1*sin(2*pi*f*t_interval2);
sinWave2.signals.values = [START2; S2'];

plot(sinWave1.signals.values,sinWave2.signals.values); % plot the
     XY plane signal
axis equal;
figure
plot(sinWave1.time, sinWave1.signals.values);
hold
plot(sinWave2.time, sinWave2.signals.values,'r');
```

A.6 TRIANGULAR REFERENCE SIGNAL

```
clear all
close all
clc

tdelay1 = 5; %  delay [s]
t_des = 100;
sample = 1e-3; % sample time
t_interval = 0:sample:t_des-tdelay1;
f = 1; % hz
T = 1/f; % period [s]
START = zeros(round(tdelay1/sample), 1);

tdelay2 = 5 - T/4 ; %  delay [s] %T/4 to have pi/2 phase
    difference
t_interval2 = 0:sample:t_des-tdelay2;
START2 = zeros(round(tdelay2/sample), 1);

TIME = 0:sample:t_des;

TriangularWave1.time = TIME;
S1 = 1*sawtooth(2*pi*f*t_interval, 0.5);
TriangularWave1.signals.values = [START; S1'];

TriangularWave2.time = TIME;
S2 = 1*sawtooth(2*pi*f*t_interval2, 0.5);
TriangularWave2.signals.values = [START2; S2'];

plot(TriangularWave1.signals.values,TriangularWave2.signals.
    values); % plot the XY plane signal
axis([-1.5 1.5 -1.5 1.5]);
axis equal;
figure
plot(TriangularWave1.time, TriangularWave1.signals.values);
hold
plot(TriangularWave2.time, TriangularWave2.signals.values,'r');
```

A.7 TRAPEZOIDAL REFERENCE SIGNAL

```
clear all
close all
clc

%% Trapezoidal wave
f = 1; %Hz
T = 1/f; %period
trise = T/4;
tcostant2 = T/4;
tcostant4 = T/4;
tfall = T/4;
amplitude = 2; % 1 positive and 1 negative
amplitude2 = 0;
offset = amplitude/2;
Ts = 1e-3; %sample time
T = trise +tcostant2 + tfall +tcostant4;

t = 0:Ts:T;

t1 = 0:Ts:trise;
s1 = (amplitude/trise)*t1 - offset;

t2 = 0:Ts:(tcostant2 -Ts);
s2 = repmat(amplitude, size(t2))- offset;

t3 = 0:Ts:(tfall - Ts);
s3 = amplitude - (amplitude/tfall)*t3 -offset;

t4 = 0:Ts:(tcostant4 -Ts);
s4 = repmat(amplitude2, size(t4))-offset;

S = [s1 s2 s3 s4];
plot(t,S);

t1first = 0:Ts:(trise/2);
s1first = (amplitude/trise)*t1first;
Sfirst = [s1first s2 s3 s4];

Scenter = S;

n = 100; % number of periods
nt = 0: Ts: (n*T + (n-1)*Ts);
periodicTrapezoidal = repmat(Scenter, 1, n);
plot(nt, periodicTrapezoidal);
trapezoidalWave = [Sfirst periodicTrapezoidal];

%% TwoAxis Reference with start dalay
tdelay1 = 5; %[s] delay time axis x
tdelay2 = 5 - T/4 ; %  delay [s] %T/4 to have pi/2 phase
    difference
```

```
tdifference = T/4; %time difference
endDifference = zeros(round(tdifference/Ts),1);

START1 = zeros(round(tdelay1/Ts), 1);
START2 = zeros(round(tdelay2/Ts), 1);
Time1 = 0: Ts: ((n + 1)*T - T/8 + (n)*Ts + tdelay1); %n-time
    periodic, +1 is the first (that have T/8 duration less)
Time2 = 0: Ts: ((n + 1)*T - T/8 + (n)*Ts + tdelay1); %n-time
    periodic, +1 is the first (that have T/8 duration less)

TrapezoidalWave1.time = Time1;
TrapezoidalWave1.signals.values = [START1; trapezoidalWave'];

TrapezoidalWave2.time = Time2;
TrapezoidalWave2.signals.values = [START2; trapezoidalWave';
    endDifference];

plot(TrapezoidalWave1.signals.values, TrapezoidalWave2.signals.
    values); % plot the XY signal
axis ([-1.5 1.5 -1.5 1.5]);
axis equal;
figure
plot(TrapezoidalWave1.time, TrapezoidalWave1.signals.values);
hold
plot(TrapezoidalWave2.time, TrapezoidalWave2.signals.values,'r');
```

A.8 KINEMATIC CROSS-COUPLING FUNCTION

```
function [xPosFF, xVelFF ,xAccFF, yPosFF, yVelFF, yAccFF] =
    kinematic_crossCoupling(xPos, xVel ,xAcc, yPos, yVel, yAcc)
%#codegen

input = [xPos; xVel; xAcc; yPos; yVel; yAcc]; % vertical vector
    of input variables
if (yPos > 0)
    A = 0.00402;
else
    A = -0.00141;
end
if (xPos > 0)
    B = 0.00325;
else
    B = -0.00188;
end

matrix = [ 1 0 0 A 0 0; 0 1 0 0 A 0; 0 0 1 0 0 A; B 0 0 1 0 0; 0
    B 0 0 1 0; 0 0 B 0 0 1];
output = matrix * input; % vertical vector of output variables

xPosFF = output(1);
xVelFF = output(2);
xAccFF = output(3);
yPosFF = output(4);
yVelFF = output(5);
yAccFF = output(6);
```

A.9 KINETOSTATIC CROSS-COUPLING FUNCTION

```
function Fcc = KinetostaticCC(x, Yposition)
%#codegen
if(Yposition >0)
    slope = 0.0014721; %[N/um]
    intercept = -0.041112; %[N]
else
    slope = -0.0019246; %[N/um]
    intercept = -0.039929; %[N]
end
Fcc = (slope*x + intercept)*Yposition;
```

A.10 RPC SCRIPT

```
Kf= 35.14;
Kdx = 1.804;
Kdy = 1.6153;
mtot = 1.824;
c = 22.353;
Kt = 129460;

Ts = 0.001; %sample time
N = round(1/(f*Ts)); %number of sample per period
if f == 1
    Krx = 0.5; %gain of x-axis RPC
    Kry = 0.1; %gain of y-axis RPC
elseif f == 5
    Krx = 0.3; %gain of x-axis RPC
    Kry = 0.05; %gain of y-axis RPC
elseif f == 10
    Krx = 0.1; %gain of x-axis RPC
    Kry = 0.08; %gain of y-axis RPC
elseif f == 20
    Krx = 0.05; %gain of x-axis RPC
    Kry = 0.05; %gain of y-axis RPC
elseif f == 50
    Krx = 0.05; %gain of x-axis RPC
    Kry = 0.05; %gain of y-axis RPC
else
    Krx = 0;
    Kry = 0;
    % if f is not one of the choosen ones, don't use the RPC (
        need to be tuned for that frequency to prevent divergent
        signals)
    %if the reference signal has another frequency, tuned the RPC
         for it and add it with another elseif
end

s = tf('s');
Px = (Kf*Kdx)/(mtot*s^2 + c*s + Kt); %open loop process linear
    transfer function X axis continuous time domain
Py = (Kf*Kdx)/(mtot*s^2 + c*s + Kt); %open loop process linear
    transfer function Y axis continuous time domain

Wxc = (Kf*Kdx)/(mtot*s^2 + c*s + Kt + Kf*Kdx); %close loop
    process linear transfer function X axis continuous time
    domain
Wyc = (Kf*Kdy)/(mtot*s^2 + c*s + Kt + Kf*Kdy); %close loop
    process linear transfer function Y axis continuous time
    domain

z = tf('z', Ts);

Wxd = c2d(Wxc, Ts, 'zoh'); %close loop discrete transfer function
```

```
[nx,dx] = tfdata(Wxd,'verbose');
nx=nx(2:3);
zeroX = zero(Wxd);
polesX = pole(Wxd);

Wyd = c2d(Wyc, Ts, 'zoh'); %close loop discrete transfer function
[ny,dy] = tfdata(Wyd,'verbose');
ny=ny(2:3);
zeroY = zero(Wyd);
polesY = pole(Wyd);
```

BIBLIOGRAPHY

[1] International vocabulary of basic and general terms in metrology (vim). https://www.bipm.org/en/publications/guides/vim.html, 2008. Accessed: 2020-03-25.

[2] Guangbo Hao. Educational material of the class: "Advanced Robotics". University College Cork, Ireland, 2020.

[3] Applications. http://www.madcitylabs.com/applications.html, . Mad Cyty Labs Inc, Accessed: 2020-03-27.

[4] Nanomanipulation. A basic look at nanomanipulation, nanofabrication, self assembly, limitations and future opportunities for nanomanufacturing. https://www.azonano.com/article.aspx?ArticleID=1720, . AZO nano, Accessed: 2020-03-27.

[5] Haiyang Li. Approaches to the Synthesis, Modelling and Optimisation of Spatial Translational Compliant Parallel Mechanisms. PhD Thesis, University College Cork(UCC), Ireland, 2016.

[6] Larry L. Howell. *Compliant mechanisms*. Wiley, New York, 2001.

[7] Compliant mechanism explained. https://www.compliantmechanisms.byu.edu/about-compliant-mechanisms. BYU CMR, Accessed: 2020-03-26.

[8] Aldo Marchi. Wide Range Control and Performance Evaluation of a Single-Axis Compliant Nano-Positioning System. 2019. Master Thesis, University of Padua, Italy.

[9] Fabiana Federica Ferro. Nonlinear Control of a Flexure-Based Single Degree of Freedom Nanopositioning System. 2016. Master Thesis, University of Padua, Italy.

[10] Riccardo Sandon. Modelling, Control and Performance Evaluation of a Single-Axis Compliant Nano-Positioning System. 2017. Master Thesis, University of Padua, Italy.

[11] Riccardo Sandon, Haiyang Li, Fabiana Federica Ferro, Alberto Trevisani, Guangbo Hao, and Richard Kavanagh. High-Performance Control of a Single-Axis Compliant Nano-Positioning System: Control. 2017.

[12] Youqing Wang, Furong Gao, and Francis J Doyle III. Survey on iterative learning control, repetitive control, and run-to-run control. *Journal of Process Control*, 19(10):1589–1600, 2009.

[13] PID Theory Explained. https://www.ni.com/en-ie/innovations/white-papers/06/pid-theory-explained.html, . National Instruments, Accessed: 2020-01-28.

[14] Ziegler - Nichols method. https://en.wikipedia.org/wiki/Ziegler%E2%80%93Nichols_method, . Wikipedia, Accessed: 2020-01-28.

[15] A.B. Barrett. The Application of Observers in Position Servosystem. June 1992. M. Eng. Sc.thesis, National University of Ireland.

[16] Masayoshi Tomizuka, Tsu-Chin Tsao, and Kok-Kia Chew. Analysis and synthesis of discrete-time repetitive controllers. 1989.

[17] Roberto Oboe. "Progettazione di Sistemi di Controllo" Class Notes. University of Padua, Italy, 2019.

[18] Small Gain Theorem. https://en.wikipedia.org/wiki/Small-gain_theorem. Wikipedia, Accessed: 2020-02-04.

[19] Douglas A Bristow, Marina Tharayil, and Andrew G Alleyne. A survey of iterative learning control. *IEEE control systems magazine*, 26(3):96–114, 2006.

[20] Guangbo Hao and Haiyang Li. Extended Static Modeling and Analysis of Compliant Compound Parallelogram Mechanisms Considering the Initial Internal Axial Force. *Journal of mechanisms and robotics*, 8(4):041008, 2016.

[21] Haiyang Li, Guangbo Hao, and Richard Kavanagh. A New XYZ Compliant Parallel Mechanism for Micro-/Nano-Manipulation: Design and Analysis. *Micromachines*, 7(2):23, 2016.

[22] Riccardo Sandon, Haiyang Li, Fabiana Ferro, Alberto Trevisani, Richard Kavanagh, and Guangbo Hao. High-Performance Control of a Single-Axis Compliant Nano-Positioning System: Design. 2017.

[23] Danielle Collins. How do rotary voice coil actuators work? https://www.motioncontroltips.com/how-do-rotary-voice-coil-actuators-work/, July 2018. Motion Control Tips, Accessed: 2020-01-10.

[24] What is a Voice Coil Actuator (VCA)? http://www.beikimco.com/resources-downloads/about-VCAs/what-is-a-voice-coil-actuator, . Bei Kimko, Accessed: 2020-01-10.

[25] Linear Actuator LA 30-48-000A. http://cdn1.beikimco.com/Products/Downloads_vca_frameless/voice-coil-actuator-linear-frameless-la30-48-000a.pdf, . BEIKIMCO, Accessed: 2020-01-10.

[26] SIGNUM encoder system. http://resources.renishaw.com/en/download/data-sheet-signum-encoder-system--34304, . Renishaw, Accessed: 2020-01-13.

[27] SIGNUM software. http://resources.renishaw.com/en/download/user-guide-signum-software--73679, . Renishaw, Accessed: 2020-01-13.

[28] Advanced Motion Control Analog Servo Drive B25A20. https://dpk3n3gg92jwt.cloudfront.net/domains/amc/pdf/AMC_Datasheet_B25A20.pdf. Advanced Motion Control, Accessed: 2020-01-13.

[29] DS1104 R & D Controller Board. https://www.dspace.com/shared/data/pdf/2019/dSPACE_DS1104_Catalog2019.pdf. dSPACE, Accessed: 2020-01-14.

[30] ControlDesk. https://www.dspace.com/shared/data/pdf/2019/dSPACE_ControlDesk-Brochure_05_2019_English.pdf. dSPACE, Accessed: 2020-01-14.

[31] Guangbo Hao and Haiyang Li. Nonlinear Analytical Modeling and Characteristic Analysis of a Class of Compound Multibeam Parallelogram Mechanisms. *Journal of Mechanisms and Robotics*, 7 (4):041016, 2015.